
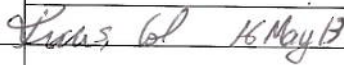


STAFF SUMMARY SHEET

	TO	ACTION	SIGNATURE (Surname), GRADE AND DATE		TO	ACTION	SIGNATURE (Surname), GRADE AND DATE
1	DFAN	sig	 16 May 13	6			
2	DFER	approve	 16 May 13	7			
3	DFAN	action	(Author /Originator)	8			
4				9			
5				10			

SURNAME OF ACTION OFFICER AND GRADE

SYMBOL

PHONE

TYPIST'S
INITIALS

SUSPENSE DATE

McLaughlin, CIV

333-2613

caf

20130522

SUBJECT

Clearance for Material for Public Release

USAFA-DF-PA- 347

DATE

20130516

SUMMARY

1. PURPOSE. To provide security and policy review on the document at Tab 1 prior to release to the public.

2. BACKGROUND.

Authors: Casey Fagley

Title: Flow Control Final Report (FA7000-10-2-0003)

Circle one: Abstract Tech Report Journal Article Speech Paper Presentation Poster

Thesis/Dissertation Book Other: _____

Check all that apply (For Communications Purposes):

☒ CRADA (Cooperative Research and Development Agreement) exists

☐ Photo/ Video Opportunities ☐ STEM-outreach Related ☐ New Invention/ Discovery/ Patent

Description: This report is a comprehensive summary of the research under cooperative agreement FA7000-10-2-0003 which was executed over the dates January, 24 2010 → January 24, 2013. From the agreement, "Closed loop flow control efforts focus on aero optic and energy extraction, with extensive effort in the development of automatic control algorithms and techniques, experimental flow control methodologies and CFD simulations.

Release Information: Release required before posting the report to DTIC.

Previous Clearance information: Most information in the manuscript has previously been released in conference and journal papers.

Recommended Distribution Statement: Distribution A: approved for public release, distribution unlimited

3. DISCUSSION.

4. RECOMMENDATION. Sign coord block above indicating document is suitable for public release. Suitability is based solely on the document being unclassified, not jeopardizing DoD interests, and accurately portraying official policy.

Thomas E. McLaughlin, Ph.D.

Director, Aeronautics Research Center

Flow Control

USAFA AERONAUTICS RESEARCH LABORATORY

FINAL REPORT

JANUARY, 24 2010 → JANUARY 24, 2013

KCENGINEERING, INC
Kinematics & Controls

Author:

Casey FAGLEY, Ph.D
KC Engineering, Inc.

915 Ellston Street
Colorado Springs, CO 80907
(505) 620-8470



Contents

1	Relevant Findings	4
2	Publications	4
3	Proposed Research	6
3.1	Approach	6
4	Research Synopsis	8
4.1	Overview	8
4.2	Theoretical Background	12
4.2.1	Numeric Simulation	13
4.2.2	Reduced Order Modeling	16
4.2.2.1	Numerical Reduction	16
4.2.3	System Identification	17
4.2.4	Feedback Control	22
4.2.4.1	State Estimation	22
4.2.4.2	Sensor Placement	22
4.2.4.3	Linear Stochastic Estimation	23
4.2.4.4	Artificial Neural Network Estimation	23
4.2.4.5	Wavenet Estimation	24
4.2.4.6	Adaptive Control	24
5	Applications	27
5.1	Cylinder Wake	27
5.2	Aero Optics	33
5.2.1	Technical approach	35
5.2.1.1	Basic flow parameters	36
5.2.1.2	Optical definitions	37
5.2.2	Numerical Simulation	37
5.2.2.1	Grid generation	38
5.2.2.2	Results	39
5.2.2.3	Actuation	42
5.2.2.4	Open loop forcing	42
5.2.3	Reduced Order Modeling	48
5.2.3.1	Numerical Reduction	48
5.2.3.2	POD Parameter Study	49
5.3	System Identification	63
5.3.1	Feedback Control	65
5.3.1.1	State Estimation	65
5.3.2	Adaptive Control	66
5.3.2.1	Feedback control of the WNARX model	70
5.3.2.2	Feedback control in the CFD simulation	73
5.4	Axisymmetric Bluff Body	81

5.4.1	Overview	81
5.4.2	Open Loop Dynamics Experiment	85
5.4.2.1	Step Response	86
5.4.2.2	Sinusoidal Response	88
5.4.2.3	Impulse Response	89
5.4.3	Open Loop Dynamics Simulations	90
5.4.3.1	Step Response	91
5.4.4	Impulse Response	92
5.4.5	Numerical decomposition and flow state definition	95
5.4.5.1	Grid and Model Geometry	95
5.4.5.2	Proper Orthogonal Decomposition	96
5.4.5.3	Results	97
5.4.5.4	Proper Orthogonal Decomposition of the Flow Field	100
5.4.6	Sensor placement	106
5.4.6.1	Optimal Method	106
5.4.6.2	Linear Stochastic Estimation	107
5.4.6.3	Results	107
5.4.6.4	Experimental Validation	110
5.4.6.5	Summary	113
5.4.7	System dynamics and modeling	114
5.4.7.1	Modeling Techniques	114
5.4.7.2	Output Error Method	115
5.4.7.3	Prediction Error Method	115
5.4.7.4	Subspace Identification Method	115
5.4.7.5	Model Selection Experiments	116
5.4.7.6	Model Selection Simulations	119
5.4.8	Closed loop dynamics	123
5.4.8.1	Closed Experimental Model Results	123
5.4.9	Closed Experimental Results	127
5.4.9.1	Closed Simulation Model Results	128
5.4.9.2	Closed Simulation Results	131
5.4.10	Modeling summary	131
5.5	Business Summary	133

6 References

133

1 Relevant Findings

Contract FA7000-10-2-0003 was in direct response to Broad Agency Announcement (BAA) with the Aeronautics Laboratory at the United States Air Force Academy. The announcement in the BAA in which this contract was directly related is quoted from the BAA as,

Current research strengths include several complementary thrusts. Closed loop flow control efforts focus on aero-optic and energy extraction, with extensive effort in the development of automatic control algorithms and techniques, experimental flow control methodologies and CFD simulations.

Work under this contract produced new, innovative and theoretical methods for developing control algorithms. In particular artificial neural networks coupled with direct adaptive control was a new innovative solution for achieving successful control of very high dimensional, non linear dynamical systems. This control technique which is described in detail throughout this manuscript was successfully applied to a wide variety of flows. This flow control approach proved to successfully reduce the drag on a circular cylinder by decreasing the amount of energy in the von Kármán street, mitigate optical aberrations through a free unstable shear layer, as well as regulate and exploit the asymmetric vortex formulation behind an axi-symmetric bluff body at high incidence. Each of these flow control applications had inherently different dynamics including periodic vortex shedding, separated free unstable shear layers, and combinations thereof, which demanded a large amount of robustness from a control design perspectives. Applications and demonstration of successful feedback flow control where shown both experimentally and computationally. This manuscript goes into great detail on the theoretical approach which has been adopted by the US-AFA flow control group and then details the applications to each of the fluid dynamics problems. The report then summarizes the business portion of the contractual agreement.

This material is based on research sponsored by the US Air Force Academy under agreement number FA7000-10-2-0003. The U.S. Government is authorized to reproduce and distribute reprints for Governmental purposes notwithstanding any copyright notation thereon.

The views and conclusions contained herein are those of the authors and should not be interpreted as necessarily representing the official policies or endorsements, either expressed or implied, of the US Air Force Academy or the U.S. Government.

[All information and data Herein is] approved for public release, distribution is unlimited.

2 Publications

Z. H. Adams and C. Fagley. Novel cyclorotor pitching mechanism for operation at curtate and prolate advance ratios. In *AIAA*, AIAA2013.

- C. Fagley, M. Balas, S. Siegel, J. Seidel, and T. McLaughlin. Reduced Order Model of Cylinder Wake with Direct Adaptive Feedback Control. In *AIAA Paper 2009-5856*, 2009.
- C. Fagley, J. Seidel, S. Siegel, and T. McLaughlin. Reduced Order Modeling using Proper Orthogonal Decomposition (POD) and Wavenet System Identification of a Free Shear Layer. In *2nd Active Flow Control Conference, Berlin, Germany*, 2010a.
- C. Fagley, J. Farnsworth, J. Seidel, and T. McLaughlin. Experimental Study of Open Loop Plasma Actuation on a von Karman Ogive. In *AIAA Paper 2012-0905*, 2012a.
- C. Fagley, C. Porter, J. Seidel, J. Farnsworth, and T. McLaughlin. Optimal sensor arrangement for asymmetric vortex state estimation on a slender body at high incidence. In *AIAA Aerospace Sciences Meeting, American Institute of Aeronautics and Astronautics, New Orleans, LA (submitted for publication)*, 2012b.
- C. Fagley, J. Seidel, and S. Siegel. Computational investigation of irregular wave cancellation using a cycloidal wave energy converter. In *31st International Conference on Ocean, Offshore and Arctic Engineering (OMAE)*, number OMAE2012-83434, June 2012c.
- C. Fagley, S. Siegel, and J. Seidel. Wave cancellation experiments using a 1:10 scale cycloidal wave energy converter. In *1st Asian Wave and Tidal Energy Conference (AWTEC) Jeju Island, Korea, November 27-30*, 2012d.
- C. Fagley, J. Seidel, and T. McLaughlin. Feedback control of a shear layer for aero-optic applications. *International Journal of Flow Control*, Vol. 3 Issue 1:p1–18, March 2011.
- C. Fagley, J. Farnsworth, C. Porter, J. Seidel, T. McLaughlin, J. Lee, and E. Lee. Open-loop dynamics of asymmetric vortex wake behind an ogive at high incidence. *Journal of Flow Control*, submitted 2012.
- C. P. Fagley, M. J. Balas, J. Seidel, S. Siegel, and T. McLaughlin. Surface Mounted Flow State Estimation of Reduced Order POD Models: Shear Layer. In *AIAA Paper 2010-7599*, 2010b.

3 Proposed Research

3.1 Approach

Classical control theory is limited when dealing with high-dimensional, extremely non-linear systems such as flow fields. New techniques need to be established to make use of current control theories, while also allowing for a reasonable design process for linear, non-linear, or adaptive control for complex flow fields. Low dimensional modeling is the first step in synthesizing control algorithms. Computational fluid dynamic (CFD) simulations, which are numeric approximations of the Navier Stokes equations seen in Eq 74

$$\rho \left(\frac{\partial \mathbf{u}}{\partial t} + \mathbf{u} \cdot \nabla \mathbf{u} \right) = -\nabla p + \nabla \cdot \mathbf{T} + \mathbf{f}, \quad (1)$$

are utilized to produce an open loop forcing parameter space, typically varying frequency and amplitude of the actuation signal. Numerical reduction schemes such as principle component analysis or proper orthogonal decomposition (POD,SPOD,BPOD,DPOD) are then used to greatly reduce the full order system (n) to a truncated mode set (m), such that $m \ll n$ as seen by the following equation.

$$\Phi(\mathbf{x}, t) = \sum_{i=1}^m a_i(t) \phi_i(\mathbf{x}). \quad (2)$$

The resulting mode set shows the decoupling of time and space, correspondingly modal amplitudes ($a_i(t)$) and spatial modes ($\phi_i(\mathbf{x})$). The highest energy/most dominant modes are retained in the truncation so that the reduced data set accurately represents the full order system. The control engineer will recognize these time coefficients($a_i(t)$) as the internal states of system.

Typically, a Galerkin projection is used to project the truncated mode set onto the Navier Stokes equations, but that creates numerous modeling errors, such as unsatisfied boundary conditions, numerical instabilities, and poor implementation of actuation term. The research proposed, utilizes system identification techniques, such as weighted least squares, correlation functions, power spectral density with impulse responses, neural networks (ANN-ARX), networks with wavelet radial basis transfer functions (WNARX), and other non-linear methods to formulate a state-space system. Typically, control designers desire these system identification models to be linear-time-invariant (LTI) state space systems. This allows for very simple control design procedures. The problem with the LTI approximation is that fluids are not a linear system, as seen from the Navier-Stokes equations which govern fluid flow (Eq. 74).

A linear model breaks down and insufficiently represents the flow field rendering it useless for any type of control design. New methods or combination of methods for both system identification and control development, from non-linear to adaptive control techniques, need to be explored. This research proposes to investigate wavelet basis networks (WNARX) to demonstrate the full capability of identifying complex flow response for a range of open loop parameters. The WNARX will represent a dynamic model which can simulate off design flow cases, serve as reference signal, and ultimately predict closed loop behavior for control design. The WNARX model uses the same network architecture as a neural network; the only difference is radial basis functions are used as each neuron's transfer function. This is shown by,

$$\Psi(t)_{u,s} = \Psi \left(\frac{t-u}{s} \right), \quad (3)$$

where u is the translation of the wavelet, s is the dilation, and Ψ is referred to as the mother wavelet, which is a radial basis function in this case. WNARX models are much better suited for identifying the frequency rich dynamics of complex, turbulent flow fields. The overall WNARX model is given by,

$$\hat{f}(t) = \sum_{i=1}^N w_i \Psi(s_i(t - u_i)) + c^T t + f_0 \quad (4)$$

where w_i are the weights, N is the number of wavelet functions, c^T represent the linear connections, and f_0 is the bias. This proposal will use this new system identification method to formulate an extremely low dimensional model based from CFD simulations and POD/DPOD decompositions to accurately predict closed loop dynamics of a given flow field. This model is then used to perform feedback simulations to condition control algorithms which can then be applied directly to CFD simulations and experiments. Previously, this control design approach was applied to the simple cylinder wake flow field Fagley et al. [2009] Siegel et al. [2008]. Although successful for the very simple flow, we desired to extend the approach to more complex, turbulent, flows, e.g. free, unstable shear layer. Initial results are promising. The WNARX method for formulating a model has proven to be much better than the previous ANN-ARX model. Neural networks have inherent problems. First, there is that no straight forward method exists for determining the number of hidden neurons, number of layers, or parameters of the regression vector. Training relies heavily on trial and error to find a combination of parameters that yields acceptable results. Second, the convergence of these networks depends heavily upon the initialization of the weighting matrices. This can lead to drastically different results when training a single network with a given set of parameters twice because of the initial random generation of weights. Third, a properly trained network will behave as a *black box* in which little mathematical/physical insight can be gained. And fourth, training times are extremely long due to multimodal error surfaces which tend to trap the solution within local minima. Wavenets incorporate POD based initialization of weighting matrices which allow for much higher convergence times; the set radial basis functions also represent non linear limit cycle behavior of these flows which reduces the local minima problem.

This research proposal continues model reduction work on the shear layer and looks to validate the designed control laws in both computational and experimental studies. The reduced order model control design approach proposed is extremely powerful and can be applied to many different flow fields. The control development method is not limited to simplified flow fields, but well suited for highly turbulent, chaotic flows. Ultimately, the goal of this research proposal is to refine the method of model/controller development while applying current knowledge and techniques to different flow fields. In accompaniment with the shear layer modeling efforts, I intend to use this model reduction method for multiple flows and actuation interaction, such as cycloidal propeller for wave extraction, cycloidal propeller for MAV design, shear layer with blowing and suction slot, shear layer with plasma actuation, and modeling of structure fluid interaction.

4 Research Synopsis

4.1 Overview

Traditionally, flow fields are controlled or manipulated via passive or open loop active control techniques. Passive strategies make use of modifying aeronautical properties of the body to achieve a desired flow state. These methods add no external energy to the flow and are time invariant. Protrusions or intrusions will be added along the body's geometry to induce some type of flow change. These methods yield only small performance gains to certain flow fields, but are very easily implemented onto an aerodynamic design. A few examples of this type of flow control are winglets, fins, or dimples on a golf ball.

The other type of flow control is active control which is broken down into two subcategories: open and closed loop control. Open-loop strategies make use of actuators to force the flow at a given frequency and amplitude to induce some sort of desirable change in flow state. These actuators are typically blowing or suction slots, plasma actuators, or piezoelectric actuators. An example of this is blowing high frequency pulses along the leading edge of an airfoil to create small coherent vortex structures which prevents the onset of separation and inherently increases the angle of attack at which stalling occurs.

These above methods have been exhaustively studied by fluid dynamicists. The focus of this paper is on closed loop active flow control. Instead of the above open-loop strategies, sensors are used to feed back vital flow characteristics such as, pressure, velocity, temperature, density measurements, etc. These measurements formulate an estimate of the current flow state. This estimated state allows for state feedback through some control algorithm which prescribes an actuation command to produce a desired flow state in the flow field. This research contains multiple tasks to overcome for the overall success of these ideas such as: development of control algorithms, state estimators, and strategic sensor placement. Mainly because fluid dynamics are composed of highly complex, non-linear, stochastic processes, the development of simple, yet robust control algorithms and state estimation methods becomes extremely difficult. The Formulation of low dimensional models which accurately and robustly represent the flow over a given forcing parameter space is one approach to developing such algorithms and is explored in extensive detail in the following dissertation.

Before any type of modeling or control design efforts can be completed, a representation of the flow field shall be selected. Flow fields are represented by techniques such as full order governing equations (the Navier-Stokes equations), experimental setups, numerical approximations of the governing equations (computational fluid dynamics), linearizing governing flow equations (potential flow theory), etc. Each of these methods are well suited for flow field representation and only depend upon the resources at hand and the relevant flow features desired in the representation. Scaled models placed in wind tunnels accurately create desired flow fields but really lack with ease of measurements. Measuring techniques such as hot films, particle image velocimetry, Schlieren imagery, laser doppler velocimetry, etc. do serve as efficient means of measuring flow characterizations, but these techniques are local measurements either temporally or spatially. Measurement noise is also a significant problem for subsequent controller design, model or state estimation formulation. The governing equations depicted below by the Navier Stokes equations do represent

100% of the flow physics, but really lack in solvability.

$$\rho \left(\frac{\partial \mathbf{u}}{\partial t} + \mathbf{u} \cdot \nabla \mathbf{u} \right) = -\nabla p + \nabla \cdot \mathbf{T} + \mathbf{f} \quad (5)$$

Only a handful of solutions exist to these equations. The solutions that *do* exist are mostly related to extremely over simplified flow fields which are often of little interest from an engineering standpoint. The Navier-Stokes (NS) equations can be numerically solved, a discipline known as computational fluid dynamics (CFD). Typically, these numeric solutions are only approximate solutions to the NS equations, but they do provide extremely insightful information which can be used for analysis, design, and simulation purposes. CFD is the process of solving coupled partial differential equations by the means of finite difference methods, finite element methods, or finite volume methods. The spatial domain of the flow field is discretized into small cells which make up a volume grid or mesh. The cells are irregular shapes (i.e. rectangles, triangles, polygons, etc.) and resolved on different spatial resolutions. Direct solutions of the NS equations (DNS) for complex flows (large Reynolds number flows) is not computationally viable on today's supercomputers. The resolution of the discretization needed is proportional to the cube of the Reynolds number ($\propto Re^3$) for an accurate DNS simulation. For a turbulent flow this could be on the order of 10^{18} cells for a given simulation. For laminar flows this is not computationally difficult (as Reynolds numbers are less than 2100), but as the increase of Reynolds number, the solution becomes unrealistic. Many numeric methods to reduce computation burden while resolving the desired scales exist to accurately predict turbulent, compressible, highly complex flow fields (i.e. direct numeric simulations, large eddy simulations, detached eddy simulation, scale invariance, higher order turbulence models, combinations of methods with filters for transition areas) Meneveau and Katz [2000]. CFD allows for an accurate means of achieving a representation of the desired flow field and is typically the most widely used among current research approaches. Other flow representations such as Euler equations, potential flow, panel methods are used as well.

Feedback flow control design can be broken into two main categories. Strategies which make use of low dimensional models and strategies which use the model free approach. It is argued that the model free approach has less chance of reaching a desired performance, but may be simpler to implement, while the reduced order model approach is more time consuming formulating the model and simplifies control derivation.

The model free approach utilizes adaptive control techniques to feedback global flow variables in an experimental setting to improve flow characteristics. Becker et al. [2006] This method completely abandons modeling procedures and directly closes the loop. Control laws such as adaptive extremum seeking controllers vary open loop parameters to produce desired flow states. King et al. [2004] Moeck et al. [2007] Typically, these controllers lack desired performance, but do prove to be useful for initial experimental investigations.

The second entails using reduced order modeling procedures to formulate low dimension numerical models for controller development. These methods, while relatively time consuming and numerically intensive are able to produce simple, high performing control algorithms. Current techniques do have inherent problems with modeling and implementation of actuation, as discussed below. The focus of this paper will be on the latter method which produces *smarter* control algorithms based on reduced order models (ROM's).

For high performance, accurate control algorithms, an underlying model needs to be formulated which accurately captures the desired flow features in the analyzed flow is needed. Customarily,

low dimensional modeling for flow control purposes is a three step process. Siegel et al. [2008] A flow field in which feedback control can improve a flow variable or achieve a certain flow state is chosen. The first step involves acquiring flow data either by experimentation or numerical procedures. Selecting the correct flow variable to model is a very important step for model development. For example, streamwise velocities may be used to model the vortex shedding behind a cylinder, or the pressure field may be used to model the structures of a shear layer. Once the experiments or numeric simulations are carried out, the data is then condensed or decomposed by common techniques such as the Karhunen -Loève procedure more commonly known as the proper orthogonal decomposition (POD) method (discussed in more detail in Section 4.2.2.1). The method of snapshots provides a powerful tool for POD which allows for a more accurate decomposition based on periodic flow behavior. Sirovich [1987] The POD method allows the higher frequency/lower energy modes to be neglected, maintaining the higher energy modes, more dominant modes. This will dramatically reduced the order of the data. After the POD procedure the data will be in the form,

$$u(x, y, t) = \sum_{j=1}^{\infty} a_j(t) \phi_j(x, y). \quad (6)$$

The third and final step is developing a numerical model for these time coefficients ($a_j(t)$). Traditionally, a Galerkin Model is formulated. Here the truncated mode set ($\phi_j(x, y)$) is projected back onto the Navier-Stokes equations ($\mathfrak{F}(\cdot)$) Noack et al. [2004] Rempfer [2000] Rowley et al. [2004] Sirisup et al. [2005] Gerhard et al. [2003]. For convenience, suppose the navier stokes equations are written as the non-linear operator $\mathfrak{F}(\cdot)$

$$\frac{\partial u}{\partial t} = \mathfrak{F}(u) \quad u = u(x, t) \quad t \geq 0 \quad x \in N. \quad (7)$$

The spatial modes are then projected onto the left and right hand sides of Equation 7, such that

$$\left(\phi_i(x, y), \frac{\partial u}{\partial t} \right) = (\phi_i(x, y), \mathfrak{F}(u)) \quad i = 1, 2, \dots \quad (8)$$

Where the set of basis functions must meet the following requirements: (1) The basis must be complete meaning the basis must span the entire set of the original flow field. (2) The basis columns must be linear independent. (3) The eigenfunctions must satisfy the boundary conditions of the Navier-Stokes equations Rempfer [2000]. This projection will yield a set of ODE's which describe the evolution of time coefficients,

$$\frac{da_i(t)}{dt} = \mathfrak{F}_i(a_1, a_2, \dots). \quad (9)$$

These ODE's will be quadratic in nature due to the convective term of the Navier Stokes equations. These equations have proven useful for analyzing stability of flow fields and developing simple control algorithms. The problem is this set of equations, while mathematically accurate, is numerically unstable because of the lack of satisfied boundary conditions. Also, adding the actuation term to the set of equations in 9 tends to be very difficult. Actuation dynamics are a dominant feature of feedback control. As in Noack et al. [2004] and Rowley et al. [2004], an actuation term is superimposed on Equation 10, such that

$$\frac{da_i(t)}{dt} = \mathfrak{F}_i(a_1, a_2, \dots) + \varepsilon g. \quad (10)$$

Where g is assumed to be a body force acting at the node ε . This is a very strong, and in some flows, false assumption to make that fluid dynamics interact linearly with body forces in the flow.

An alternative approach is using system identification to produce a model for these time coefficients. System ID techniques can be broken into two main categories linear and non-linear. Linear system ID has many widespread uses and applications. Linear models really allow for a very nice analysis of the underlying system by the ability to compute stability, observability, controllability, robust and performance margins. Common methods include but are not limited to the following: output error methods, prediction error methods, subspace model identification methods, AR/AR-MAX/ARX model identification methods. These linear models really fail at capturing non-linear limit cycle/periodic behavior which is *very* common in unsteady fluid dynamics.

Fluids are governed (as discussed previously) by highly non-linear dynamics. Thus, linear system ID presents excessive modeling errors. The alternative is adopt non-linear system ID algorithms which are more difficult to formulate/train, slower to simulate, harder to analyze, but in the end more accurate than linear techniques at modeling fluid behavior. A common approach is to use non-linear Volterra kernel identification. Lucia et al. [2003] Balajewicz et al. [2009] For time invariant, non-linear, continuous time systems Volterra system ID is very good at identifying non linear behavior. To model the response, $y(t)$, of a system due to an arbitrary input, $u(t)$, a second order Volterra series is formed such that,

$$y(t) = h_o + \int_0^t h_1(t - \tau)u(\tau)d\tau + \int_0^t \int_0^t h_2(t - \tau_1, t - \tau_2)u(\tau_1)u(\tau_2)d\tau_1d\tau_2 \quad (11)$$

where $h_1(t)$ is a kernel which identifies the impulse response of the system and $h_2(t)$ is the quadratic kernel which models non-linearities. Higher order series can be expanded, but the identification of higher order kernels increases exponentially. Lucia et al. [2003] Techniques exist to prune or numerically soothe the matrix inversion process to reduce this computational burden. Griffith and G.R. [1999] The inherent problem with Volterra series is that they are strictly input output relationships, that is $y(t) = H \times u(t)$. The model doesn't identify internal dynamics of the system. Once the input becomes zero the output will go to zero. These Volterra series do have their uses in aeroelastic systems and non-linear filter design, but are not useful in the application to ROM development for feedback flow control Balajewicz et al. [2009].

Another alternative to non-linear system identification is using neural networks. Network topology ID methods are a capable of identifying strong non-linearities. They can also be modified to calculate future outputs based on previous simulated outputs; thus having the ability to model dynamics of a system. They are not limited to single input-single output (SISO) systems but are capable of simulating multi-input multi-output (MIMO) systems. They *do* have some downsides. Training is extremely sensitive, and tends to get stuck in local minima. Techniques do exist of increasing training effectiveness, but backpropagation algorithms mainly rely on increasing number of epochs and general luck in achieving global minimum Larochelle et al. [2009]. This paper will explore the technique of using Artificial Neural Networks - Auto Regressive eXogenous Siegel et al. [2008] (ANN-ARX) non-linear identification methods to produce an extremely low dimensional model for flow state simulation, reference signals and control algorithm development. Also, the ANN-ARX system ID method will be extended to include wavelet basis functions which are very well suited for modeling the non-linear periodic behavior of certain flow fields.

4.2 Theoretical Background

A closed-loop flow control system is comprised of three basic components: i) a sensor or array of sensors to sense and estimate the current flow state, ii) a controller that determines a control signal to achieve the desired flow state, and iii) an actuator that introduces the predetermined perturbation into the flow. Note that in an application, the system may have multidimensional inputs and outputs, i.e. the sensor could be comprised of an array of sensors, and the actuator could in fact be a combination of multiple actuators such as side by side blowing and suction slots. In the following description of the feedback control strategies, the wake behind a circular cylinder is considered as an illustrative example.

Model Independent Approach Involves the introduction of sensors in the wake and using a control law (usually linear) to produce a command to the actuator that forces the flow. The advantages of this approach are that:

- No model of the flow field is required for controller design
- Direct feedback eliminates the need for a state estimator
- A simple control law may be implemented in an experimental setup with relative ease

For the circular cylinder wake problem, experimental studies have shown that linear proportional feedback control based on single sensor feedback is able to delay the onset of the wake instability, rendering the wake stable at Reynolds numbers about 20% higher than the unforced case. However, above this threshold, single-sensor feedback may suppress the original vortex shedding mode but destabilize other modes Roussopoulos [1993]. While this approach is relatively simple to implement experimentally, the results are very limited for the absolutely unstable cylinder wake.

Direct Navier Stokes Approach This approach is more structured as it applies conventional and proven model-based control strategies such as optimal control theory to flow control problems. Abergel and Temam [1990] developed conditions for optimality for a few simple applications. However, from a control algorithm point of view, the complexity of the flow physics results in a control problem of very high dimensionality. Even if this strategy theoretically can yield optimal results, implementation in a real time system is not feasible since it would require the solution of the Navier-Stokes equations in real time.

Low-Dimensional Approach Low-dimensional modeling is a vital building block for realizing a structured model-based closed-loop strategy for flow control. In light of the high complexity of the control problem, a practical procedure is needed to reduce the order by capturing the essential physical processes in a low dimensional model. A commonly used method to achieve this reduction in order is proper orthogonal decomposition (POD). This method is an optimal approach in that it will capture the largest amount of the flow energy in the fewest modes of any decomposition of the flow. POD has been successfully used to identify the characteristic features, or modes, of a cylinder wake Gillies [1998], Siegel et al. [2008].

The major building blocks of this low-dimensional approach are a reduced-order POD model, a state estimator and a controller. The desired POD model contains an adequate number of

modes to enable reasonable modeling of the temporal and spatial characteristics of the large scale coherent structures inherent in the flow Holmes et al. [1996].

For low-dimensional control schemes to be implemented, a real-time estimation of the modes present in the flow is necessary since it is not possible to measure the whole flow field directly, especially not in real-time. Flow field data (e.g. velocity), provided by either simulation or experiment, is fed into the POD procedure. The temporal amplitudes of the POD modes are determined by applying a least squares fit of the instantaneous data to the spatial eigenfunctions. Then, the estimation of the low-dimensional states is provided, e.g. by using a linear stochastic estimator (LSE). Sensor measurements may take the form of velocity measurements or body-mounted pressure measurements. This process leads to the state and measurement equations, required for design of the control system. For practical applications it is desirable to reduce the information required for estimation to a minimum. The requirement for the estimation scheme then is to behave as a modal filter that ‘combs out’ the higher modes. The main aim of this approach is to thereby circumvent the destabilizing effects of observation *spillover* Balas [1978]. Spillover has been the cause for instability in the control of flexible structures and modal filtering was found to be an effective remedy.

To provide an overview of the feedback flow control design cycle used in this research project, Figure 1 shows the main building blocks in the process. The main premise of this control design approach relies on an iterative scheme which tweaks current methodologies to achieve adequate flow field to controller design time along with desirable closed loop performance. The development started with building a database of flow states based on CFD simulation results. First, the natural (i.e. without any control input) flow field was simulated. Then, a number of simulations were performed where periodic blowing and suction was used to introduce disturbances at a given frequency and amplitude into the flow. The results of all these simulations were analyzed using Proper Orthogonal decomposition (POD), which resulted in POD spatial modes as well as the POD time coefficients for each time step of all simulations. POD modes and their adjoint amplitudes for a forcing scenario provide important flow/forcing interaction characteristics. This interaction is then modeled through the time coefficients with system identification techniques outlined in following sections. The low dimensional model is then verified given off design forcing parameter cases. Once an acceptable model is formulated adaptive control methodologies can be applied. As seen in Figure 1 at each design point a possible iteration path to adjust parameters to increase model/controller performance exist along paths 1 through 4. This flowchart will be strictly followed and described within the following sections.

4.2.1 Numeric Simulation

The framework of this control design approach is based upon the use of open loop numeric simulations. The simulations were performed using COBALT from Cobalt Solutions, LLC, a commercial unstructured finite-volume code developed for the solution of the compressible Navier-Stokes equations. The basic algorithm is described in Strang et al. [1999] and Grismer et al. [1998], although substantial improvements have been made since then. The numerical method is a cell-centered finite volume approach applicable to arbitrary cell topologies (e.g, hexahedra, prisms, tetrahedra). The spatial operator uses the exact Riemann Solver of ?, least squares gradient calculations using QR factorization to provide second order accuracy in space, and TVD flux limiters to

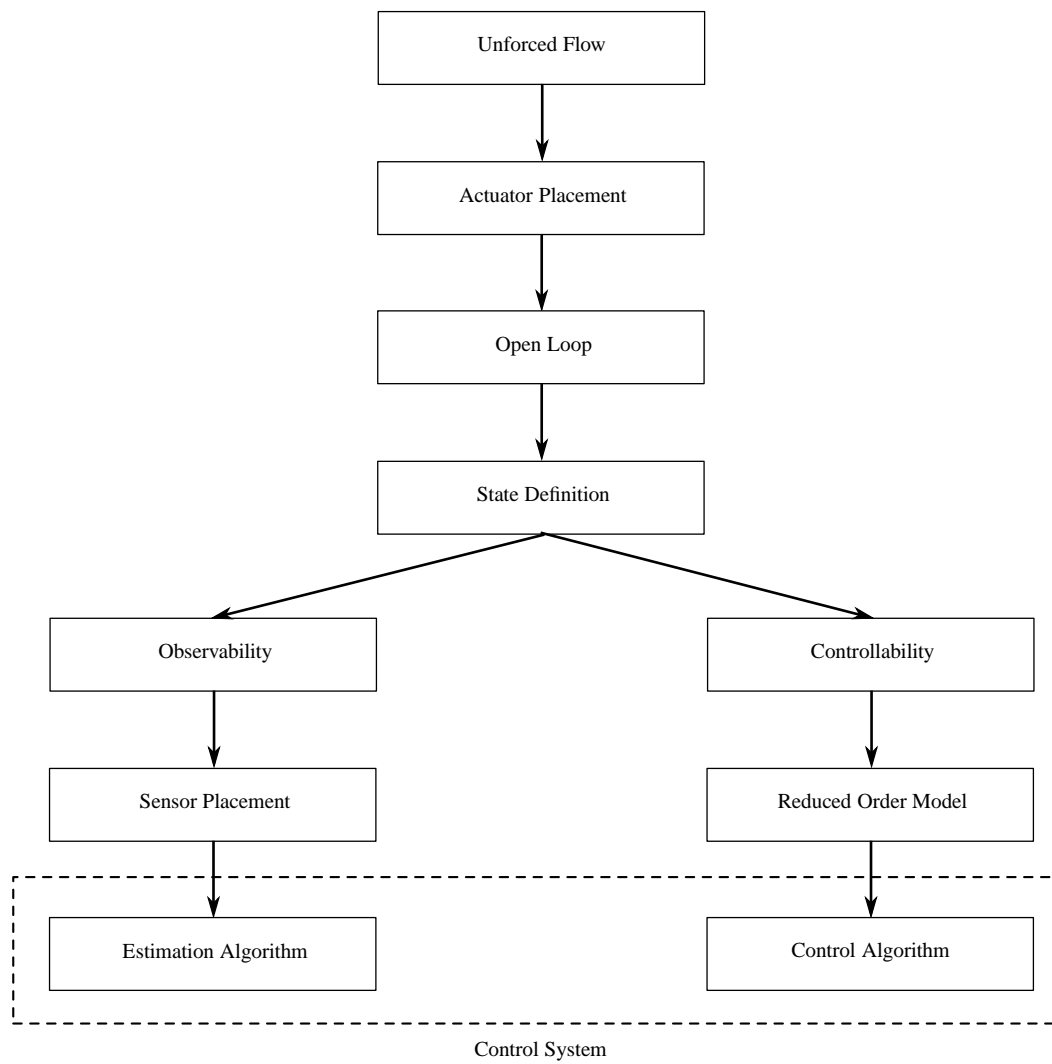


Figure 1: Flowchart of the feedback control development process.

limit extremes at cell faces. A point implicit method using analytic first-order Jacobians is used for advancement of the discretized system. For time-accurate computations, a second order accurate method with Newton sub-iterations is employed. For parallel performance, COBALT utilizes the domain decomposition library ParMETIS [Karypis et al., 1997] to provide optimal load balancing with a minimal surface interface between zones. Communication between processors is achieved using Message Passing Interface (MPI), with parallel efficiencies above 95% on as many as 1024 processors Grismer et al. [1998].

The main methods for calculating complex flows with a CFD solver are Direct Numerical Simulation (DNS), Large Eddy Simulation (LES), and Reynolds-averaged Navier Stokes (RANS). The RANS approach is the most economical since it is designed to solve for the mean flow, but it is subject to many modeling approximations. Since it models rather than resolves the bulk if not all of the turbulent motions, this would be an inappropriate choice for the current investigation. DNS, on the other hand, makes no modeling assumption but is the most expensive approach since all turbulent motions must be resolved by the grid. Since the smallest scales of turbulence (the Kolmogorov length scale) decrease rapidly with increasing Reynolds number, this approach is limited to relatively low Reynolds number flows. LES is less expensive than DNS since it models the small subgrid scales of motion and resolves the rest of the turbulent motions. However, since the large scales in the boundary layer are on the order of the boundary layer thickness (which is quite thin for high Reynolds number flows), this method is cost prohibitive at high Reynolds numbers for wall bounded flows.

Detached-Eddy Simulation (DES) is a by now well known hybrid technique [Spalart, 2000] for prediction of turbulent flows at high Reynolds numbers [see Spalart, 2000]. The motivation for developing DES was to combine the most favorable aspects of RANS and LES, i.e. the acceptable predictions using RANS models of thin, near wall shear layers (e.g. attached boundary layers) and LES for resolution of time-dependent, three-dimensional large eddies (e.g. free shear layers). For natural applications of DES, RANS is applied in the boundary layer, while outside the boundary layer in the separated region, LES is used. An array of flows ranging from building block applications such as the flow over a cylinder, sphere, aircraft forebody, and missile base to complex geometries including full aircraft have been modeled successfully using DES Travin et al. [1999], Squires et al. [2001], Constantinescu et al. [2002], Forsythe et al. [2002], Hansen and Forsythe [2003]. These and other applications illustrate the capability of DES to accurately resolve chaotic unsteady features in the separated regions along with a rational treatment of the attached boundary layers. Recent DES predictions of the flow around complex configurations (all using Cobalt) include the massively separated flow around an F-15E at 65° angle of attack reported by Forsythe et al. [2004] (this simulation was the first eddy-resolving simulation of flow around a full aircraft configuration), transonic shock-separated flow over an F/A-18E by Forsythe and Woodson [2003], and vortex breakdown on an F-18C by Morton et al. [2003, 2004].

These highly successful simulations demonstrate the capabilities of the COBALT CFD solver. In light of the aero-optics problem, it is important to note that many of the flows investigated show features similar to the ones expected to play a significant role in the aero-optics problem. In particular, the fully separated flow simulations can only accurately predict flight parameters such as lift or drag in a time dependent manner if the large scale motion is computed correctly. These same large scale structures play a significant role in the aero-optics problem as well, which made the COBALT solver a very well suited tool for the numerical aspects of this research project.

4.2.2 Reduced Order Modeling

4.2.2.1 Numerical Reduction

A dynamical system can be written as

$$\dot{\rho}(\mathbf{x}, t) = f(\mathbf{x}, t), \quad (12)$$

where \mathbf{x} is defined to be a vector over finite dimensional state space, ρ is e.g. the fluid density at a given spatial location and time, t . The right hand side of the equation is time variant, non-linear, and described by the Navier-Stokes equations. Unforced and forced simulations provide a flow data base. The forcing signal is limited to periodic input varying frequency and amplitude. The range of these parameters are chosen by perturbations to the natural shedding frequency of the flow at a range of feasibly implementable actuation limits. This parameter space provides as the basis for future investigations. The corresponding data set is designated by the matrix $\Omega \in \mathbb{R}^{n \times m}$, where n is the number of samples in time and m is the number of spatial grid points.

Data reduction schemes such as proper orthogonal decomposition (POD), also known as the Karhunen-Loève process, have been used successfully to reduce the data to manageable size Berkooz et al. [1993]. The Method of Snapshots Sirovich [1987] is used here to reduce the size of the correlation matrix. The matrix $\Omega \in \mathbb{R}^{n \times m}$ can be decomposed using singular value decomposition,

$$\Omega = U \Sigma V^*, \quad (13)$$

where U is an orthonormal matrix with dimension $m \times m$, V^* is also an orthonormal matrix with dimension $n \times n$, Σ is a diagonal $m \times n$ matrix in which the n (because typically $n < m$) singular values are arranged in decreasing order on the diagonal. The singular values of Ω are also the eigenvalues of $\Omega^T \Omega$. Next, define $Q \equiv U \Sigma$ in Equation 13, which yields

$$\Omega = Q V^*. \quad (14)$$

This can be written in summation form, as shown in Equation 15, such that q_i is the i^{th} column of Q ; likewise, v_i is the i^{th} column of V ,

$$\Omega = \sum_{i=1}^m q_i v_i^*. \quad (15)$$

Equation 15 is still an identity, i.e. no approximations have been introduced. In Equation 15 the i^{th} temporal coefficient, $a_i(t)$, is exactly equivalent to the i^{th} column of Q . Likewise, the i^{th} spatial mode, $\phi_i(x, y)$, is represented by the i^{th} row vector of V^* . The system Ω can then be written as,

$$\Omega = \sum_{i=1}^m a_i(t) \phi_i(\mathbf{x}). \quad (16)$$

For $m' < m$ the decomposition becomes,

$$\Omega \simeq \sum_{i=1}^{m'} a_i(t) \phi_i(\mathbf{x}). \quad (17)$$

where now the right hand side is an approximation of Ω . Because the singular values can be related to the energy of the modes and are arranged from largest to smallest ($\sigma_1 > \sigma_2 > \dots > \sigma_n$), the dominant spatial and temporal modes appear first in the matrices U and V , respectively.

Therefore, plots of the singular values are normally shown to determine where a truncation of a model is appropriate. For example, for the cylinder wake flow field 98% of the energy in the flow is contained within the first three modes. Reducing m' to three represents a significant reduction in the model order even though the model still maintains the dominant flow physics Siegel et al. [2008].

The above decomposition is a good approximation for a periodic flow field, but in feedback control, the flow is being forced through some (arbitrary) actuation and therefore not periodic, even if it would be naturally. This means that the flow will undergo some transient development, which results in the spatial modes ($\phi_i(\mathbf{x})$) evolving over time. Siegel et al. [2008] devised a strategy called Double Proper Orthogonal Decomposition (DPOD) to accurately model this transient behavior. In DPOD, the POD process is used twice to capture the transient phenomenon in the spatial modes. The second decomposition represents the spatial mode fluctuations over time which capture forcing-flow interaction. The DPOD decomposition is written as,

$$\Omega = \sum_{i=1}^{m'} \sum_{j=1}^{n'} a_{ij}(t) \phi_{ij}(\mathbf{x}). \quad (18)$$

The resulting spatial modes form a $m' \times n'$ mode set which accurately represents the unforced, forced and flow state transitions from one to the other. For more information on the DPOD process see Siegel et al. [2008].

4.2.3 System Identification

The system identification step as presented in Fagley et al. [2010] is a crucial step in formulating the low dimensional model. Numeric decomposition parameters such as: forcing parameters, spatial domain, and numerical decomposition method (DPOD, SPOD, POD..etc.) are determined by a parameter study. The next task for defining a reduced order model was the development of a mathematical model which accurately represents the time coefficients of the POD mode set. The formulation of a reduced order model which accurately relates the forcing input to the evolution of the time coefficients would give capability to predict a flow state not present in the original dataset. These predicted time coefficients, multiplied with the spatial modes, would yield a prediction of the flow field at any instant in time within some confidence interval.

For model development, the Galerkin method has been typically used to project a truncated mode set onto the Navier Stokes equations, resulting in a set of ordinary differential equations [see e.g. Berkooz et al., 1993]. However, it has been realized that the resulting equations are mathematically unstable, that the resulting model cannot satisfy the boundary conditions due to POD truncation. Also a linear flow interaction with actuation is taken into account through the body force term in the Navier-Stokes equations Rempfer [2000]. Nonetheless, these reduced order models provide insight into the flow physics and basic controller design. Galerkin models lack of actuation characterization poorly models the dynamics of typical actuation methods such as blowing and suction slots or plasma actuators. The body force assumption does not capture forcing dynamics of a blowing and suction slot in which the mass flow rate is actually changing through a prescribed location.

These shortcomings of the Galerkin model drive this research project a different direction. System identification techniques were used to identify a model which accurately represents the

open loop forcing dynamics of the flow field. Writing the system in Equation 17 with the density of the flow as the kernel,

$$\rho(\mathbf{x}, t) = f(\mathbf{x}, t, u) \simeq \sum_{i=1}^{m'} a_i(t, u) \phi_i(\mathbf{x}|u), \quad (19)$$

where $\mathbf{x} \in \mathbb{R}^n$, $t_o \leq t \leq t_1$ and $u(t|F, A) = A \sin(2\pi Ft)$, provides the basis for applying system identification tools. In order to understand the evolution of the density field, $\rho(\mathbf{x}, t)$, in time, its derivative must be found,

$$\dot{\rho}(\mathbf{x}, t) \simeq \sum_{i=1}^{m'} [\dot{a}_i(t, u) \phi_i(\mathbf{x}|u) + a_i(t, u) \dot{\phi}_i(\mathbf{x}|u)]. \quad (20)$$

The second term, $a_i(t, u) \dot{\phi}_i(\mathbf{x}|u)$, drops out because ϕ is time invariant, so all of the nonlinearities of the system are contained within the evolution of the mode amplitudes $\dot{a}_i(t|u)$. System identification was then used to provide a mathematical representation of the evolution of these mode amplitudes. Here the system can be represented in state space form as

$$\begin{cases} \dot{a}(t, u) = G(a(t, u)) \\ \rho(\mathbf{x}, t) \simeq \phi(x|u)a(t, u) \end{cases} \quad (21)$$

where $G(a(t, u))$ is an unknown, non-linear, time invariant function. In discrete time, this system is

$$\begin{cases} a(t_{k+1}, u_{k+1}) = G(a(t_k, u_k)) \\ \rho(\mathbf{x}, t_k) \simeq \phi(x|u_k)a(t_k, u_k). \end{cases} \quad (22)$$

The modeling goal was to formulate a mathematical model which represented the time coefficients of the numerical approximation over the open loop forcing parameter space, $u(t|F, A)$. Nonlinear autoregressive exogenous (NLARX) systems were used to identify the behavior of the mode amplitudes, for which a regression vector was formed such that

$$\Theta(t) \equiv [u(t) \dots u(t - n_u), a_1(t - 1) \dots a_1(t - n_{a_1}) \dots a_i(t - 1) \dots a_i(t - n_{a_i})]. \quad (23)$$

Nonlinear mathematical models were then trained to minimize the error between the training set and predicted output in a least squares sense.

Many methods for nonlinear system identification exist. Previous work used artificial neural network autoregressive exogenous (ANN-ARX) systems to identify the dynamical behavior of the time coefficients in the forced cylinder wake Siegel et al. [2008]. Neural networks are widely used in the scientific community for process modeling, artificial intelligence, pattern recognition, machine learning, etc. This nonlinear system identification technique has been argued to be a universal approximator, capable of representing any type of data trend Norgaard et al. [2003]. However, some inherent problems of ANN models exist. First, there is no straight forward method for designing the network, including determining the number of hidden neurons, the number of layers, or the parameters of the regression vector. Furthermore, training relies heavily on trial and error to find a combination of parameters that yields acceptable results. Second, the convergence of these networks depends strongly upon the initial (usually random) weights in the weighting matrices. This can lead to drastically different results when training a single network with different

sets of parameters. Third, a properly trained network will behave as a *black box* from which little mathematical and physical insight can be gained. And fourth, training times are extremely long due to multimodal error surfaces which tend to trap the solution in local minima, which also contributes to the vastly different network parameters obtained from the random data initialization.

A different way to formulate a model is by using wavelet transformations, which are known for their ability to compress, decompose, and approximate scientific data sets accurately and efficiently. They are used in many technical fields including image processing, edge detection, large scale monitoring processes, transient detection, etc. Mathematically, the *mother wavelet*, Ψ , can be written as

$$\Psi(t)_{u,s} = \Psi\left(\frac{t-u}{s}\right), \quad (24)$$

where u denotes the shift or translation and s denotes the dilation or frequency content of the wavelet basis function. In the current modeling approach, wavelets were used as transfer functions to create a wavelet neural network (WNN). These wavenets were first introduced by Zhang et al. and have been applied to many areas such as functional approximation, system identification, adaptive control, and non-linear modeling and optimization Zhang and Benveniste [1992], Zhang et al. [1995], Chen and Bruns [1995], M.M. Polycarpou and Weaver [1997]. An example of the formulation of a wavelet based ARX network is Zhang and Benveniste [1992]

$$\hat{f}(t) = \sum_{i=1}^N w_i \Psi(s_i(t - u_i)) + c^T t + f_0, \quad (25)$$

where w_i are the weights, Ψ is the wavelet function, N is the number of wavelet functions, c^T represents the linear connections, and f_0 is the bias. The WNN is typically initialized using a dyadic wavelet decomposition Oussar and Dreyfus [2000]. The above parameters are updated via a gradient descent method to minimize the cost function

$$J_\theta = \|\hat{f}(t) - f(t)\|^2. \quad (26)$$

Multiple techniques exist to design the architecture of such wavenets. One technique is to replace the existing transfer function of a neural network (usually sigmoid or signum functions) with a radial basis wavelet. Another approach for integrating these two ideas is to use the wavenet as a preprocessing filter for the non-linear ANN identifier. An example of this type of network is shown in Figure 2, which was used by Angrisani et al. [1998] to identify transients in power signals. This approach was taken in the current research to design wavenets for feedback flow control applications.

The fundamental WN structure used for this approach to model the system in Equation 22 is

$$\hat{a}_j(t_k|\Theta_j) = \underbrace{(\Theta_j - r)PL}_{linear} + \underbrace{\sum_{i=1}^n a_{s_i} f(b_{s_i}(\Theta_j - r)Q - c_{s_i})}_{scaling\ block} + \underbrace{\sum_{i=1}^n a_{w_i} g(b_{w_i}(\Theta_j - r)Q - c_{w_i})}_{wavelet\ block} + d \quad (27)$$

where r is the mean of the regression vector, P is the linear subspace, L are the linear weights, Q is the nonlinear subspace, a_{s_i} are the scaling block coefficients, b_{s_i} are the scaling block dilations, c_{s_i} are the scaling block translations, a_{w_i} are the wavelet block coefficients, b_{w_i} are the wavelet block dilations, c_{w_i} are the wavelet block translations.

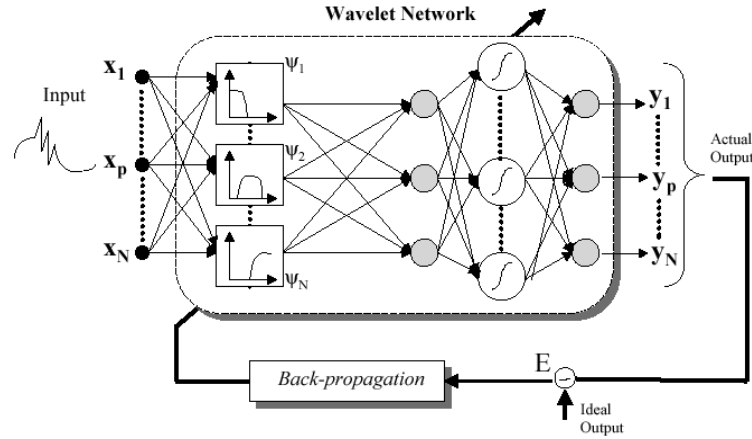


Figure 2: Training method for Wavenet ARX system which updates frequency and ANN parameters during single back propagation iteration Angrisani et al. [1998].

Moreover, $f(x)$ is the scaling function. Here, the scaling function was chosen to be a class of radial basis function such that

$$f(x) = e^{-\frac{1}{2}\|x\|_2^2} \ni f : \mathbb{R}^n \rightarrow \mathbb{R}. \quad (28)$$

Likewise, $g(x)$ is the wavelet basis, which is also a radial basis function in the form

$$g(x) = (\|x\|_0 - \|x\|_2^2) e^{-\frac{1}{2}\|x\|_2^2} \ni g : \mathbb{R}^n \rightarrow \mathbb{R}. \quad (29)$$

Examples of these basis functions are shown in Figure 3. Notice that these are continuous functions with defined derivatives over an infinite domain.

The linear and nonlinear subspace matrices (P and Q , respectively, in Equation 27) were initialized by a principal component analysis based on an optimal representation of the system linearities in the linear block as well as the nonlinear block. Given a set of initial parameters for the WN, the model simulation was performed and the global error of the training data was determined as $a_j(t) - \hat{a}_j(t)$. The parameters of the WN were then updated via a gradient descent method to minimize the error.

A graphical representation of this network is shown in Figure 4. The regression vector is presented to the three blocks as discussed above. The network simulates the estimated output for the entire training set, computes the error and updates the network parameters in Equation 27. Wavelets as a set of basis functions, represented in Equation 27, allow for a basis which represents a variable frequency domain (by the adjustment of the dilation parameter, b_{wi}). The frequency rich, nonlinear limit cycle behavior of the two dimensional shear layer was accurately represented by the set of wavelet basis, $[(g)(x)(f)(x)]$, as shown below.

A number of parameters needed to be determined to find a suitable wavenet model which accurately represented the density states of the flow field. The first parameter was the composition of the regression vector, Θ_j . This regression vector was composed of previous time histories of simulated mode amplitudes and current and previous inputs to the system. The total time history encapsulated by the regression vector determined the amount of memory the model had. However, large regression vectors drastically increase training times and may possibly increase the final

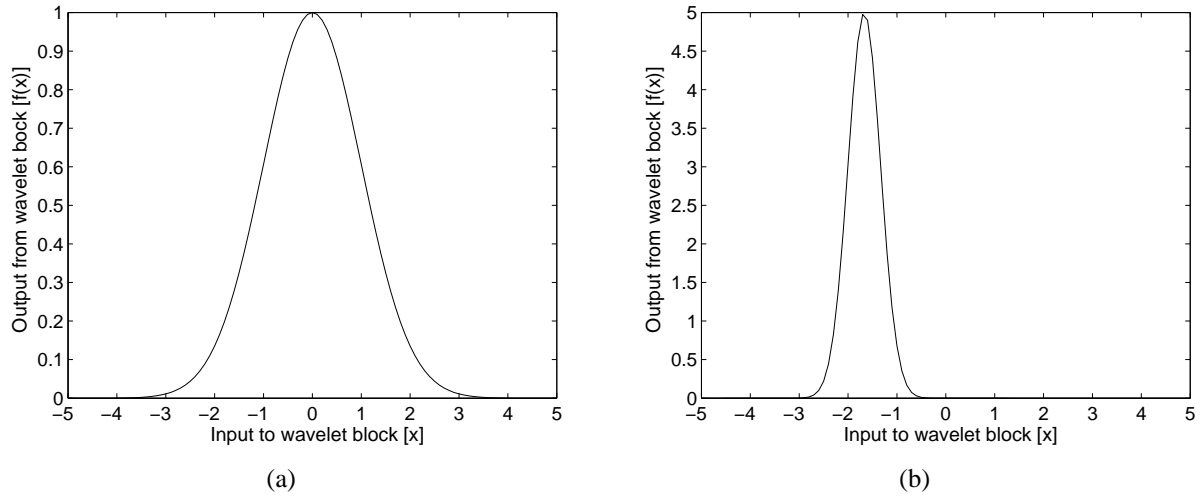


Figure 3: Example of wavelet transfer functions $f(x)$ for given scaling, dilation, and translation parameters.

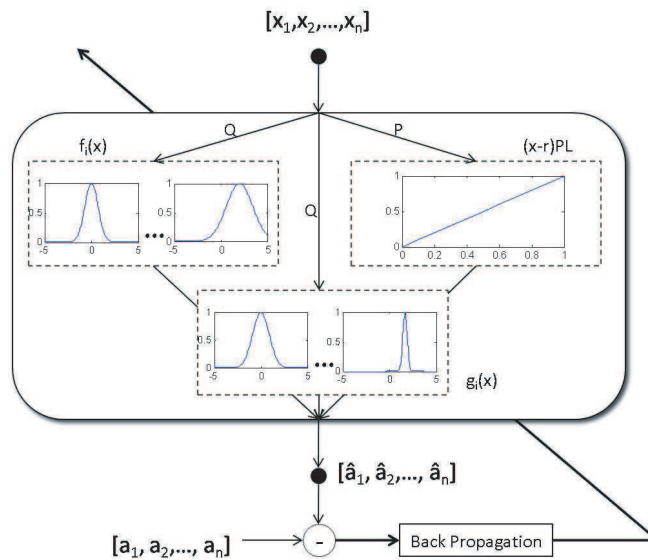


Figure 4: Graphical representation of the current wavenet approach for identifying the evolution of time coefficients. Back propagation was used to update parameters in Equation 27 in a least squares fashion.

simulation error. For periodic systems, typical time histories should approximately include one fourth of a period of the predicted output.

4.2.4 Feedback Control

4.2.4.1 State Estimation The estimator design process is extremely important. The main idea is described in ?. The state estimator will relate an array of surface mounted sensor signals, defined as $p(x_s, t)$, to the flow state which is modeled by the time coefficients of a POD truncation ($a_j^f(t)$ in equation 17) (Note: the f superscript designates that the parameter was *in flow* and the s superscript designates that the parameter was *on surface*). The goal here is to take an experimentally feasible number of surface mounted sensors (pressure transducers for example) and through a mathematical modeling technique, formulate a mapping of sensor signals to the flow state. Having access to the current flow state allows for state feedback flowcontrol. The process to developing this mathematical relation is describe below.

4.2.4.2 Sensor Placement A heuristic approach to sensor placement is used in this study. Locations correlated spatially to desired flow features (e.g. vortex shedding, vortex pairing, boundary layer growth, separation points, etc.) are chosen and defined as (x_s) within the numeric simulation. A surface POD analysis,

$$p(x_s, t) \simeq \sum_{p=1}^k a_p^s(t) \phi_p^s(x_s), \quad (30)$$

yields surface POD modes $\phi_p^s(x_s)$. The resulting locations of the maxima and minima of the surface modes show where the largest variability of the signal occurs; hence, they indicate preferred locations for sensorsCohen et al. [2003b]. The corresponding surface POD analysis allows for the reduction of the number of sensors needed to accurately estimate the surface POD mode amplitudes.

The surface time coefficients (a linear pre-filter) are then computed by solving for $a_p(t)$ in equation (30), given a particular simulation, using

$$a_p^s(t) = p(x_s, t) \phi_p^{s-1}(x_s). \quad (31)$$

The matrix $\phi_p^s(x_s)$ provides the linear subspace, with $\dim(a_p^s(x_s)) \leq \dim(x_s)$, on which the sensor signals are projected. The state vector is then given by

$$\theta(x_s|t) = \begin{bmatrix} p(x_s, t) \phi_p^{s-1}(x_s) \\ p(x_s, t) \end{bmatrix}, \quad (32)$$

which will be estimated using state estimation methods. The estimator will yield a model for the POD time coefficients in which the flow state is estimated by the linear or non-linear mapping of the state vector through the function \mathbb{G} ,

$$a_j^f(t) \simeq \mathbb{G}(\theta(x_s|t)). \quad (33)$$

In the following, the most prevalent estimation techniques for feedback flow control are outlined.

4.2.4.3 Linear Stochastic Estimation Linear stochastic estimation (LSE) is chosen as the baseline estimation method. Since flow fields of interest are typically highly non-linear, the performance of this method usually tends to be poor. The LSE method is also a static estimator, meaning no time histories of the sensor signals are used to improve the mapping performance. Nevertheless, a linear analysis is always important because it serves as a benchmark comparison for the more complex, non-linear system ID methods. For the LSE method, the estimated state $\hat{a}_j^f(t)$ is obtained from a linear mapping through matrix L where $L \in \mathbb{R}^{n \times m}$ with m is the dimension of the sensor measurements, n the dimension of the state space. The LSE operator is given by,

$$\hat{a}_j^f(t) = L\theta(x_s|t). \quad (34)$$

The observation matrix, L , is obtained by correlation of the data, such that

$$L_{ij}E(\theta(x_s|t)_i\theta(x_s|t)_j) = E(a_i^f(t)\theta(x_s|t)_j), \quad (35)$$

where $E(\cdot)$ is the expected value. This can also be written as,

$$L = BA^{-1} \text{ where } B = E(\mathbf{a}^f(t)\theta(x_s|t)^T) \text{ and } A = E(\theta(x_s|t)\theta(x_s|t)^T), \quad (36)$$

Noting that the span of L is limited to the number of sensors. Likewise, the number of states must be smaller than the number of sensors for this estimation method. This method allows for very quick computation and simple set up within simulation and experimental settings. LSE is highly sensitive to noise and requires a large array of sensors to provide accurate estimates.

4.2.4.4 Artificial Neural Network Estimation Artificial neural network estimators (ANNE) are a powerful non-linear system identification method Cohen et al. [2007]. A two layer feed forward network is used in this study to map the sensor signals to the current flow state. The first layer implements the *tanh* transfer function while the second layer consists of linear neurons. Previous time histories of the sensor data are used in the ANNE effort such that the estimation is autoregressive (AR). The regression vector x is formulated by concatenating current and previous state vectors,

$$x(t) \equiv \begin{bmatrix} \theta(x_s, t) \\ \theta(x_s, t - t_1) \\ \vdots \\ \theta(x_s, t - t_n) \end{bmatrix}. \quad (37)$$

The regression vector is then presented to the network which can be written as

$$\hat{a}_j^f(t) = W_O \tanh(W_I x(t) + b_I) + b_O, \quad (38)$$

where W_I , W_O are the input and output matrices, respectively, and b_I and b_O are the input and output biases. During network training, the global error for a given training data set is estimated and the weighting matrices along with the bias weights are updated via the gradient descent method to minimize the estimation error.

4.2.4.5 Wavenet Estimation Wavenet estimation (WNE) methods combine the network architecture of the above ANNE method with wavelet basis functions. Wavenets were first introduced by Zhang et al. and have been applied to many areas such as functional approximation, system identification, adaptive control, and non-linear modeling and optimization. Zhang and Benveniste [1992], Zhang et al. [1995], Chen and Bruns [1995], M.M. Polycarpou and Weaver [1997] Multiple techniques exist to design the architecture of such wavenets. One technique is to replace the transfer functions of a neural network with a wavelet basis function. Another approach for integrating these two ideas is to use the wavenet as a preprocessing filter for the non-linear artificial neural net (ANN) identifier. In this research, a combination of these two methods is used. The model structure is decomposed into three blocks, a linear block, a preprocessing scaling block, and a wavelet block. The AR model is then trained to accurately estimate the frequency rich, highly non-linear POD modal amplitudes. The fundamental WN structure to model the system $a_j^f(t) = \mathbb{G}(x(t))$ is

$$\hat{a}_j^f(t) = (x-r)PL + \sum_{i=1}^n a_{s_i} f(b_{s_i}(x-r)Q - c_{s_i}) + \sum_{i=1}^n a_{w_i} g(b_{w_i}(x-r)Q - c_{w_i}) + d, \quad (39)$$

where r is the mean regression vector, P is the linear subspace, Q is the non linear subspace, L are the linear coefficients, a_{n_i} are the wavelet coefficients, b_{n_i} are the wavelet dilations, c_{n_i} are the wavelet translations, and $f(x)$ is the scaling function. In this investigation, the scaling functions were chosen to be a class of radial basis function such that

$$f(x) = e^{-\frac{1}{2}\|x\|_2^2} \ni f : \mathbb{R}^n \rightarrow \mathbb{R}. \quad (40)$$

Likewise, $g(x)$, the wavelet basis, is also a radial basis function of the form

$$g(x) = (\|x\|_0 - \|x\|_2^2) e^{-\frac{1}{2}\|x\|_2^2} \ni g : \mathbb{R}^n \rightarrow \mathbb{R}. \quad (41)$$

The linear and non-linear subspace matrices (P and Q , respectively, equation 39) are initialized by a principal component analysis based on an optimal representation of the system linearities in the linear block as well as the non linearity block. Given a set of initial parameters for the WN, the model simulation is performed and the global error of the training data is determined as $a_j(t) - \hat{a}_j(t)$. The parameters of the WN are then updated via a gradient descent method to minimize the cost function

$$J_\theta = \|a_j^f(t) - \hat{a}_j^f(t)\|^2. \quad (42)$$

4.2.4.6 Adaptive Control A feedback law needs to be developed to control the model as seen in (99). This equation is written again as follows,

$$\begin{cases} \dot{a}(t, u) = G(a(t, u)) \\ \rho(\mathbf{x}, t) \simeq \varphi(x|u)a(t, u) \end{cases} \quad (43)$$

The WNARX model estimates a given flow state based on forcing input and dynamics of the system as seen by (27). The closed loop goal is to regulate (i.e. force a particular state to zero); thus, reducing active vortex shedding and achieving a desired closed loop flow state. Direct adaptive control law was chosen to close the loop. This method of control allows for unforeseen uncertainties when scaling the controller up to feedback CFD simulations and experiments.

The ROM in (27) allows for relatively short simulation times to pre-condition an adaptive controller. Adaptive control theory demands a linear system to prove stability. The model in (27) is highly non-linear. Linearizing would lose many of the flow effects which were desired in the model in the first place. To develop an adaptive strategy, satisfy stability and bounded trajectory issues, the model can be written as,

$$\begin{cases} \dot{\mathbf{x}} = \mathbf{A}\mathbf{x} + \mathbf{B}\mathbf{u} \\ \mathbf{y} = \mathbf{C}\mathbf{x} \end{cases} \quad (44)$$

Even though flow fields are highly non-linear and linearization is often a poor approximation, there is still information to be learned from the linear model. Suppose the adaptive control goal is to have the output of the plant go to zero, commonly known as output regulation, that is

$$\mathbf{y}_{t \rightarrow \infty} \rightarrow 0. \quad (45)$$

Suppose there exists a G_* which moves the system along some ideal trajectory, such that the closed loop system can be written as

$$\dot{\mathbf{x}} = \underbrace{(\mathbf{A} + \mathbf{B}\mathbf{G}_*)}_{\mathbf{A}_c} \mathbf{x}. \quad (46)$$

Of course G_* is unknown so assume that G can be composed into an ideal portion with a perturbation, that is $G = G_* + \Delta G$. The system input then becomes $\mathbf{u} = G_*\mathbf{y} + \Delta G\mathbf{y}$. The closed loop system then appears as,

$$\begin{cases} \dot{\mathbf{x}} = \mathbf{A}_c\mathbf{x} + \underbrace{\mathbf{B}\Delta G\mathbf{y}}_{\mathbf{w}} \\ \mathbf{y} = \mathbf{C}\mathbf{x} \end{cases} \quad (47)$$

Here a Lyapunov energy function can be defined as $V(\mathbf{x}) \equiv \frac{1}{2}\mathbf{x}^T \mathbf{P}\mathbf{x}$ with \mathbf{P} a positive definite, symmetric matrix. The derivative along a trajectory is given by $\dot{V}(\mathbf{x}) = \nabla V f(\mathbf{x}) = \mathbf{x}^T \mathbf{P} [\mathbf{A}_c\mathbf{x} + \mathbf{B}\mathbf{w}]$. With some algebraic manipulation the following relation can be found,

$$\dot{V}(\mathbf{x}) = \frac{1}{2}\mathbf{x}^T [\mathbf{P}\mathbf{A}_c + \mathbf{A}_c^T \mathbf{P}] \mathbf{x} + \mathbf{x}^T \mathbf{P}\mathbf{B}\mathbf{w}. \quad (48)$$

The famous Lyapunov equation is seen here

$$\mathbf{P}\mathbf{A}_c + \mathbf{A}_c^T \mathbf{P} = -\mathbf{Q}, \quad (49)$$

which states that if a solution $(-\mathbf{Q})$ to the matrix equation above exists then the derivative along trajectories will be less than zero ($\dot{V}(\mathbf{x}) \leq 0$) and the resulting equilibrium point will be *stable*. Equation 48 can be expressed as,

$$\dot{V}(\mathbf{x}) = -\frac{1}{2}\mathbf{x}^T \mathbf{Q}\mathbf{x} + \mathbf{y}^T \mathbf{w} \text{ with } \mathbf{P}\mathbf{B} = \mathbf{C}^T. \quad (50)$$

This energy function obviously shows a dissipation term $(-\frac{1}{2}\mathbf{x}^T \mathbf{Q}\mathbf{x})$ and a generation term $(\mathbf{y}^T \mathbf{w})$. The goal of our adaptive system will be to cancel out this external power term with feedback control. That is ΔG needs to be designed such that the $\dot{V}(\Delta G) = -\mathbf{y}^T \mathbf{w}$, to ensure we have a stable system.

$$\dot{V}(\mathbf{x}\Delta G) = \dot{V}(\mathbf{x}) + \dot{V}(\Delta G) = -\frac{1}{2}\mathbf{x}^T \mathbf{Q}\mathbf{x} + \mathbf{y}^T \mathbf{w} - \mathbf{y}^T \mathbf{w} \leq 0 \quad \forall \mathbf{x}. \quad (51)$$

Define a new energy function $V(\Delta G) \equiv \frac{1}{2}tr(\Delta G \gamma^{-1} \Delta G^T)$ with $\gamma > 0$. The derivative along trajectories is calculated to be

$$\dot{V}(\Delta G) = tr(\dot{\Delta G} \gamma^{-1} \Delta G^T). \quad (52)$$

Now, it was found to be that $\dot{\Delta G} = -\mathbf{y}\mathbf{y}^T \gamma$ so that,

$$\dot{V}(\Delta G) = tr(-\mathbf{y}\mathbf{y}^T \gamma \gamma^{-1} \Delta G^T) = -tr(-\mathbf{y}\mathbf{y}^T \Delta G^T) = -tr(\mathbf{w}^T \mathbf{y}) = -\mathbf{w}^T \mathbf{y}. \quad (53)$$

Which satisfies our condition in Equation 51. In summary adaptive feedback control will be stable if the following criteria is satisfied.

$$\left\| \begin{array}{l} PA_c + A_c^T P = -Q \\ PB = C^T \end{array} \right. \quad (54)$$

These conditions are also satisfied if the system is strict positive real (SPR) with no non-minimum phase zeroes. Simply written as,

$$A_{SPR} \iff CB > 0 \& \text{Minimum phase open loop system} \quad (55)$$

This process is done exactly the same for discrete time systems; the only difference is that for strict positive realness, the so called Kalman-Yacubovic equations Fuentes and Balas [2000] must be satisfied. Which are (for some $\varepsilon > 0$),

$$\begin{aligned} A^T P A - P &= -Q = -(2\varepsilon P + L^T L) \\ A^T P B &= C^T - L^T W \\ D + D^T &= W^T W + B^T P B. \end{aligned} \quad (56)$$

The main difference here is that the D term cannot be zero for strict positive real discrete system. The analysis above for continuous time is analogous to the discrete time system.

5 Applications

5.1 Cylinder Wake

The DPOD ANN-ARX adaptive control design approach was first successfully used on a much simpler flow field, the cylinder wake. The overall goal of this project was to actuate the cylinder through an oscillating displacement to reduce the Von-Kármán vortex street. Decreasing the strength of these vortices reduces the amount of energy put into the wake of the flow; thus, minimizing the drag upon the cylinder. This project was taken from theoretical formulation to numerical simulation to reduced order modeling techniques to experimentation validation. The cylinder wake allowed for a benchmark flow for the development of this dynamic model/control design approach. More comprehensive results can be seen in Fagley et al. [2009], Siegel et al. [2008].

The Von-Kármán vortex street creates an oscillating lift force on the cylinder. This lift force well represents the natural vortex shedding frequency and strength. The natural shedding frequency for this wake was approximately 5.6 Hz. Figure 5 shows a forcing simulation, with a frequency equal to that of the natural shedding frequency, of the cylinder wake in which the forcing was started at exactly 180° out of phase from the lift force. As seen in the figure, the lift force goes through a transient period whilst the drag decreases. The flow then begins to lock in with the forcing and the drag returns to the initial value. This transient phenomenon is important to see because it shows that open loop forcing can produce a desirable flow state for a short period of time; thus, giving feedback control a promising outcome.

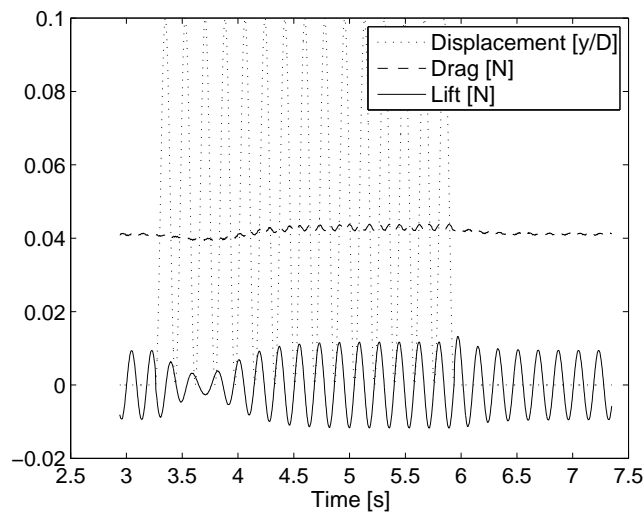


Figure 5: Actuation of cylinder wake 180° out of phase. The resulting transient period is seen between 3.25 to 4s. The reduction of drag is directly related to the magnitude of the limit cycle of the lift force.

Forcing parameter cases as seen in Figure 8 were simulated with CFD software such as *Cobalt Solutions*. The simulations were then put through the DPOD process. The DPOD spatial modes are seen in Figure 6 and the DPOD time coefficients are seen in Figure 7. The spatial modes in the first column of Figure 6 are the *main modes*, that is they are a result of the first POD decomposition. The spatial modes in the second column of Figure 6 are the *shift modes* which

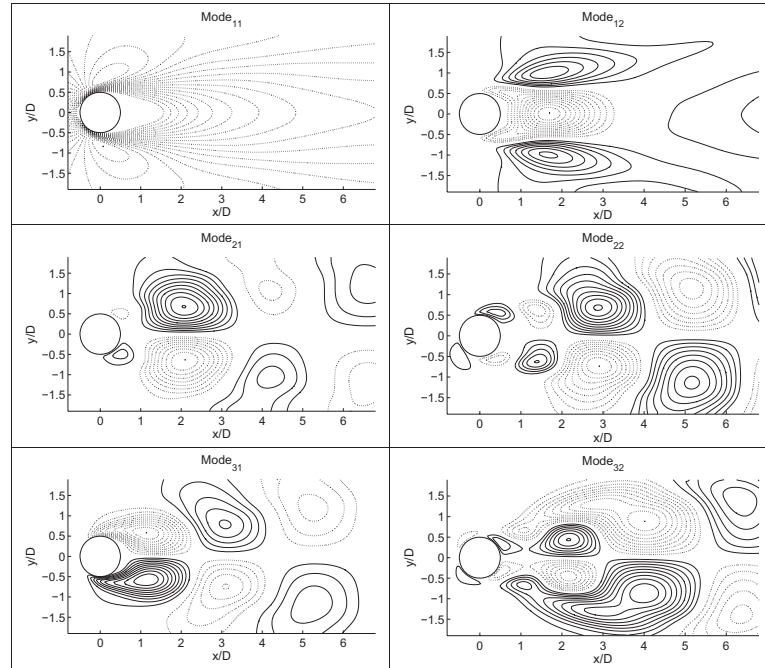


Figure 6: A transient forced DPOD spatial mode set using one shift mode for each main mode, the first 3 x 2 DPOD modes are shown. Iso-contours of streamwise velocity are shown, solid lines are positive, dashed lines negative.

show the transient affect as discussed above. The mode set was reduced to 3×2 set based on energy profile analysis. This mode set contains nearly 99.8% of the flow Siegel et al. [2008]. Once the DPOD temporal and spatial mode sets are formulated, they are validated for off design flow cases. Errors for this validation are on the order of $0.5\% \rightarrow 1\%$. This is a very acceptable range of error percentages. Once the DPOD mode set is validated, the time coefficients, as seen in Figure 7, for the selected training data are then concatenated and the dynamic ANN-ARX model is trained. Choosing an adequate training data is an important modeling step for feedback flow control. At first training data in which the flow locked-in with forcing actuation was used to formulate the model. This model had poor close loop dynamical behavior and the training data needed to be revised. More cases were added, as seen in Figure 8 and, more importantly, more transient cases were added in which the flow field didn't lock in with the actuation. These lower amplitude forcing cases produced very long, non-linear transients. The model then accurately predicted closed loop behavior as discussed later.

The neural network topology is an important factor for realizing the non-linear behavior of the data to be identified. Typically, neural networks consist of three layers: input, hidden and output. Activation functions are also determined for each of the neurons. The sigmoid function is the most commonly used function due to the continuity of the function for back propagation derivation training algorithms. Other parameters are also important for the functionality of the network model. The number of neurons allows the network to fit more complicated non-linear trends. Eventhough, the more neurons a network contains the more likely the model will be *overtrained* and poorly simulate off-design data. Also, training times will be greatly increased. The number of past inputs

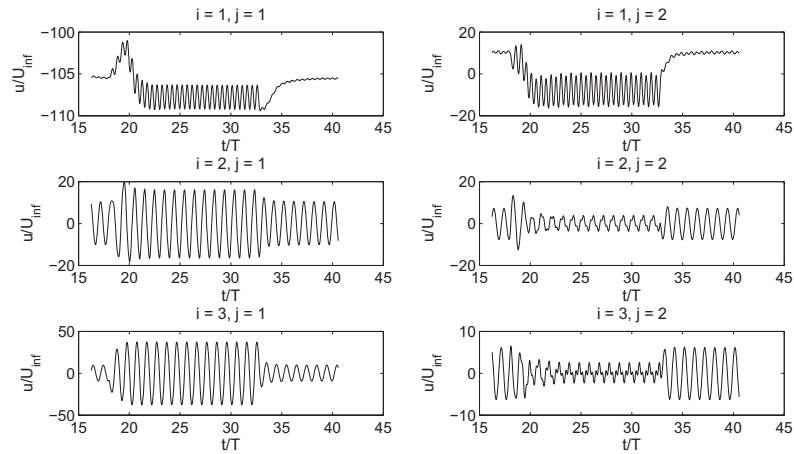


Figure 7: Mode Amplitudes a_{ij} of the open loop forced simulation $\frac{f}{f_0} = 1$ and $\frac{A}{D} = 0.25$. Forcing activated at $\frac{t}{T} = 18$ and stopped at $\frac{t}{T} = 33$, after 15 full forcing cycles. The first 3 x 2 DPOD mode amplitudes are shown.

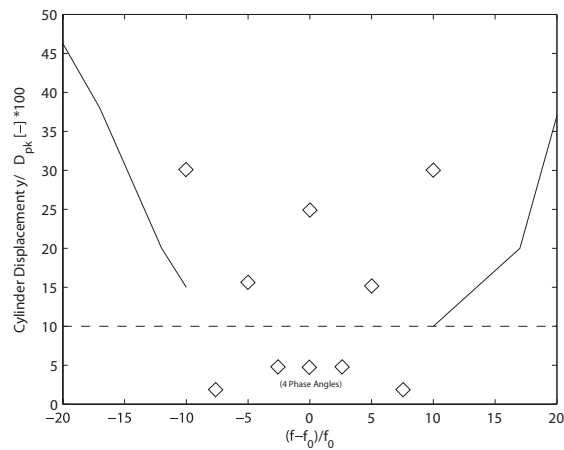


Figure 8: Training data set used for ANN-ARX identification. Lower amplitude forcing near natural frequency produced slow, large transients.

Table 1: ANN-ARX 3x2 model parameters

Input	# Past Inputs	Sampling Delay	Total Time History
Re Number	1	10	10
Actuator Position	4	2	8
$a_{1,1}$	1	1	1
$a_{2,1}$	3	8	24
$a_{3,1}$	3	8	24
$a_{1,2}$	1	1	1
$a_{2,2}$	1	12	12
$a_{3,2}$	1	12	12

and time histories of previous simulated outputs also is a crucial design factor. A new feature was added which allows for a time tapped delay so every n^{th} point will be sampled. This gives for a much larger time history while keeping the number of inputs lower which yields much shorter training times. All of these parameters were adjusted, trained, and repeated until a proper model was found. The parameters can be seen in the Table 1.

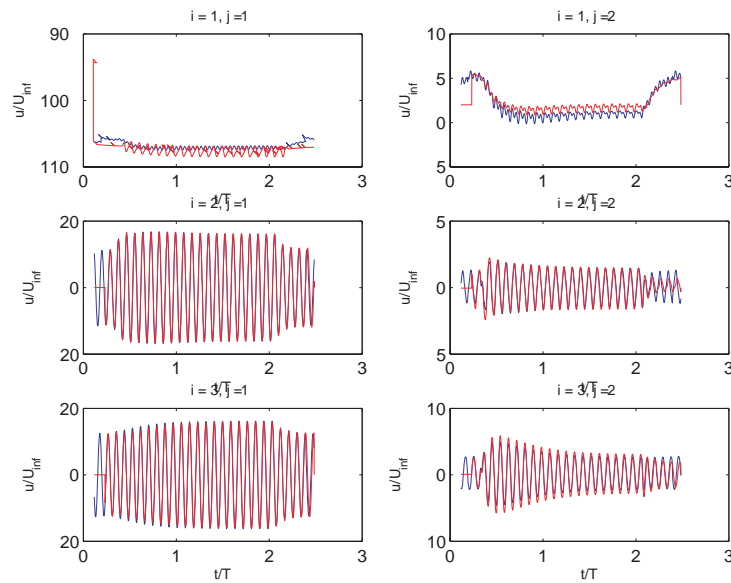


Figure 9: Off design validation of ANN-ARX model. Forcing case for $\frac{f-f_o}{f} = 0$ and $\frac{y}{D_{cyl}} = 10\%$. Red lines show the simulation result of the model and the blue lines are the actual CFD data.

The model is also validated for off design actuation. As shown below in Figure 9, the 3x2 ANN-ARX model does an excellent job of simulating the mode amplitudes for an off design actuation case with forcing of $\frac{f-f_o}{f} = 0$ and $\frac{y}{D_{cyl}} = 10\%$.

The adaptive feedback control algorithm in section 2.2.1 was designed and mode $a_{2,1}$ was fed back to the vertical cylinder position. Once the gain aggressiveness (γ) in equation 2.25 was properly conditioned and correspondingly good results were seen with the ANN-ARX closed loop simulation (i.e. reduction of mode $a_{2,1}$) were seen the same control algorithm was plugged into

a CFD simulation. The CFD simulation shows qualitatively accurate results when compared to the ANN-ARX model. Thus proving that the model does capture the close loop dynamics of the cylinder wake flow field.

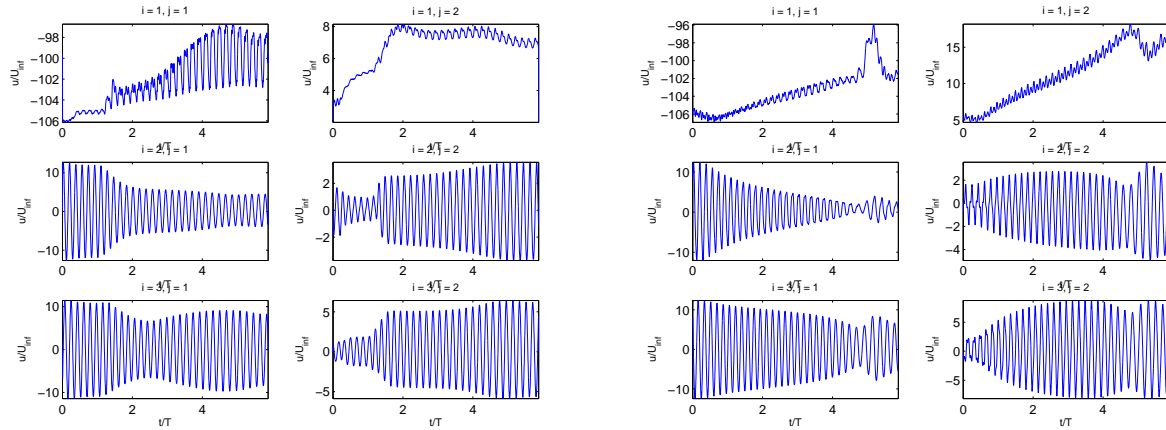


Figure 10: Closed loop simulation of the 3x2 ANN-ARX model(left). CFD closed loop simulation(right). Similar dynamics are shown between each of the models.

The CFD simulation allows for the ability to analyze flow characteristics such as pressures, velocities, densities, etc. Here the surface pressures of the cylinder can be integrated around the surface to give resulting lift forces and more importantly drag force. Figure 11 shows a reduction of drag on the cylinder up to 16%. Thus, proving the control development strategy successful for simple flow fields.

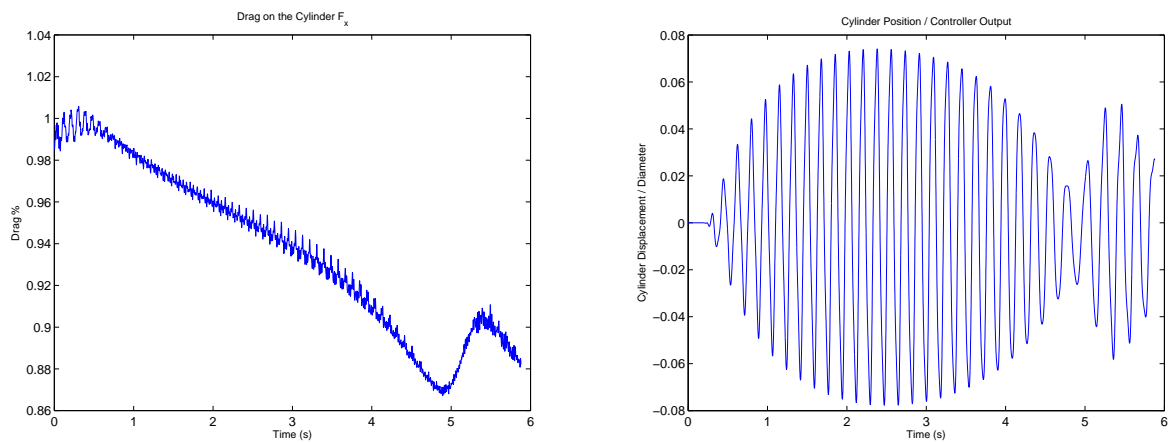


Figure 11: CFD closed loop simulation using direct adaptive control. Drag force reduction (left) and actuation input/cylinder position (right).

5.2 Aero Optics

Aero-optical systems are designed for the transmission of light beams through aerodynamic flow fields. For optical design purposes, the flow has to be considered as a time-varying optical element due to density variations of the fluid in the beam path, which lead to changes in the optical path length (OPL). The correlation between density fluctuations and variations in the gas refractive index, whose integral is the optical path length, is described by the Gladstone-Dale relation, which states a linear relationship where the proportionality constant is the Gladstone-Dale constant McMackin et al. [1997], Jumper and Fitzgerald [2001].

Aero-optical aberrations can be loosely grouped into two categories. The first, associated with the large scales in the flow field, includes boresight (tracking) errors. Some of these errors could be alleviated by current adaptive optical systems because of their relatively large length scales and slow time scales. The second category includes errors such as beam spreading, scintillation and reduction of resolution, contrast, etc., due to the small scale turbulent motion in the flow. Although recently there have been some indications that the large scale motion can also cause errors typically associated with small scales, this classification still seems appropriate. In the past, corrections for these aberrations in aero-optical systems were based on compensation using optical components. This approach led to the development of highly complex adaptive optical systems. While truly impressive results have been achieved for telescopes used in astronomy, which have to correct for aberrations due to the earth's atmosphere, state-of-the-art adaptive optical systems have only met limited success on airborne applications. To a large extent, this is due to the vastly different length and time scales, compared to terrestrial astronomy applications, present on envisioned airborne optical platforms. One of the problems is that all adaptive optical systems rely on mechanically moving some component (usually a mirror surface) to adapt to beam distortions due to the flow field. Current systems are still limited in their bandwidth, frequency, and field-of-vision and are unable to correct for disturbances of all length and time scales. The same limitations apply to wave front sensors, and although new wave front sensors are being developed to analyze distortions in aero-optical applications, they still suffer from limitations that make them only marginally usable in environments comparable to the one in airborne applications Trolinger et al. [2005].

A relatively new approach to understanding and controlling the optical aberrations observed in applications is to look at directly controlling the flow field to minimize the strength of the structures responsible for the optical distortions. If control is possible, and recent research Seidel et al. [2005], Siegel et al. [2005a] has shown initial successes in this research area, the aberrations could be reduced, possibly overcoming a significant hurdle on the way to the implementation of airborne optical systems. In this context, two fundamentally different ideas of flow control are currently being explored. The first is open-loop active flow control (AFC), which introduces small amplitude disturbances at sensitive locations in the flow, which will then be amplified using the flow's inherent instabilities and thus can lead to large global changes in flow behavior. The best known example of this technique is the delay of separation on airfoils at large angles of attack by introducing small disturbances upstream of the separation point that keep the flow attached by energizing the boundary layer. However, even AFC is not able to react dynamically to changing operating conditions. Furthermore, AFC relies on creating disturbances, which in the context of aero-optics applications is detrimental to improving system performance. The problems outlined above led to the development of a second idea for flow control: feedback (closed-loop) flow control. The key components of the feedback system are flow sensors, the state estimator, a controller module and

the actuators. The information obtained from sensors, which observe instantaneous, localized flow quantities, is analyzed in the state estimator. The reduced data is then supplied to the controller module to determine an output signal that is used to drive the actuators. It has been shown that using feedback flow control, it is possible to achieve goals such as the suppression of the von Kármán vortex street Siegel et al. [2005a] that are not achievable using active open loop control. Also, feedback flow control is typically more efficient than active flow control due to its ability to optimize the forcing input to match the current flow state. Furthermore, feedback flow control is tolerant against environmental changes, since it senses the actual, instantaneous flow field rather than operating on assumed states. And finally, because feedback control is used on demand, it does not have a detrimental effect in other flow regimes. These properties make feedback flow control superior to active flow control despite the increased complexity.

For the aero-optical problem, two different approaches for implementing AFC have been investigated to date. The first, developed by Jumper and co-workers [see e.g. Gordeyev et al., 2005], is based on the idea that regularizing the flow will yield a flow field that is more deterministic with respect to its unsteadiness. This is achieved by forcing the flow with a known disturbance signal (frequency, phase, and amplitude). The knowledge of the resulting structure of the flow field, including the (approximate) strength and phase of the large, most optically active structures, simplifies the task of the adaptive optics system, which targets the now known distortions. While this approach has been shown to yield good results, it also strengthens the large structures, which is counterproductive when the goal is to minimize their optical aberrations. The second approach, which was developed by Glezer and co-workers Oljaca and Glezer [1997], Vukasinovic et al. [2004], hinges on the observation that the large, and therefore low frequency, coherent structures in the flow field can be destroyed by high frequency forcing. Although they have shown successful reduction of the large structures and their associated optical distortions, it stands to reason that increasing the energy contained in the small structures is detrimental to the optical performance because it strengthens exactly those structures that provide the high frequency, small scale aberrations that are outside the realm of correction of current adaptive optical systems.

In contrast to the above mentioned open-loop AFC research, feedback flow control was used in this project to control the unsteady structures in the flow field. The underlying assumption is that if the large, coherent structures can be successfully weakened, their aberrations will diminish as well. In addition, when energy is extracted from the large structures, the energy available to create small scales is diminished, delaying the development of turbulence. This notion has been successfully demonstrated for the Kármán vortex street, where successful control of the shedding frequency also yielded an amplitude reduction in higher harmonics Siegel et al. [2003a, 2005a]. It is this combination of effects that holds the promise of successfully controlling the optical aberration due to the flow over the aperture of airborne optical platforms.

As outlined above, systems currently in use suffer from aberrations that are outside the capabilities of state-of-the-art adaptive optics systems. To alleviate the tasks to be borne by the adaptive optical system has the potential to provide a highly sought after functionality. The renewed interest in these systems, with much more stringent requirements for accuracy, requires novel methods to reduce the detrimental effect of the flow over the aperture.

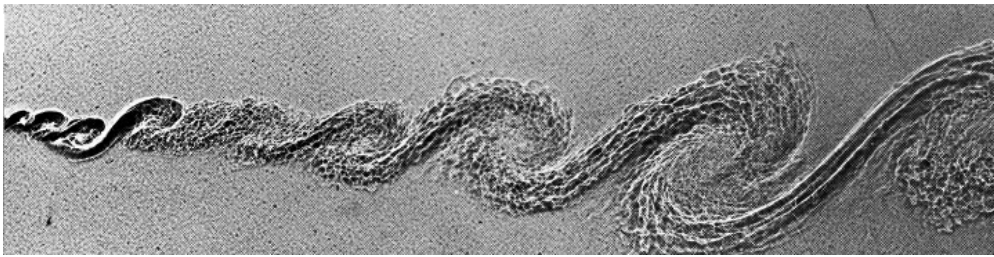


Figure 12: Turbulent shear layer Van Dyke [1982].

5.2.1 Technical approach

The core technologies for this aero-servo-optics project, aimed at reducing optical aberrations in airborne platforms, were derived from a combination of the fluid dynamics, controls, and optics research areas, with a strong emphasis on fluid dynamics and controls. The optical performance of the proposed aerodynamic control system was judged using the well-known correlation between the fluid density and index-of-refraction fields in gases. The underlying assumption was that as long as reliable data of the density field is available (through simulations or experiments), a good representation of the optical properties should be achievable.

From a fluid dynamics point of view, shear layers develop large, coherent structures due to their inherent inviscid instability. As shown in Figure 12, there are several stages in this development. First, large, laminar, S-shaped structures are generated behind a splitter plate. After the initial growth of these structures, smaller structures develop due to further instability mechanisms, eventually leading to small scale turbulence. However, as shown in the figure, even when the flow is turbulent, the large coherent structures persist. It is these structures that are responsible for the large boresight errors in aero-optical applications. However, because of their large size and relatively low frequency, an adaptive optical system can correct for their effect if their amplitude and phase are known. Another important aspect to note in Figure 12 is that the turbulent motion develops as a consequence of the primary flow instability that creates the S-shaped shear layer structures. This is in accordance with observations of the energy cascading from large to small scales Pope [2000].

For the aero-servo-optics project, this energy cascade is of crucial importance: If feedback flow control is able to reduce the strength of the primary shear layer structures, it follows that there is less energy in these disturbances and therefore less energy is available to generate small scale turbulent structures, resulting in significantly reduced optical aberrations on all scales. An effect similar to the one outlined above, namely the reduction of the amplitude of high frequency disturbances by controlling a lower frequency, has been observed in low Reynolds number wake flows Cohen et al. [2003a].

There were certain aspects of the investigations that lent themselves to investigations using simulations, while other aspects were explored more easily and efficiently in the experiment. For example, only small portions of the flow can be measured simultaneously in the experiment since the sensing options are limited. Thus, meaningful sensor locations can be derived much more easily from simulation results since the entire flow field data with all its variables is available. However, in order to vary flow and actuation parameters, a new simulation needs to be performed for each set of parameters, with the associated cost and time requirements. In contrast, once the

experimental hardware is in place, flow and actuation parameters can be varied easily and quickly. Thus this type of investigation is best performed using experiments. In summary, by using both experiment and computation in parallel, the fastest possible progress was achieved.

To provide an overview of the feedback flow control design cycle used in this research project, Figure 1 shows the main building blocks in the process. The development started with building a database of flow states based on CFD simulation results. First, the natural (i.e. without any control input) flow field was simulated. Then, a number of simulations were performed where periodic blowing and suction was used to introduce disturbances at a given frequency and amplitude into the flow (see Section 5.2.2.4). The results of all these simulations were analyzed using Proper Orthogonal Decomposition (POD), which resulted in POD spatial modes as well as the POD time coefficients for each time step of all simulations.

These POD modes and time coefficients were then used for the development of a reduced order model (ROM). In the present effort, a wavenet ARX topology was chosen (see Section 4.2.2.1). Once the model performance was validated against the original CFD data, state-of-the-art feedback controller design tools were used to develop a controller. Iterative testing (iteration loop “1” in Figure 1) lead to a controller design that achieved the predefined control goal of minimizing the optical distortion for a given aperture.

In addition, the POD spatial modes were scrutinized for flow state estimation purposes. Sensors placement studies, which were used to determine the number and locations of flow sensors, were performed using the computed flow quantities on the wall behind the backward facing step (see Section 4.2.4.2). With the sensors chosen, a flow state estimator was developed. This estimator determined the *global flow state* based on the sensor readings, i.e. it established field data from only the sensor information.

At this stage, the flow state estimator and the controller were introduced into the CFD simulations and feedback controlled simulations were performed. The results of this simulation were scrutinized to investigate the effect of the control input on the flow field, as well as their effect on the overall figure of merit, the OPD. As indicated in Figure 1, multiple iteration paths were open at this point. Path “2” in Figure 1 could be taken if the results indicated that the controller, designed using the wavenet model, is not performing well. It could also be possible that the findings indicate problems with the wavenet itself, which would be remedied using iteration path “3”. Finally, the research design is flexible enough to also allow inclusion of feedback controlled data into the POD database to improve the fidelity of both model and controller development. All steps outlined above will be described in detail in this report.

5.2.1.1 Basic flow parameters Several parameters had to be considered to arrive at flow conditions that on the one hand result in large enough (i.e. measurable) density changes, but that, on the other hand, do not result in vortex shedding frequencies that were too high to be measured successfully. In addition, the slower the flow, the easier it is to implement a feedback control system. These considerations resulted in the following key experimental parameters:

- Mach number $Ma = 0.3$ at the inflow
- Step height $H = 0.15\text{m}$
- Free stream velocity at step $U_\infty = 140\text{m/s}$

5.2.1.2 Optical definitions The optical properties of the fluid forming the shear layer behind the backward facing step were evaluated based on the Gladstone Dale relation

$$n(x, y, z, t) = 1 + k_{GD}\rho(x, y, z, t), \quad (57)$$

where n is the fluid's index of refraction, k_{GD} is the Gladstone-Dale constant, $k_{GD} = 2.289 \times 10^{-4} \text{m}^3/\text{kg}$, and ρ is the fluid density. The optical path length (OPL) can be obtained by integrating the index of refraction along the beam path, L ,

$$\text{OPL}(x, y, z, t) = \int_0^L n(x, y, z, t) dl = L + k_{GD} \int_0^L \rho(x, y, z, t) dl. \quad (58)$$

Since the differences in OPL over a given aperture are typically on the order of the wave length of the beam, it is common to express the wave front distortion as the optical path difference (OPD), which is defined as the local, instantaneous OPD minus the spatial mean over the aperture. Assuming the beam propagates in the y -direction, this can be expressed as

$$\text{OPD}(x, z, t; y) = \text{OPL}(x, z, t; y) - \overline{\text{OPL}(x, z, t; y)}^{xz}. \quad (59)$$

These equations were used when analyzing the CFD results because the density field $\rho(x, y, z, t)$ is computed directly from the governing equations.

5.2.2 Numerical Simulation

The exact geometry for the simulations of a free shear layer was developed in conjunction with the design of the experiment. Comparisons to experimental data performed at USAFA aeronautics laboratory of the unforced flow field data were performed to validate the accuracy of the simulations and to judge the necessary grid resolution to resolve the relevant flow features. In particular, the optical path difference (OPD) was used as the main optical figure-of-merit. It should be noted that once a time accurate, spatial density distribution is available from the computations, calculating the index of refraction field and the resulting OPD is possible with a small computational effort compared to the CFD simulations. During the course of this study, Mani et al. [2008] published an article outlining the resolution requirements determined by their aero-optical simulations. They concluded that the resolution requirements for an aero-optic simulation match the ones for a well resolved LES simulation.

To build a database of flow states that would be used to define the reduced order model for the flow field, unforced simulations were performed first. In a second step, open loop active flow control (AFC), which in the simulations was implemented using an externally controlled blowing/suction boundary condition (see below), was studied and the data was added to the development cycle of the database. These forcing cases were particularly valuable for describing the transient flow features present during the initial development of the open loop forced shear layer as well as the vortex pairing that occurred when forcing was initiated. The results from the simulations provided a comprehensive database of the free shear layer, which was used to develop feedback control strategies as well as to compare the effectiveness of feedback control applied to the aero-optics problem.

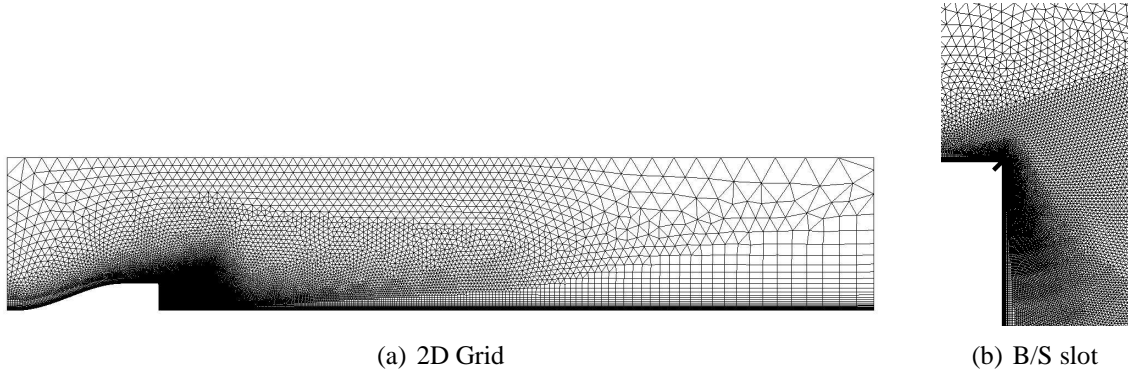


Figure 13: a) Two-dimensional CFD grid. b) Grid at the step showing the blowing/suction slot.

5.2.2.1 Grid generation The experimental ramp geometry was used in the simulations. The grids for the simulations were generated using the SimCenter software developed at Mississippi State University Marcum and Weatherill [1995]. Since the geometry is essentially two-dimensional, a planar grid was generated first and then this grid was extruded in the spanwise direction. The step height was $H = 0.15\text{m}$, and the ramp length $L_R = 0.85\text{m}$. To ensure that no disturbances reach the outflow boundary, the domain length was $L_x = 4\text{m}$ downstream of the step. The domain height matched the experimental setup in the USAFA wind tunnel, $L_y = 0.85\text{m}$.

The main difference to the experimental geometry was that the forcing chamber (see Figure 19) was not included in the simulations. Instead, only a short section of the slot ($b = 1\text{mm}$) was modeled and a blowing and suction boundary condition was applied at the base of the slot. Figure 13 shows the final two-dimensional grid. A zoomed view of the step with the blowing/suction slot is given in Figure 13. The grid spacing at the step was defined to be $\Delta x = 0.1\text{mm}$. This grid contains approximately 58,000 nodes and 90,000 elements. Grid clustering was used on the bottom wall and in the region of interest in the free shear layer. In order to resolve the blowing and suction slot geometry, the grid also had to be refined near the step edge. The boundary layer grid spacing was chosen such that the final y^+ value at the step was $y^+ \simeq 1$.

For the three-dimensional simulations, this grid was extruded in the spanwise direction. The spanwise step size was chosen as $\Delta z = 1\text{mm}$. Solutions at various domain widths ($L_z/H = 1, 2, 3, 4$) were computed to ensure that the pertinent shear layer dynamics were captured in the simulations. Figure 14 shows the geometry for the case $L_z/H = 2$.

In addition to the grid for the CFD simulations, a grid for the beam propagation was developed. The beam domain size was chosen as $0 < x/H < 3$, $-1 < y/H < 0.5$, and spanned the whole spanwise domain, which represents a sufficiently large domain to investigate various optical apertures while being able to maintain reasonable resolution. $46 \times 81 \times 41$ points were used in the x-, y-, and z-directions, respectively. The grid was designed as a structured grid with one grid direction aligned with the predominant beam direction. This approach facilitated the computation of the OPL and OPD (see Equations 58 and 59) since the path integral was along grid lines. For the interpolation of the CFD data onto the beam grid, the 'tap' capabilities in COBALT were used. Taps were initially designed as measurement locations, but for the current research, using taps to extract the flow field on the beam grid ensured that the numerical methods for integration of the Navier-Stokes equations and interpolation were consistent.

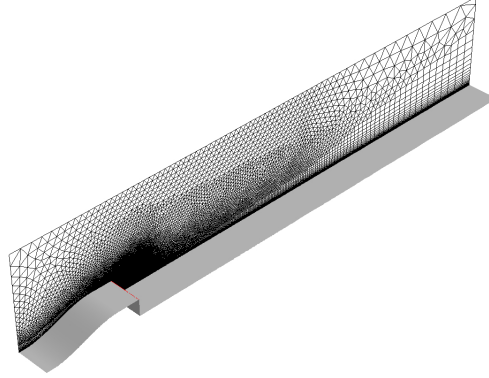


Figure 14: Three dimensional domain with CFD grid, $L_z/H = 2$.

5.2.2.2 Results Figure ?? shows the comparison of the mean flow u-velocity profiles at $x/H = 0, 0.5, 1, 2, 3, 4$ obtained from experiments (symbols) and simulations (lines). The separating boundary layer had a thickness of $\delta_{99} \simeq 8\text{mm}$, which for a fully turbulent boundary layer corresponds to $Re_\theta \simeq 8500$. As the shear layer develops, at downstream positions $x/H < 2$, the shear layer in the simulations is not spreading as quickly as measured in the experiments. Further downstream at $x/H = 3$ the profiles are in very good agreement and at $x/H = 4$ the simulation results show a slightly larger shear layer thickness. This increased spreading rate in the simulation data was attributed to the behavior of the DES turbulence model as the separating flow transitions from a RANS based boundary layer calculation to a Large Eddy Simulation. The initial lack of structures in the flow led to reduced shear layer growth. As the structures developed, the growth rate matched the experimental and theoretical results well, but further downstream, the grid resolution is insufficient to maintain the coherent structures in the flow and numerical diffusion results in an increased spreading rate.

Instantaneous results of the simulations are shown in Figure 15. In Figure 15a, the flow structures are visualized using an iso-surface of the Q vortex identification criterion Jeong and Hussain [1995] colored by pressure. At this instant, the shear layer (Kelvin-Helmholtz) vortices are starting to form approximately one step height downstream of the separation point, with increased spanwise coherence one wavelength further downstream. The instantaneous isosurface of density is shown in Figure 15b. Comparing the Q-vortex structures with the density isosurface shows that there is a very strong correlation.

Furthermore, it is interesting to note that the density isosurface shows only the large scale structures while suppressing the smaller scales at the step as well as in the recirculation region below the shear layer. This is due to the deeper “pressure well”, and the concomitant drop in density, inside the largest structures. For feedback flow control that targets the coherent motion in the shear layer, this behavior of the density field is highly desirable because density behaves like a filter and density isosurfaces identify the flow structures of interest. In addition, since the optical path length is a linear function of density, density is in fact the quantity of interest for the aero-optics problem. This is shown in Figure 16, where the flow structures, identified using the Q-criterion Jeong and Hussain [1995], are shown in grey and the OPD is plotted in color at the top of the beam grid. Comparing the OPD results and the density isosurface plotted in Figure 15 shows a strong

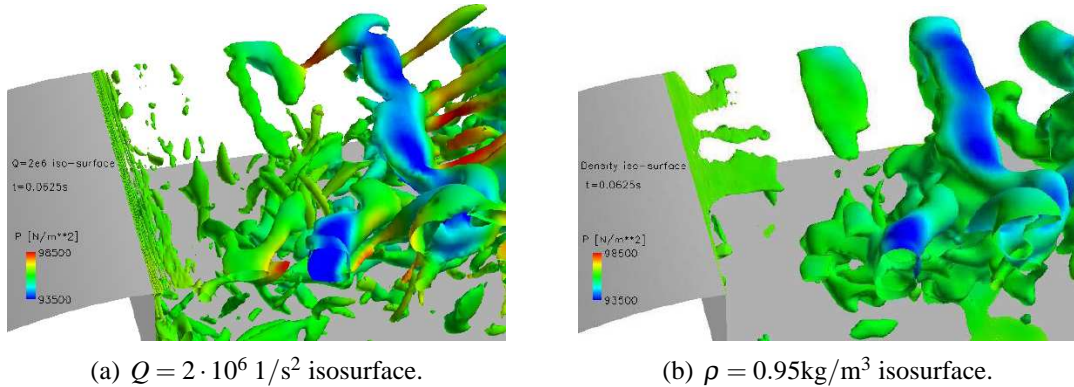


Figure 15: Instantaneous representation of the structures in the flow field. Iso surfaces colored by pressure.

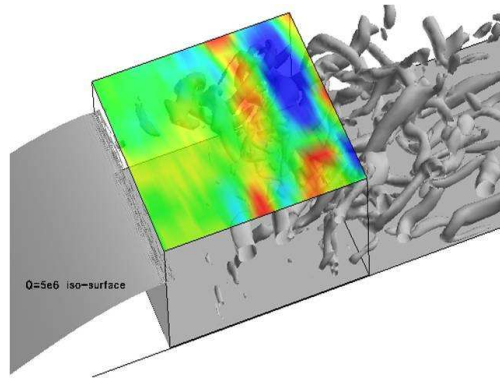


Figure 16: Instantaneous flow structures visualized using an isosurface $Q = 5 \cdot 10^5 \text{ 1/s}^2$ and OPD (color).

correlation between the “valleys” in the wave front (negative values of OPD shown in blue) and the location of the flow structures. The initial vortex shedding frequency for the shear layer can be estimated from theory based on $St = F\theta/U_\infty = 0.012$ Hasan [1992] to be $F_n \simeq 2000\text{Hz}$. Using probes at $y/H = 0$ and various streamwise positions, the frequencies with the highest amplitudes ranged around $F \simeq 400\text{Hz}$ (Figure 17), indicating that vortex pairings had occurred upstream of the probe locations [see Seidel et al., 2009, for more details]. While the total simulation time was too short for a detailed spectral analysis, the results provided a good indication of the frequency of the naturally occurring structures. The results were also in good agreement with the results obtained from the experiments. Because the extent in the streamwise direction spanned by the density probes was commensurate with the area of interest for optical performance, this frequency provided an approximate target frequency to investigate the effect of open loop forcing on the optically relevant shear layer structures. To further analyze the flow field and the structures in the shear layer, the simulation data was reduced using Proper Orthogonal Decomposition Sirovich [1987], Berkooz et al. [1993], Holmes et al. [1996]. The u-velocity, v-velocity, and density were analyzed to examine which of these quantities provided a meaningful representation of the flow structures with a focus on the coherent structures in the shear layer. Figure 18 shows the first six spatial modes (plotted in pairs to show the traveling vortex nature of the shear layer structures) and their corresponding

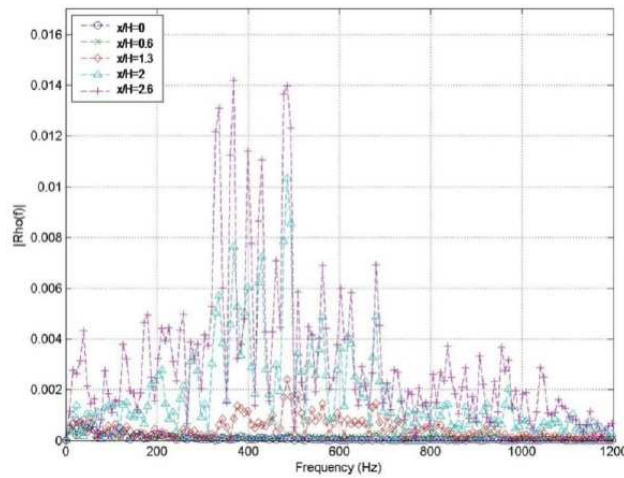


Figure 17: Density spectra between $x/H = 0$ and $x/H = 2.6$. Unforced.

time coefficients for the full length of time available in the data set. Figure 18a shows that the u-velocity POD modes do not have any discernable spatial structure, which is also reflected in the lack of a dominant frequency in the time coefficients (Figure 18b). In contrast, the first two pairs of POD modes of the v-velocity (Figure 18c and d) exhibit a distinct, highly coherent structure that is indicative of traveling waves. The periodic character of the time coefficients corroborates that these POD modes capture the vortex street in the shear layer. The same holds for the density POD modes (Figure 18e and f) that identify the shear layer structures and their spanwise distortions. It is interesting to note that the POD of both the v-velocity and density show the strongest peaks in the shear layer while the smaller scales in the recirculation zone below are suppressed; in contrast, the u-velocity POD modes include these structures. Furthermore, the dominant mode pairs of both the v-velocity and density, modes 1-2 and 3-4, show the same frequency content but are not periodic, corroborating the fact that the spectral peak around the dominant frequency is very broad in the natural flow. Another important point to note is the strong spanwise coherence of modes 1-2 of both the v-velocity and density. This indicates that the dominant structures, as measured by the magnitude of the singular values obtained from the POD procedure (not shown), are indeed spanwise “rollers”, even in the unforced, three-dimensional flow. Forcing, as described in the next section, only increases this spanwise coherence.

Table 2: Summary of computed forcing cases.

	400Hz	600Hz	800Hz	1000Hz
$A/U_\infty = 0.3$	x	x	x	x
$A/U_\infty = 0.2$	x	x	x	x
$A/U_\infty = 0.1$	x	x	x	x
$A/U_\infty = 0.05$	x	x	x	x
$A/U_\infty = 0.01$	x	x	x	x

While this POD analysis was not exhaustive (other quantities, e.g. vorticity, could be analyzed), it showed that either the v -velocity or the density are well suited for developing a reduced order model for control purposes for this research program. From an aero-optics perspective, the density is clearly the best quantity for model and feedback controller development due to its direct influence on the optical properties of the flow.

5.2.2.3 Actuation Since the forcing chamber was not part of the backward facing step flow geometry, it was modeled in a separate simulation to verify that the slot exit velocity was uniform in the spanwise direction. The geometry model is shown in Figure 19a. The geometry included a section of the backward facing step and extended approximately three step heights in the upstream and downstream directions and to three step heights above the slot to ensure that the boundary conditions do not influence the exhaust velocity distribution. In Figure 19a, the red circles indicate the speaker exits. When the speakers are driven by a single frequency, periodic blowing and suction results at the slot exit. The peak blowing stroke is shown in Figure 19b, where the color represents the wall pressure in the forcing duct and the velocity is shown by arrows at the forcing slot exit. The results indicate a slight spanwise pressure variation ($\Delta p/p \simeq 1\%$) from the center of the chamber to its spanwise edges. The exit velocity is shown to be essentially uniform (the variations seen in the figure are due to vectors in the slot boundary layer).

5.2.2.4 Open loop forcing Numerous open-loop forced simulations were performed to provide data for the development of reduced order models for feedback flow control (see Section 5.2.3). These open-loop data have to span the range in the amplitude-frequency parameter space that will be utilized by the controller. To provide these data sets, simulations with different forcing parameters have been performed and analyzed.

From the unforced data it was determined that the vortical structures in the shear layers naturally occur at $F_n \simeq 400\text{Hz}$ at $x/H = 2$. This frequency formed the basis for a study where the blowing and suction actuation was used in a frequency range from $F_f = 400\text{Hz}$ to $F_f = 1000\text{Hz}$ and an amplitude ranging between $A/U_\infty = 0.01$ and $A/U_\infty = 0.3$, resulting in the time dependent blowing and suction velocity $u_f(t) = A \sin(2\pi ft)$. A table of all the computed cases is given in Table 2; representative results from this part of the investigation are shown in this section.

When forcing is applied at $F_f = 400\text{Hz}$, $A/U_\infty = 0.1$ (Figure 20), the density spectra taken at the five downstream locations $x/H = 0, 0.6, 1.3, 2, 2.6$ show that the flow initially amplifies the forcing frequency through $x/H = 2$. At $x/H = 2.6$, the amplitude starts to decay. In addition, the first harmonic at $F = 800\text{Hz}$ is amplified between $x/H = 1.3$ and $x/H = 2$. No subharmonic frequency is discernable in the data. When forcing at $F_f = 600\text{Hz}$, $A/U_\infty = 0.1$ (Figure 21), the

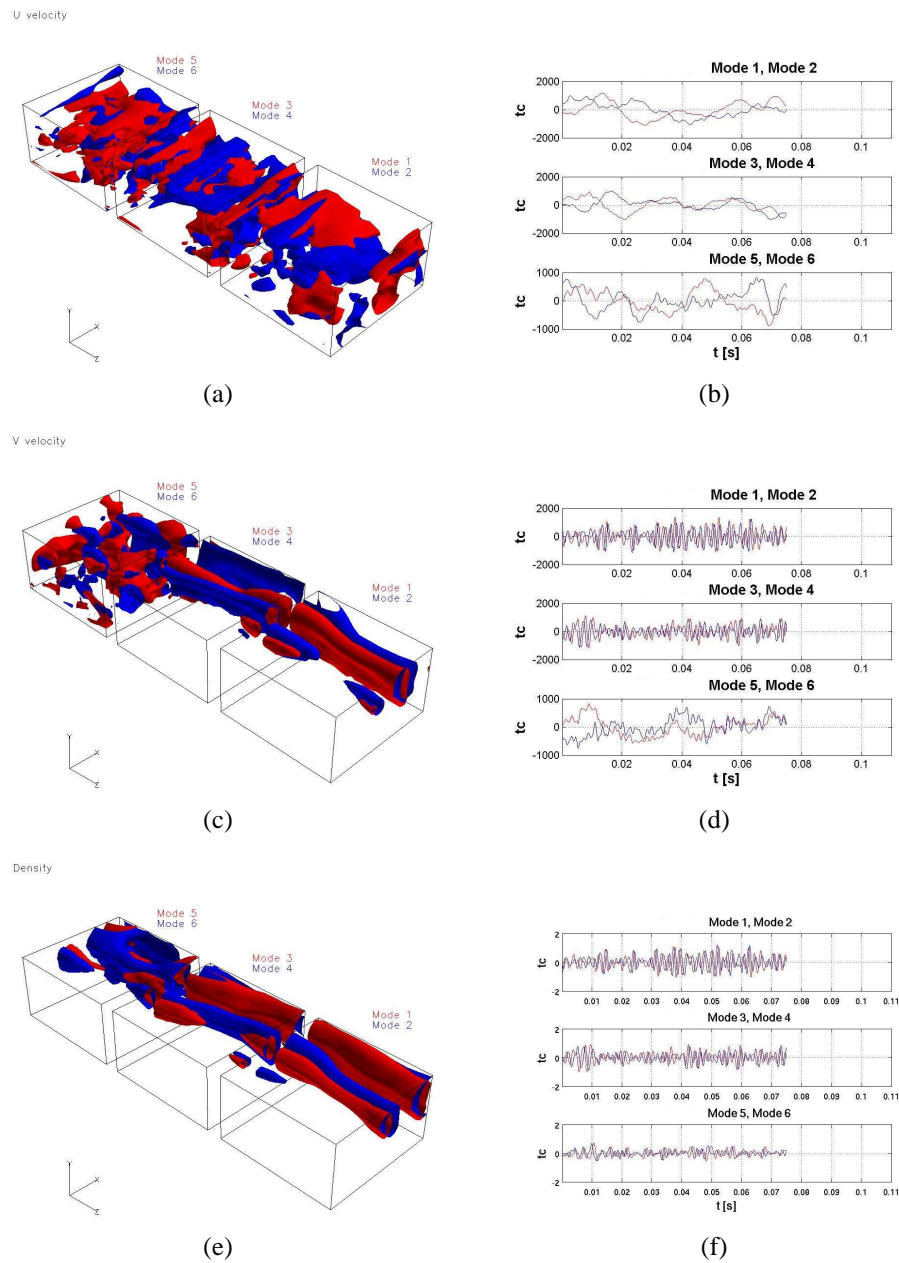


Figure 18: POD modes and time coefficients for a),b) u-velocity, c),d) v-velocity, e),f) density. Unforced case.

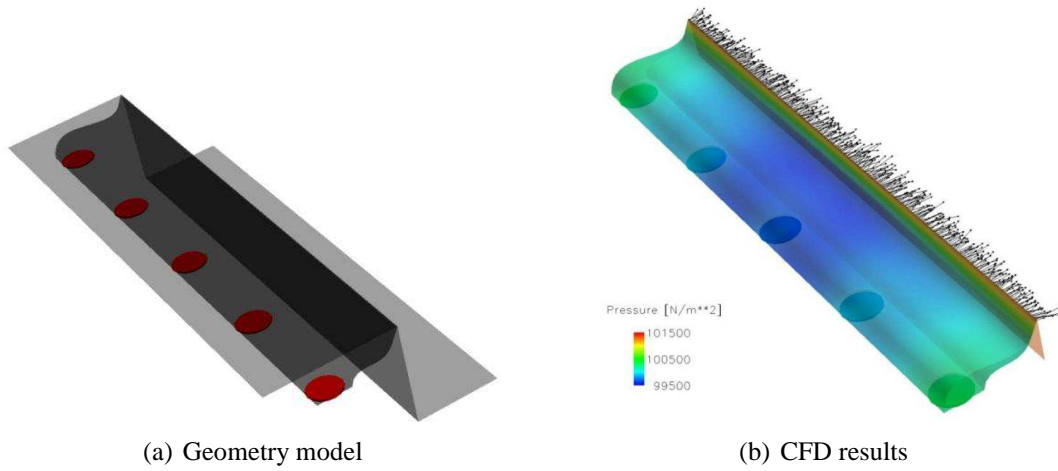


Figure 19: Blowing and suction slot analysis. Pressure distribution in the blowing suction duct (color) and velocity vectors at the slot exit.

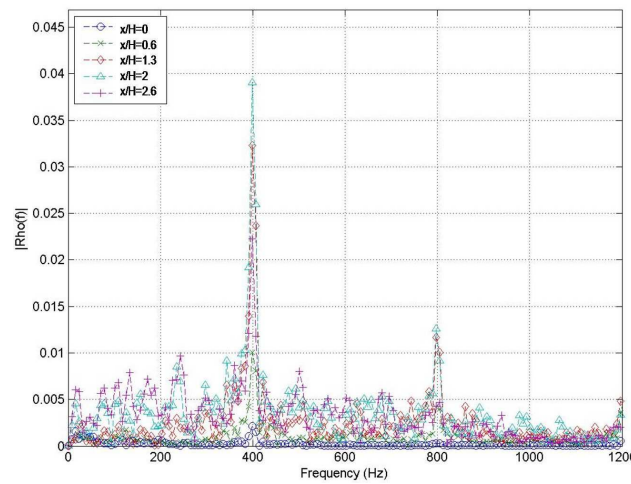


Figure 20: Density spectra between $x/H = 0$ and $x/H = 2.6$, $F = 400\text{Hz}$, $A/U_\infty = 0.1$.

fundamental is strongly amplified between $x/H = 0$ and $x/H = 0.6$ and decays downstream. In addition, the first subharmonic frequency $F_s = 300\text{Hz}$ is amplified as well and decays very slowly downstream of $x/H = 1.3$. Finally, forcing at $F_f = 800\text{Hz}$, $A/U_\infty = 0.1$ (Figure 22) shows the largest amplitude response close to the slot of the three forcing cases and a rapid growth of the fundamental. Downstream of $x/H = 0.6$ it decays and the subharmonic starts to develop, indicating vortex pairing in this region.

Performing POD on the density results in the modes shown in Figure 23 for a forcing frequency of $f_f = 400\text{Hz}$. In the figure, POD mode isosurfaces $\hat{p} = 0.005\text{kg/m}^3$ are shown. The dominant modes 1 and 2 show the developing shear layer vortex street. Modes 3 and 4, which develop further downstream, are representative of the spanwise distortion of the main shear layer structures. The time coefficients, Figure 23c, clearly show the forcing frequency in modes 1 and 2.

For forcing at $F_f = 600\text{Hz}$, the POD modes of density are shown in Figure 24 (the same isosurface level as in Figure 23 is plotted). The development of the POD modes is similar to

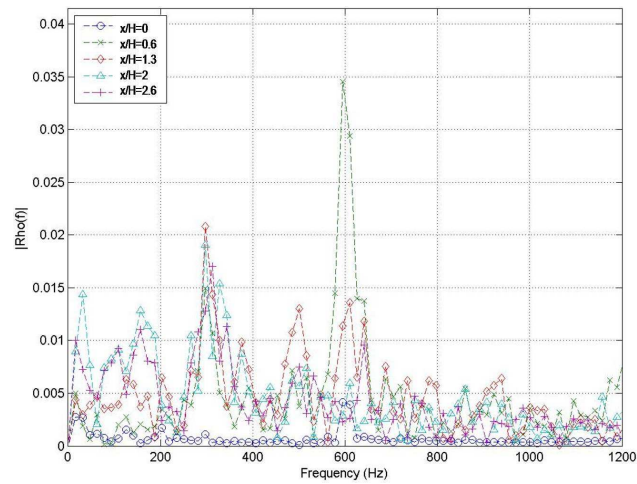


Figure 21: Density spectra between $x/H = 0$ and $x/H = 2.6$, $F = 600\text{Hz}$, $A/U_\infty = 0.1$.

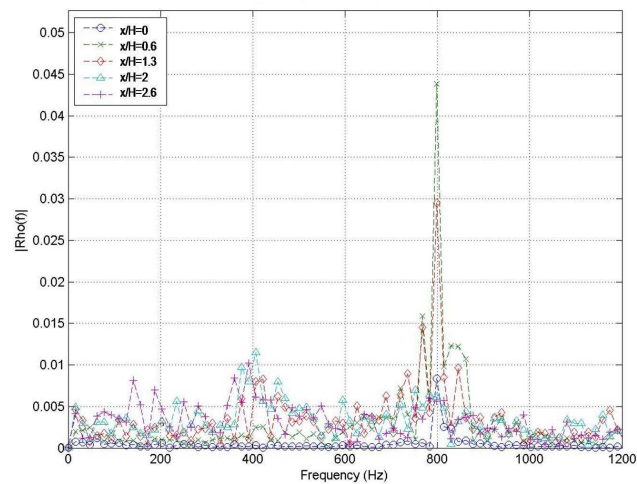


Figure 22: Density spectra between $x/H = 0$ and $x/H = 2.6$, $F = 800\text{Hz}$, $A/U_\infty = 0.1$.

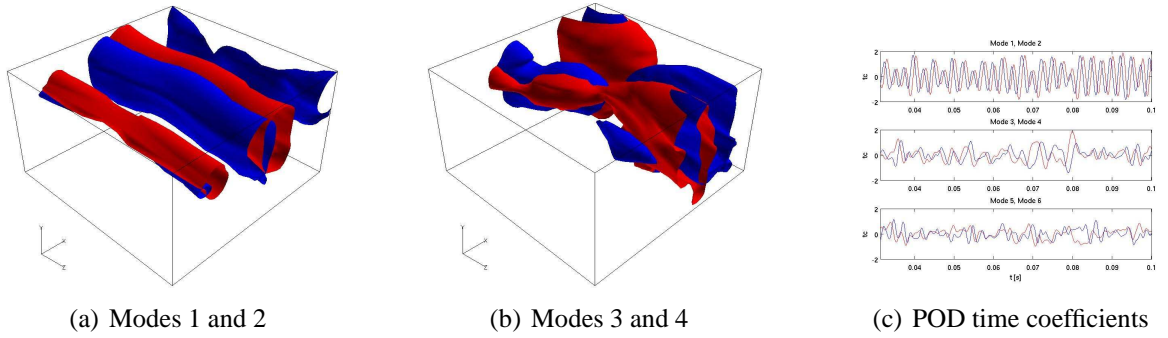


Figure 23: POD density modes and time coefficients, $F = 400\text{Hz}$, $A/U_\infty = 0.1$.

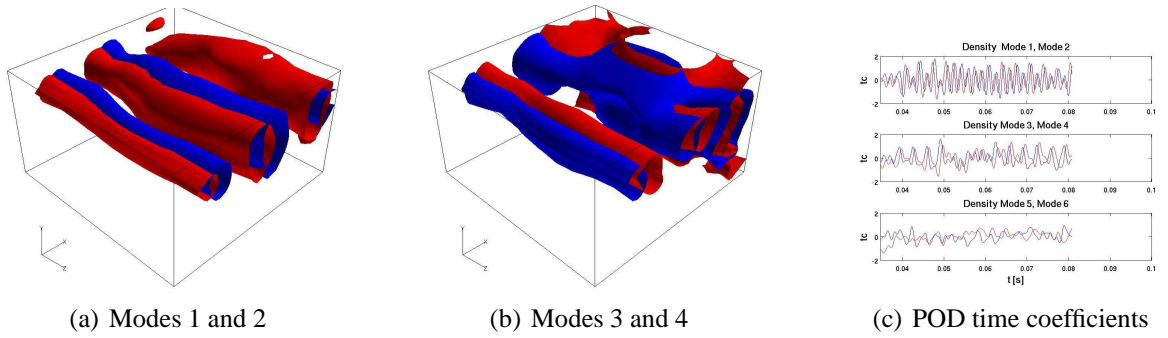


Figure 24: POD density modes and time coefficients, $F = 600\text{Hz}$, $A/U_\infty = 0.1$.

the $F_f = 400\text{Hz}$ case, although the emergence of the modes was shifted upstream due to the higher frequency, in accordance with theory Ho and Huerre [1984]. The time coefficients exhibit the same behavior as in the previous case, but the subharmonic character of modes 3 and 4 is more pronounced. Finally, for $F_f = 800\text{Hz}$, the POD results are shown in Figure 25. The figure shows that the vortical structures develop a very short distance downstream of the step (located at the inflow boundary of the box shown in the figures), but the growth saturates quickly and the highly coherent structures begin to show three-dimensional distortions (as indicated by POD modes 3 and 4) further downstream. The time coefficients show that modes 1 and 2 are the most periodic of all investigated forcing cases and that modes 3 and 4 oscillate at the first subharmonic frequency. In all cases, as pointed out for the unforced case, the density POD modes represent only the structures in the shear layer and not the smaller scale motion in the recirculation region, which is beneficial for the development of a reduced order model of this flow.

The optical properties of the flow field were analyzed using the beam grid described above. As for the unforced case, the density field on this grid was integrated from the wall through the shear layer and the effect of open loop, periodic forcing was assessed. Figure 26 shows instantaneous plots of the flow structures and the OPD. There is a strong correlation between the structures in the shear layer and the OPD results, as was observed for the unforced flow. However, when forcing is introduced, the structures in the flow exhibit increased spanwise coherence due to the spanwise uniform forcing.

The three-dimensional simulations described above all showed that the dominant dynamics in the shear layer behind the backward facing step are essentially two-dimensional, at least in

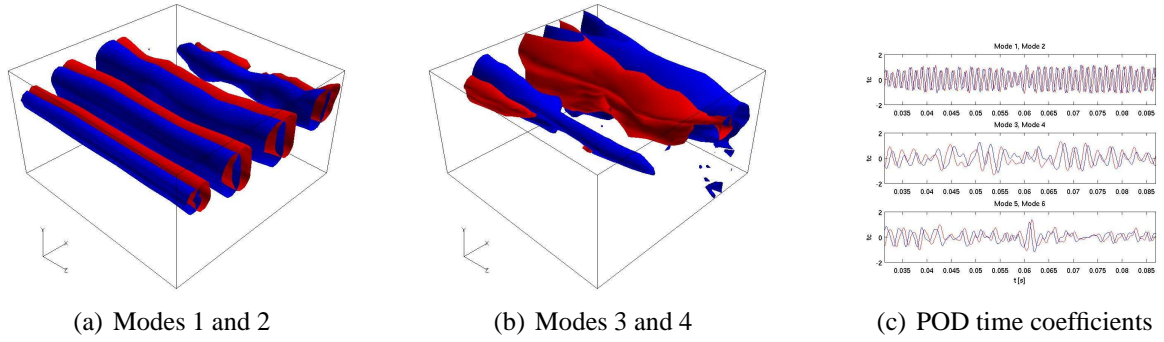


Figure 25: POD density modes and time coefficients, $F = 800\text{Hz}$, $A/U_\infty = 0.1$.

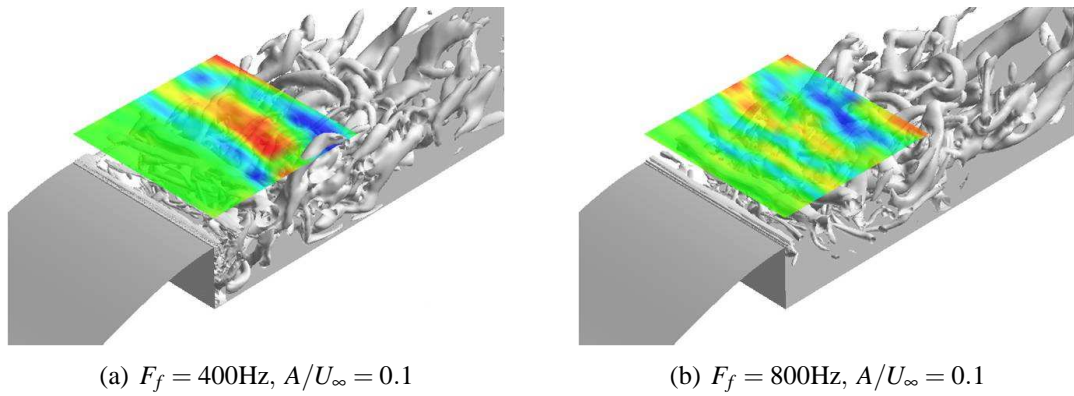


Figure 26: Instantaneous isosurface of flow structures and associated OPD for various forcing conditions.

the domain investigated in this research project. Especially the POD analyses showed this two-dimensionality in the first pair of modes, which are representative of the most dominant structures in the flow, the Kelvin-Helmholtz vortices. While three-dimensional effects cannot be discarded for a complete description or reconstruction of the flow field from the POD data, it is posited that for the development of feedback flow control strategies, a two-dimensional representation of the flow captures the relevant physical processes. This allowed for drastically reduced simulation times and more efficient use of the computational time available to the project.

To develop the POD mode database for reduced order modeling and controller design, therefore, the simulations above were repeated for the two-dimensional grid. The results obtained from these simulations were comparable to the results described above. Most importantly, the natural shedding frequency matched the three-dimensional results. This is a good indicator that the instability mechanism that results in the Kelvin-Helmholtz vortices was not negatively affected by the reduction to two dimensions. A comparison for the forced simulations showed a slightly higher amplitude of the fluctuations for the two-dimensional simulations. This was expected since these simulations could be viewed as ideal in the sense that they provide perfect spanwise coherence. Another way to think of these results is that the structures are infinitely long in the spanwise direction. The increased coherence of the structures did not affect the initial development of the shear layer targeted with feedback control. However, further downstream, where the structures start to develop spanwise distortions in the three-dimensional simulations, the two-dimensional simulations overpredicted the strength of the structures.

The two-dimensional simulations were performed on the grid shown in Figure 13. Simulation results for the unforced or open-loop cases will not be shown here; results for the validation of the feedback control strategy are presented in Section 5.3.2.2.

5.2.3 Reduced Order Modeling

5.2.3.1 Numerical Reduction The procedure in section 4.2.2.1 was precisely followed and the following results were detected.

The quantity of greatest concern in this project is the OPD, which, as shown in Equations 57-59, is linearly dependent on the fluid density $\rho(\mathbf{x}, t)$. Substituting the POD decomposition of ρ into Equation 57 yields

$$n = 1 + K_{GD} \sum_{i=1}^{m'} a_i(t) \phi_i(\mathbf{x}) \quad (60)$$

and the OPL (Equation 58) can be calculated as

$$OPL = \int_L n(s) ds = \int_L \left[1 + K_{GD} \sum_{i=1}^{m'} a_i(t) \phi_i(\mathbf{x}) \right] ds \quad (61)$$

or

$$OPL = L + K_{GD} \sum_{i=1}^{m'} a_i(t) \int_L \phi_i(\mathbf{x}) ds. \quad (62)$$

The OPD is then computed from Equation 59 such that

$$OPD = \left[L + K_{GD} \sum_{i=1}^{m'} a_i(t) \int_L \phi_i(\mathbf{x}) ds \right] - \overline{\left[L + K_{GD} \sum_{i=1}^{m'} a_i(t) \int_L \phi_i(\mathbf{x}) ds \right]}. \quad (63)$$

Simplifying this expression gives

$$OPD(\mathbf{x}, t) = K_{GD} \sum_{i=1}^{m'} a_i(t) \left[\int_L \left[\phi_i(\mathbf{x}) - \overline{\phi_i(\mathbf{x})} \right] ds \right] \quad (64)$$

where the OPD spatial modes are $\int_L \left(\phi_i(\mathbf{x}) - \overline{\phi_i(\mathbf{x})} \right) ds$.

Comparing this result with Equation 17 shows that the OPD POD modes can directly be derived from the density POD modes by using the definition of the OPD. This is important because the density is readily available from the CFD simulations. Furthermore, because of this direct relationship, the minimization of the time coefficients of the density POD modes will be regarded as the main control goal to regulate the flow to reduce OPD fluctuations using feedback flow control.

5.2.3.2 POD Parameter Study A large parameter study was carried out to determine an appropriate means for numeric decomposition. The parameters consisted of POD vs. DPOD, spatial domain size, and also the data sets to be used in the decomposition. The spatial domains were defined as

$$\begin{aligned} X1 &\equiv 0 \leq \frac{x}{H} \leq 4 & -1 \leq \frac{y}{H} \leq 1 \\ X2 &\equiv 0 \leq \frac{x}{H} \leq 2\frac{1}{3} & -\frac{1}{3} \leq \frac{y}{H} \leq \frac{1}{3} \\ X3 &\equiv 1\frac{1}{3} \leq \frac{x}{H} \leq 2\frac{2}{3} & -\frac{1}{3} \leq \frac{y}{H} \leq \frac{1}{3} \end{aligned} \quad (65)$$

The three spatial domains (X1, X2, X3) adequately contain the optical aperture of interest, whose center is located at $x/H = 2$. The domain size study helped to determine if limiting the amount of information in the POD kernel has a detrimental effect on the model.

A typical forcing input for a given frequency and amplitude is shown in Figure 27. The forcing begins from the fully developed unforced flow computed for $t < 0$. The first five cycles of forcing are defined as the opening transient in which the flow starts to react to the forcing signal. The flow then locks in to the forcing signal for the remainder of the duration of the forcing. When the forcing is turned off, the flow undergoes an ending transient in which the flow shifts back into its natural state. The data sets used for the POD/DPOD study were

$$\begin{aligned} D1 &\equiv \textit{Forcing} \\ D2 &\equiv \textit{Forcing} + \textit{Unforced} \\ D3 &\equiv \textit{Forcing} + \textit{Unforced} + \textit{Starting/EndingTransients}. \end{aligned} \quad (66)$$

The resulting POD/DPOD model was then validated using the case $F_f = 600\text{Hz}$, $A/U_\infty = 0.05$, which had been removed from the training data sets for model validation purposes. To quantify the reconstruction error, the root mean squared error of the local and instantaneous density field was computed as

$$\epsilon_{rms}(t) = \left[\overline{(\rho((Xi), t) - \hat{\rho}((Xi), t))^2} \right]^{1/2}, \quad (67)$$

or, expressed as a percentage of the mean density,

$$\epsilon(t) = \frac{\epsilon_{rms}(t)}{\bar{\rho}((Xi), t)}. \quad (68)$$

The parameters for the dataset study are shown in Table 3.

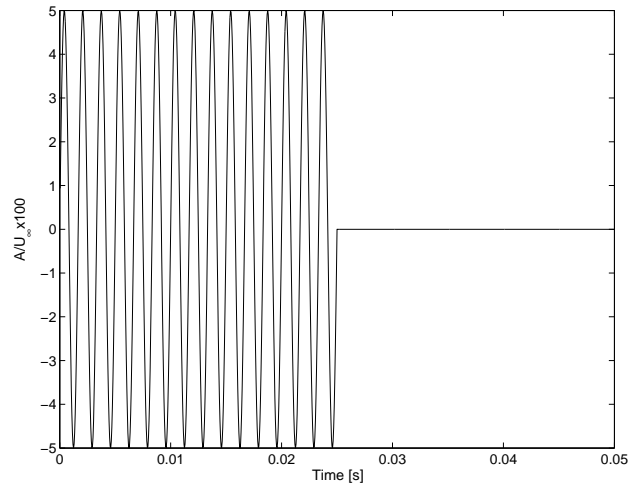


Figure 27: Typical forcing input, $u(t|F,A)$, for an open loop simulation. Case will undergo a total of four defined stages. Starting transient ($0 \leq t \leq 0.01$), Locked in ($0.01 \leq t \leq 0.025$), Ending transient ($0.025 \leq t \leq 0.035$) and unforced ($0.035 \leq t \leq 0.05$).

Table 3: Summary of parameters chosen for the POD dataset, spatial domain and method study.

Case	Spatial Domain	Data Set			$\bar{\epsilon}(t)$	
		Di	F_f [Hz]	A/U_∞ [%]	POD	DPOD
1	X1	D1	400, 600, 800	2.5, 5, 10	0.58%	0.55%
2	X2	D1	400, 600, 800	2.5, 5, 10	0.67%	0.52%
3	X3	D1	400, 600, 800	2.5, 5, 10	0.45%	0.37%
4	X1	D2	400, 600, 800	2.5, 5, 10	0.57%	0.45%
5	X2	D2	400, 600, 800	2.5, 5, 10	0.66%	0.46%
6	X3	D2	400, 600, 800	2.5, 5, 10	0.45%	0.35%
7	X1	D3	400, 600, 800	2.5, 5, 10	0.54%	0.42%
8	X2	D3	400, 600, 800	2.5, 5, 10	0.65%	0.44%
9	X3	D3	400, 600, 800	2.5, 5, 10	0.44%	0.33%

The POD mode sets were truncated to 5 modes for POD and 5x2 modes for DPOD. Therefore, DPOD was expected to perform better at reconstruction of the density field than POD. The error values in the last two columns in Table 3 show the training data selection and spatial domain choice did influence the reconstruction error. It decreased slightly for larger, more comprehensive data sets. Also, the reconstruction error decreased proportionally to the spatial domain, suggesting that by limiting the spatial domain size, certain flow features that do not contribute to the shear layer physics under investigation, such as the recirculation zone, were neglected. Most importantly, the errors indicate that it is crucial to retain as much information about the flow field as possible, shown by the fact that the smallest errors were obtained using dataset D3, which includes the unforced and forced data as well as both startup and shutdown transients. However, the main outcome of this parameter study was that the reconstruction error was not a good way to quantify which mode set to choose as the final numeric model. All of the error values were acceptable (< 1 per cent), which would suggest that all these parameter combinations would be adequate.

Scrutinizing the differences between POD and DPOD provides insight into the shear layer dynamics as forcing is applied to the flow. From theory as well as the experimental data obtained in this project, it is well known that the shear layer is extremely susceptible to periodic forcing. Due to the flow's instability, small perturbations over a wide frequency range are amplified and result in Kelvin-Helmholtz vortices [see e.g. Oster and Wygnanski, 1982]. The shift modes for the DPOD mode sets ($\phi_{i,2}$), shown in Figures 28, 31, and 34, model the transient change from the natural shedding to a forced state, but the shift modes show a change in wavelength compared their corresponding main mode, indicating that there was not a slow shift from the natural to a forced state. The data suggested that for the shear layer, the flow response was different because the frequency band in which lock-in occurs is much larger than for flows such as the cylinder wake. As seen from these DPOD modes, the shear layer structures assume a different wave length when forced at a given frequency. The transient behavior is extremely fast, thus making the underlying concept of DPOD questionable. In addition, the spatial modes for the DPOD decomposition lack physical relevance.

The POD models for cases 1, 6, and 8 are shown in Figures 29, 32 and 35, respectively. The mode sets show the mean flow and the first 2 mode pairs. As expected, there is a distinct size/wavelength change for the 2 mode pairs. The modes in the POD mode sets also look physically viable, unlike the DPOD mode sets. Therefore, POD, not DPOD, was chosen as the preferred modeling approach for the shear layer.

When the reconstruction error is evaluated as a function of time, as in Equation 67, DPOD should better represent the flow field in the transient regions whereas POD should fail to model these transitions from one flow state to another. Figures 30, 33, 36 show that this was not the case. In fact, the reconstruction error is smaller for the POD approximation than for the DPOD one. This corroborates the assertion that the five supplemental shift modes were not really modeling transient flow effects in the shear layer.

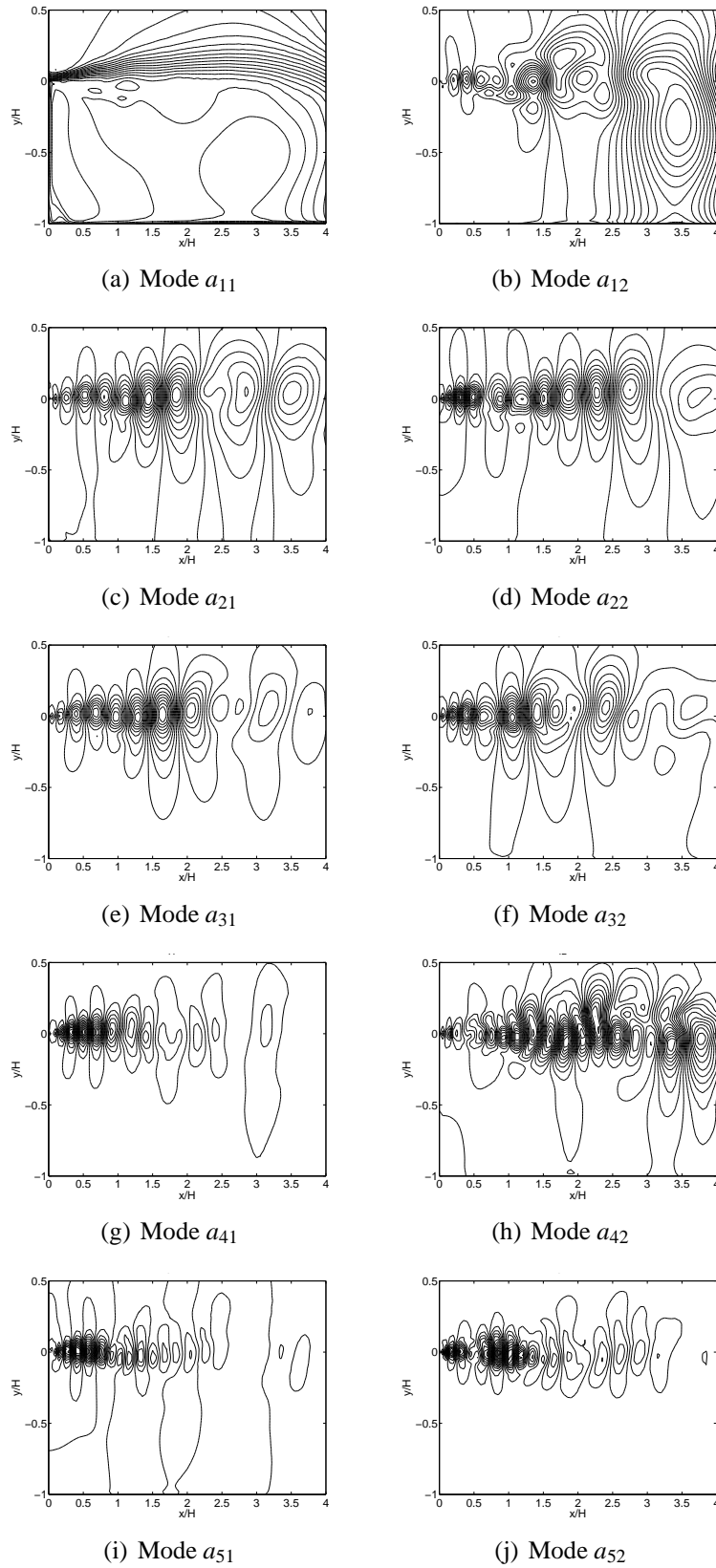


Figure 28: Case 1: DPOD modes ϕ_{ij} for parameters shown in Table 3. Left column: Main modes ϕ_{i1} , right column: Shift modes ϕ_{i2} .

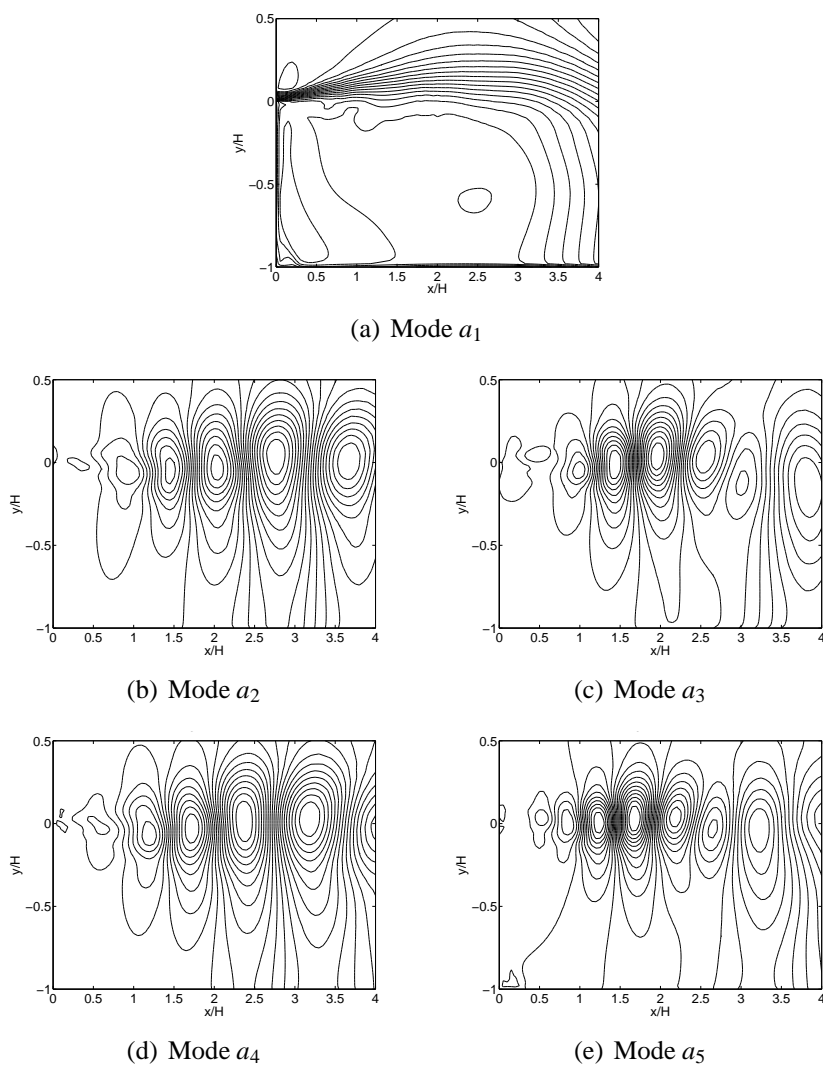


Figure 29: Case 1: POD modes ϕ_i for parameters shown in Table 3. a) Mean flow mode, b) and c) first fluctuating mode pair, d)-e) first harmonic mode pair.

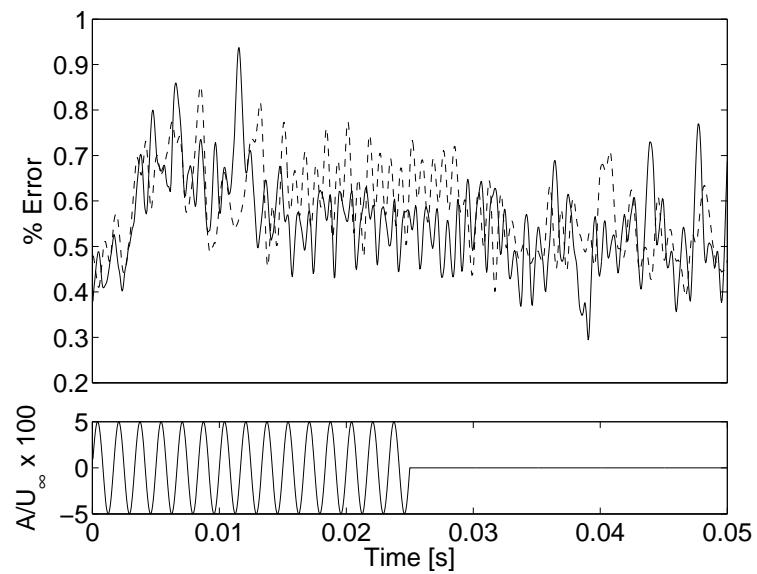


Figure 30: Case 1: (Top) Reconstruction error as a function of time of numerical model, (—) POD, (---) DPOD. (Bottom) Forcing signal for validation case. Transient period in flow field begins around, lock in region to $t = 0.03$ s, ending transient until $t = 0.035$ s where the natural flow state occurs.

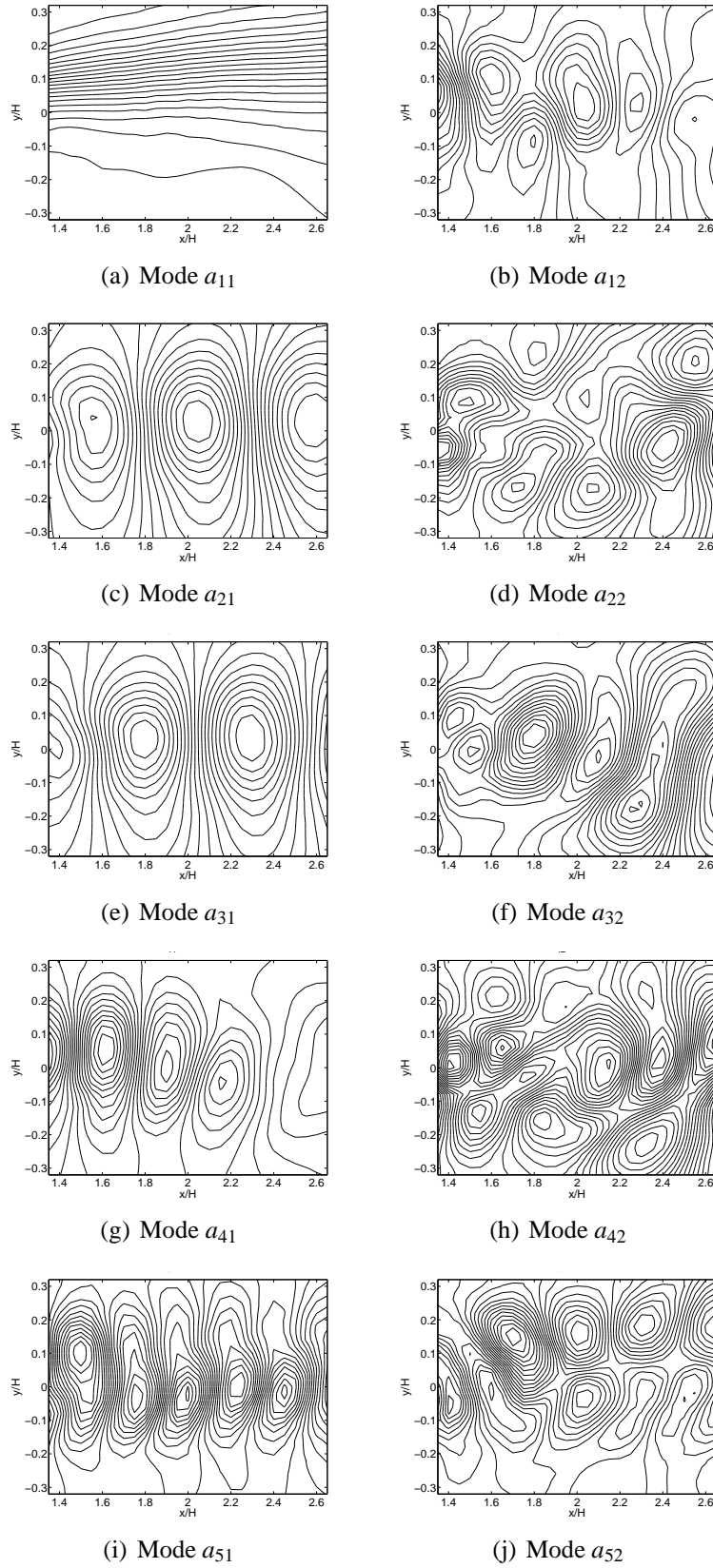


Figure 31: Case 6: DPOD modes ϕ_{ij} for parameters shown in Table 3. Left column: Main modes ϕ_{i1} , right column: Shift modes ϕ_{i2} .

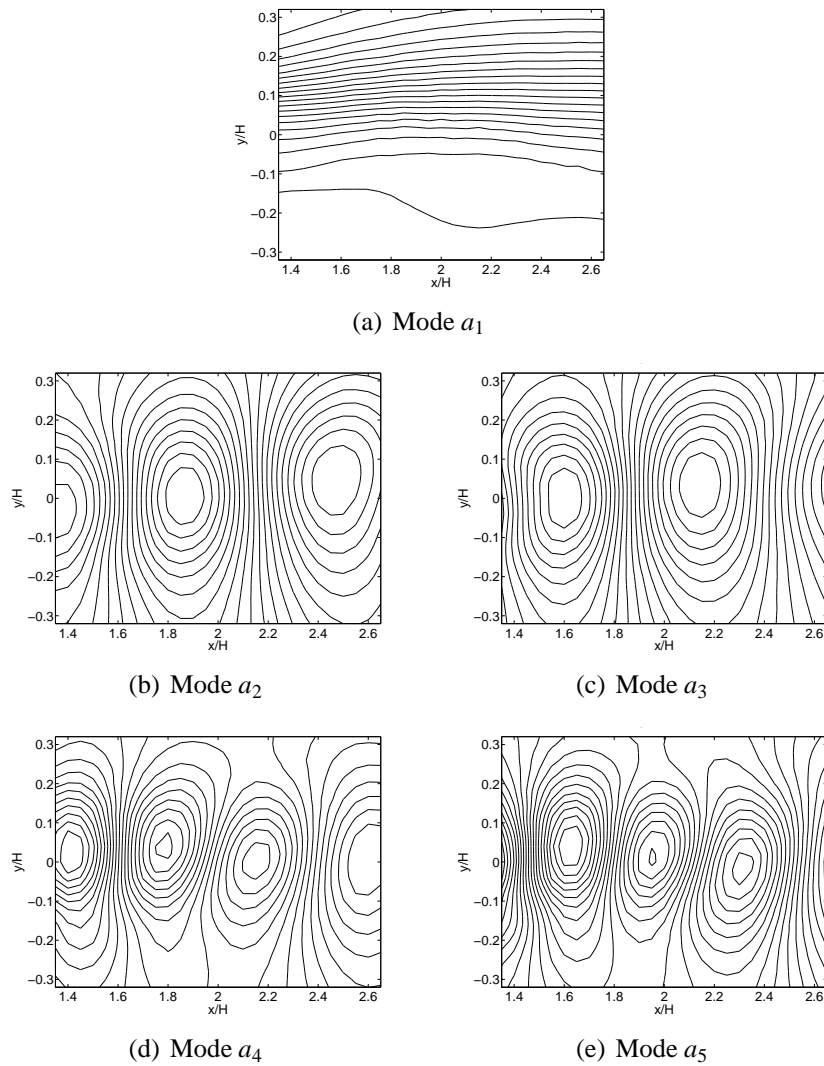


Figure 32: Case 6: POD modes ϕ_i for parameters shown in Table 3.

The only parameter left to choose was the spatial domain. The spatial domain sets were chosen to be the entire flow field behind the step (X1), just the shear layer neglecting the recirculation zone (X2) and the shear layer over the optical aperture (X3). Because the reconstruction error, as shown in Table 3, did not provide a reliable criterion for which spatial domain was appropriate, the domain was chosen on a physical basis. The first spatial domain, X1, limited the ability to capture the dynamics of interest by retaining undesirable flow physics, such as the recirculation zone, in the domain. As shown in Figure 37, the mode amplitudes obtained for the validation case ($F_f = 600\text{Hz}$, $A/U_\infty = 0.10$) showed some low frequency content, which originated most likely from the recirculation zone. Figure 38, the corresponding data for domain X2, exhibits much more periodic mode amplitudes, which are representative of the structures in the shear layer.

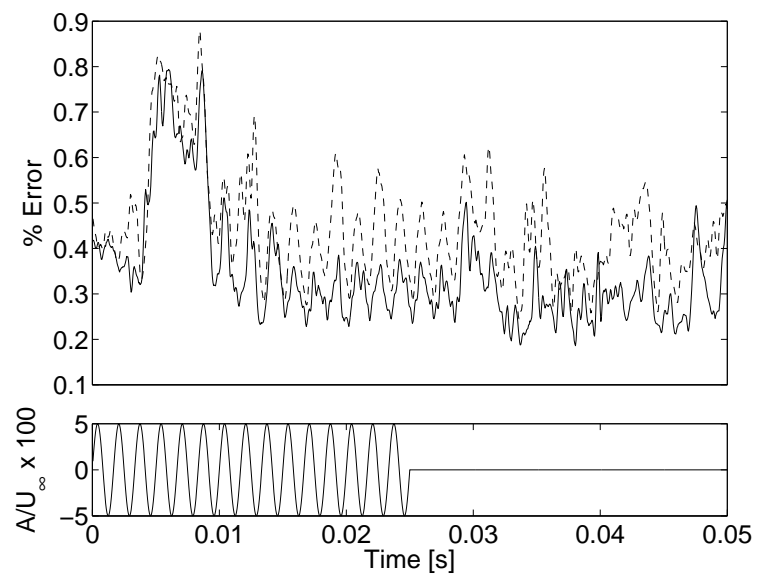


Figure 33: Case 6: (Top) Reconstruction error as a function of time of numerical model, (—) POD, (---) DPOD. (Bottom) Forcing signal for validation case. Transient period in flow field begins around $t = 0.005s$, lock in region to $t = 0.03s$, ending transient until $t = 0.035s$ where the natural flow state occurs.

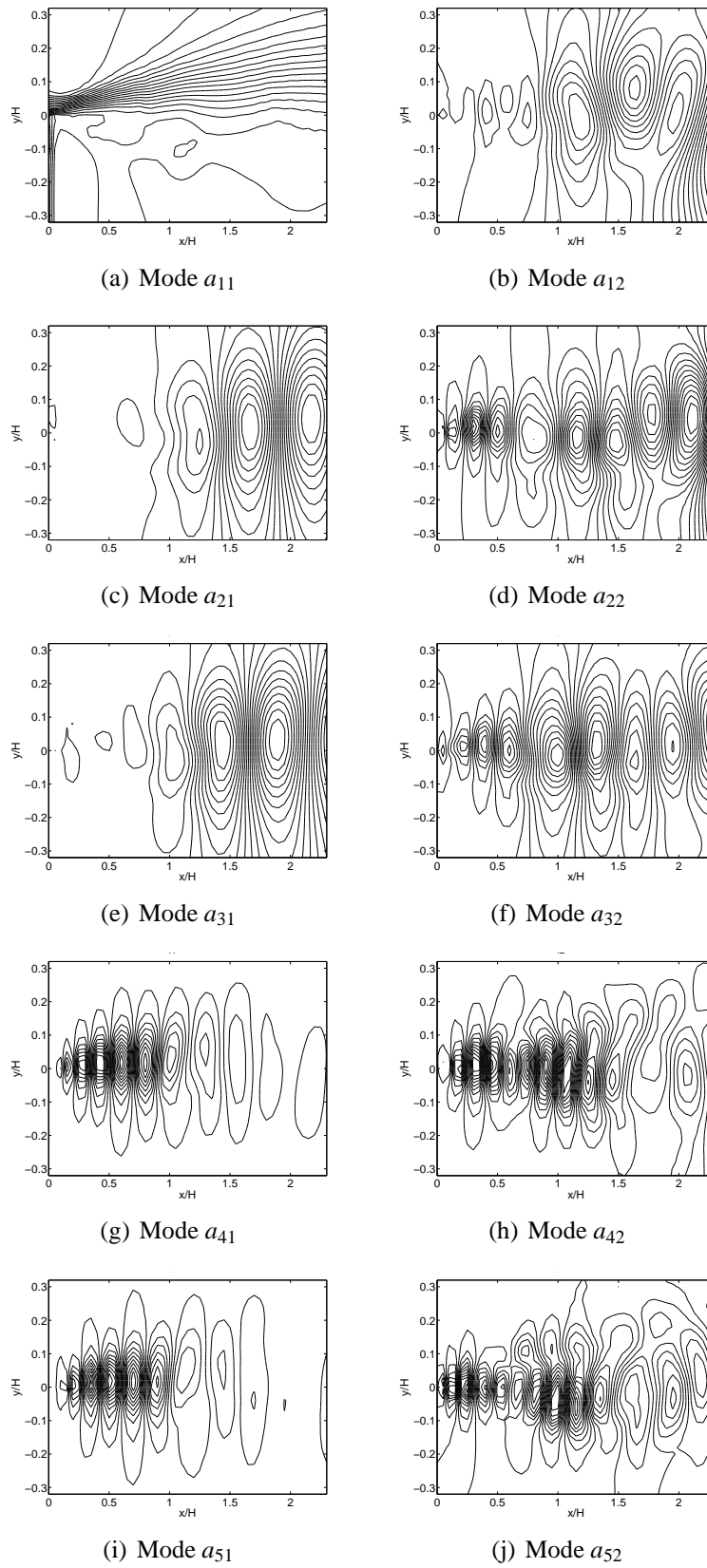


Figure 34: Case 8: DPOD modes (ϕ_{ij}) for parameters shown in Table 3. (a)(c)(e)(g)(i) Main modes(ϕ_{i1} , (b)(d)(f)(h)(k) Shift modes (ϕ_{i2}).

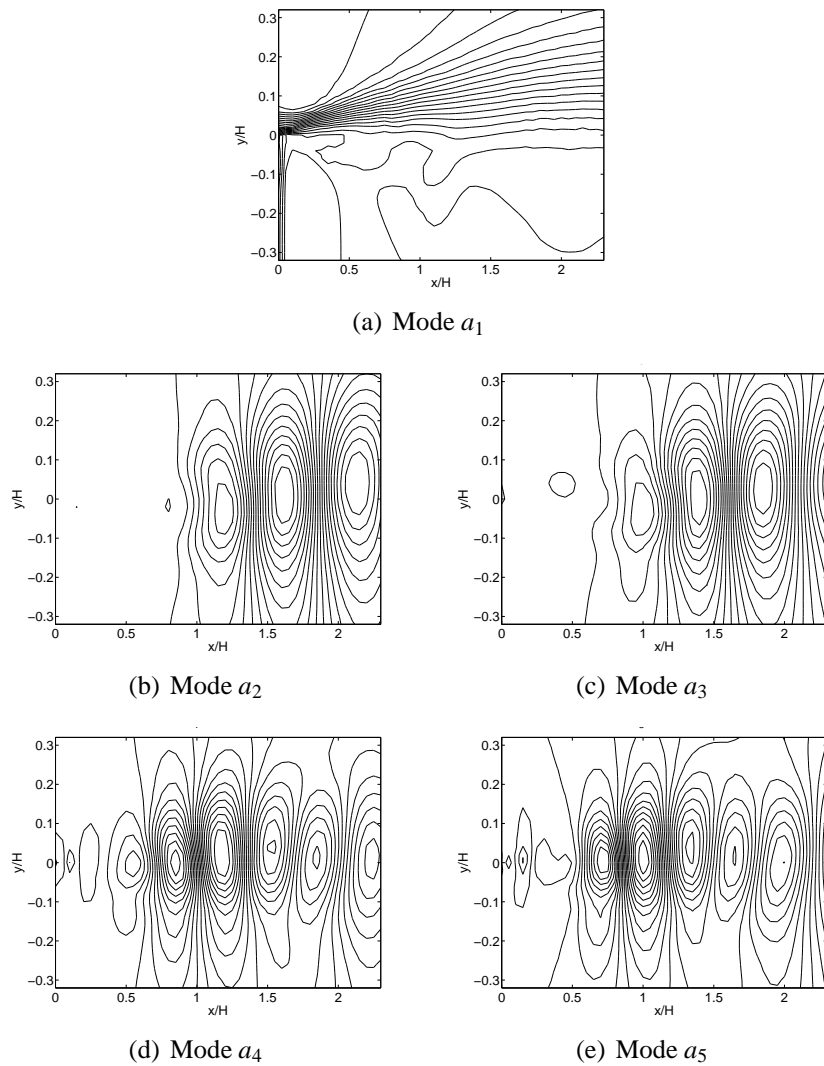


Figure 35: Case 8: POD modes (ϕ_i) for parameters shown in Table 3.

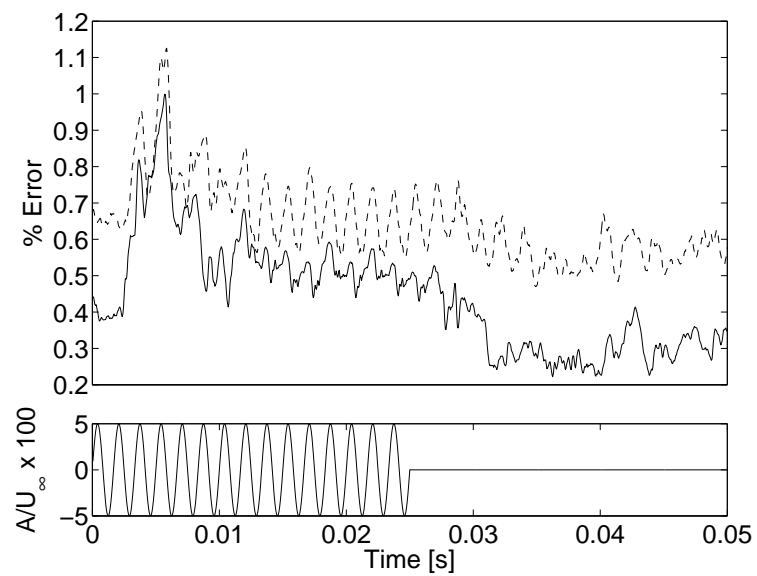
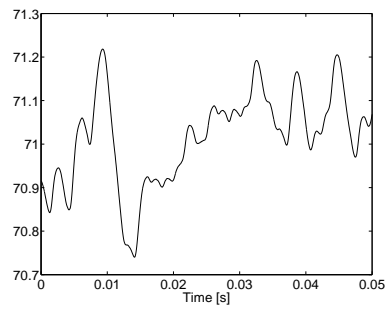
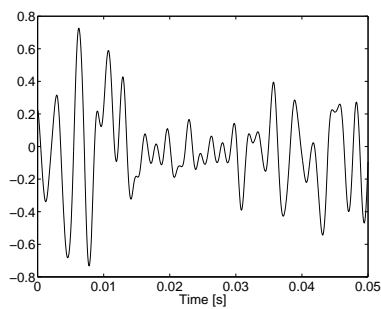


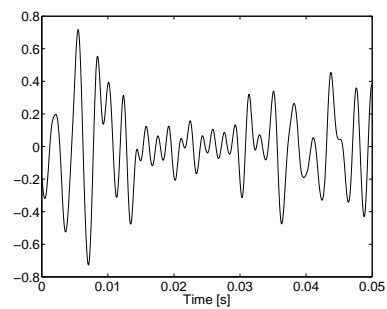
Figure 36: Case 8: (Top) Reconstruction error as a function of time of numerical model, (—) POD, (---) DPOD. (Bottom) Forcing signal for validation case. Transient period in flow field begins around $t=0.005s$, lock in region to $t= 0.003s$, ending transient until $t=0.0035s$ where the natural flow state occurs.



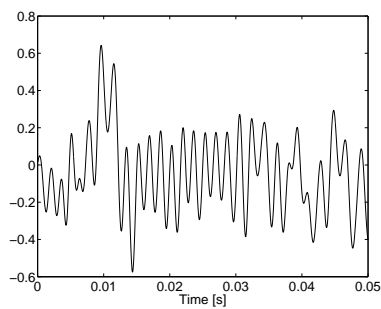
(a) Mode a_1



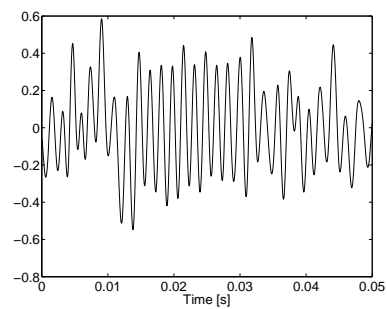
(b) Mode a_2



(c) Mode a_3



(d) Mode a_4



(e) Mode a_5

Figure 37: Case 1: POD mode amplitudes (a_i) for parameters shown in Table 3.

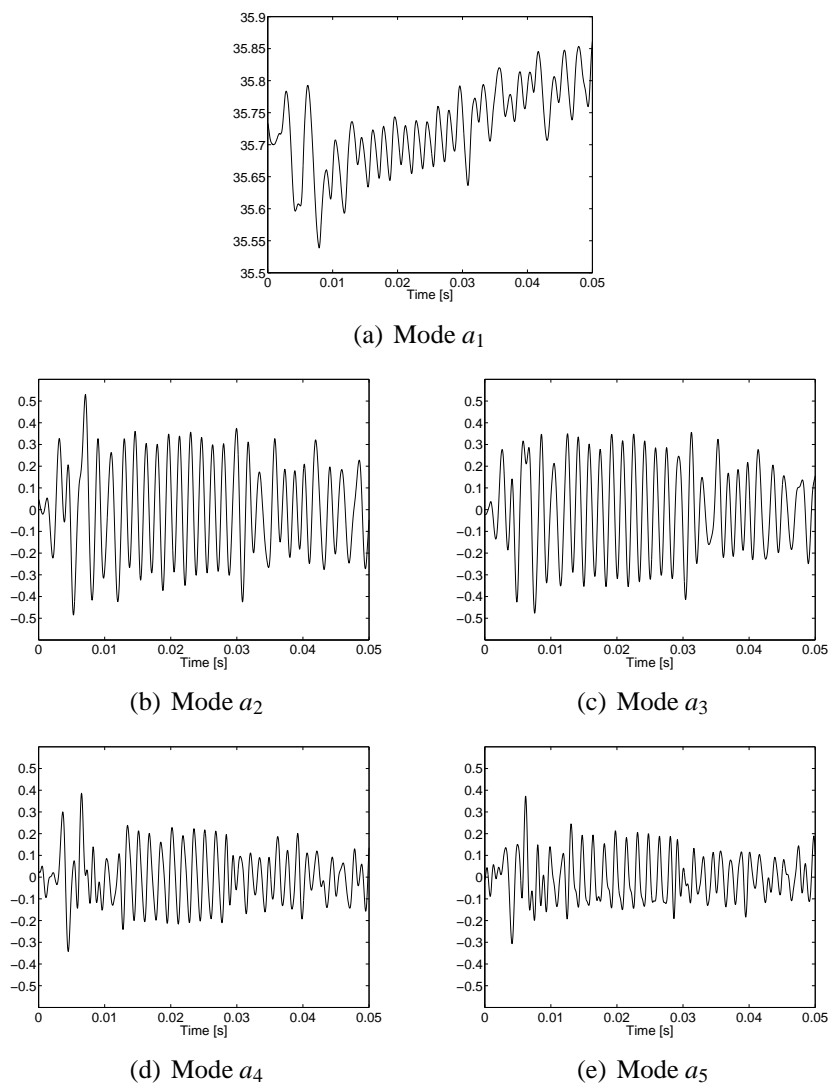


Figure 38: Case 8: POD mode amplitudes (a_i) for parameters shown in Table 3.

5.3 System Identification

Another important parameter was the size of the training data set for the model. The number and span of training cases for the WNARX model is presented in Table 4. A total of 12 open loop cases, all of which contained starting and ending transients from the unforced flow state and back to it, were computed to understand the influence of actuation with varying frequency and amplitude on the flow. The results of this investigation showed that the time coefficients reacted almost linearly to the blowing and suction amplitude, i.e. the response of the mode amplitudes, $a_j(t)$, scaled linearly with amplitude input. In contrast, the flow response was highly nonlinear with respect to the forcing frequency. Thus, the three training data sets highlighted in Table 4 were chosen to provide a basis space for the WNARX model. The case $F_f/F_n = 1$, $A/U_\infty = 0.10$ was chosen to be the validation case for the model. A summary of final parameters for the dynamic model is presented in Table 5.

Table 4: Summary of cases. \checkmark : WN training cases, o: validation case.

	400Hz	600Hz	800Hz
$A/U_\infty = 0.1$	\checkmark	o	\checkmark
$A/U_\infty = 0.05$	x	\checkmark	x
$A/U_\infty = 0.025$	x	x	x
$A/U_\infty = 0.0125$	x	x	x

The WNARX model was validated for an off design flow case for which the forcing signal was turned on at simulation time $t = 0s$, at which point the flow goes through a transient period before locking into the forcing frequency. The forcing was then turned off at $t = 0.025s$ (corresponding to 15 forcing periods) to reestablish the unforced flow state (see Figure 27). As seen in Figure 39, the model captures the lock-in region of the periodic forcing very well. Once the forcing was turned off at $t = 0.025s$, the model accurately predicted the type of nonlinear signal in the unforced flow. Expecting an exact replication of the unforced time coefficients is unrealistic since the signal was extremely nonperiodic. However, the important point is that the model of the unforced flow does not decay to zero over time. This indicates that there is a periodic attractor to the nonlinear function for the WNARX system. The similarities in periodic trends furthermore suggest that the attractor is near the solution of the unforced state.

With the development of this model, the feedback control problem of the shear layer behind a backward facing step had been transformed into the problem of designing a controller for the POD time coefficients. At this point, the previous definition of the control goal, namely minimizing the

Table 5: Summary of parameters chosen for the WNARX model.

Mode a_i	Wavelets	Regressors				
		a_1	a_2	a_3	a_4	u
a_1	2	4	1	0	0	1
a_2	21	1	5	0	0	1
a_3	10	0	0	4	2	2
a_4	16	0	0	2	4	2

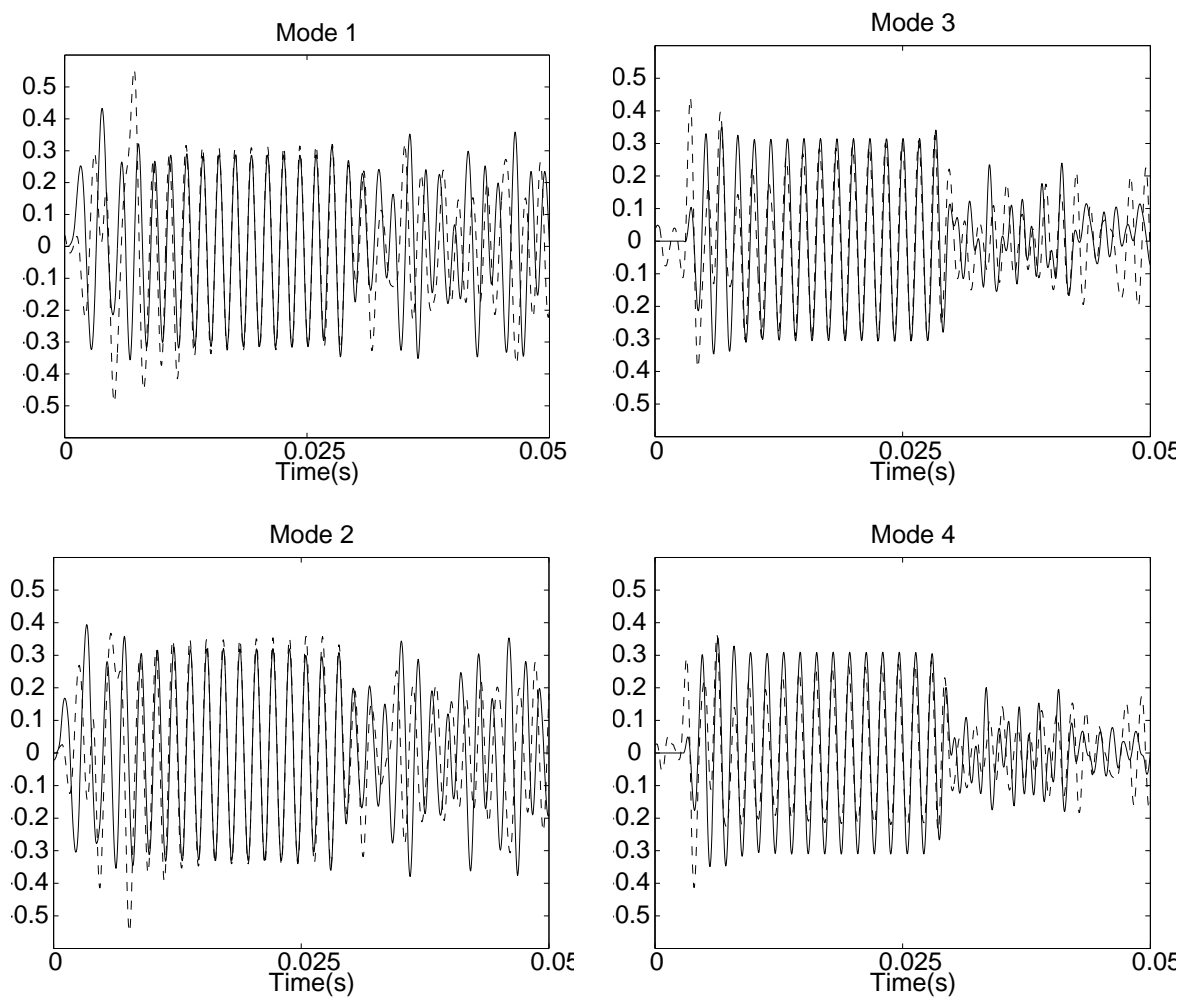


Figure 39: Off design validation of the four mode WNARX model for flow case of $F_f = 600\text{Hz}$ and $A/U_\infty = 0.1$. WNARX output (—), POD model (- -).

Table 6: Summary of parameters chosen for surface mounted sensor estimation scheme.

Study	# of Sensors	Data Set			Error $\bar{\epsilon}(t)$		
		$A(\frac{u'}{U_\infty})$	Pressure	SPOD TC	LSE	ANNE	WNE
1-3	47	2.5% 5% 10%	✓	-	21%	19%	12%
4-6	47	2.5% 5% 10%	-	✓	22%	20%	12%
7-9	47	2.5% 5% 10%	✓	✓	11%	9.5%	4.6%
10-12	47	5% 10%	✓	✓	10.9%	9.6%	4.6%
13-15	8	5% 10%	✓	✓	11.2%	10.8%	4.7%
16-18	6	5% 10%	✓	✓	18.8%	16.5%	5.2%
19-21	4	5% 10%	✓	✓	20.5%	19.2%	8.1%
22-24	2	5% 10%	✓	✓	23.1%	19.9%	21%

density fluctuations in the flow field, was replaced by a much more tractable problem: Design a controller for the *model of the POD time coefficients* whose dimensionality is orders of magnitude less than that of the underlying CFD flow field data. Finding a model that described a flow field that was not included in the model design with the fidelity shown was a major step toward developing successful feedback flow control strategies for the free shear layer flow.

5.3.1 Feedback Control

5.3.1.1 State Estimation A parameter study was conducted for the state estimator formulation. Because the density of the fluid cannot be directly measured on the surface behind the step, pressure variations, which directly correlate to the density fluctuations in the flow (with the assumption of constant temperature), were chosen as viable surface measurements. Five forcing cases, which contained starting and ending transients (see Table 2) were used as state estimator training data. The case $F_f = 600\text{Hz}$, $A/U_\infty = 0.1$ (Table 2) was reserved for validation purposes. It should be noted that the error of the training data is bounded above by the error of the validation case, that is

$$\|e_{Train}\| \leq \|e_{Val}\|, \quad (69)$$

for all cases. Therefore, the error of the validation case will suffice to determine the performance of the estimation method. Table 2 shows that the estimator was interpolating between cases; the accuracy of the estimator outside the *training region* has not been verified.

Determining the appropriate parameters for the state estimator began by defining the physical locations of the sensors. The floor behind the step from $0 \leq x_s \leq 2.5H$ contained a total of 47 possible sensor locations. All three estimation methods (LSE, ANNE, WNE) were applied to the full state sensor array (i.e. $\dim(x_s) = 47$) to determine the best performance of the estimation methods. The sensor array was then down-sampled to the minimum number of sensors (i.e. $\dim(x_s) = 2$) and incrementally increased until the error converged to the full state sensor estimation performance. The parameters of the training methods for ANNE and WNE were held constant throughout this study. A total time history of 25 time steps was used in the formulation of the regression vector (i.e. $n = 25$ in Equation 38). The results are summarized in Table 6.

Figure 40a) shows the error in the estimation of mode 1 as a function of the number of sensors. The results indicate that all of the methods rapidly converge to approximately their final performance level with the use of 8 sensors spaced equally between $x/H = 0.25$ and $x/H = 2$. More

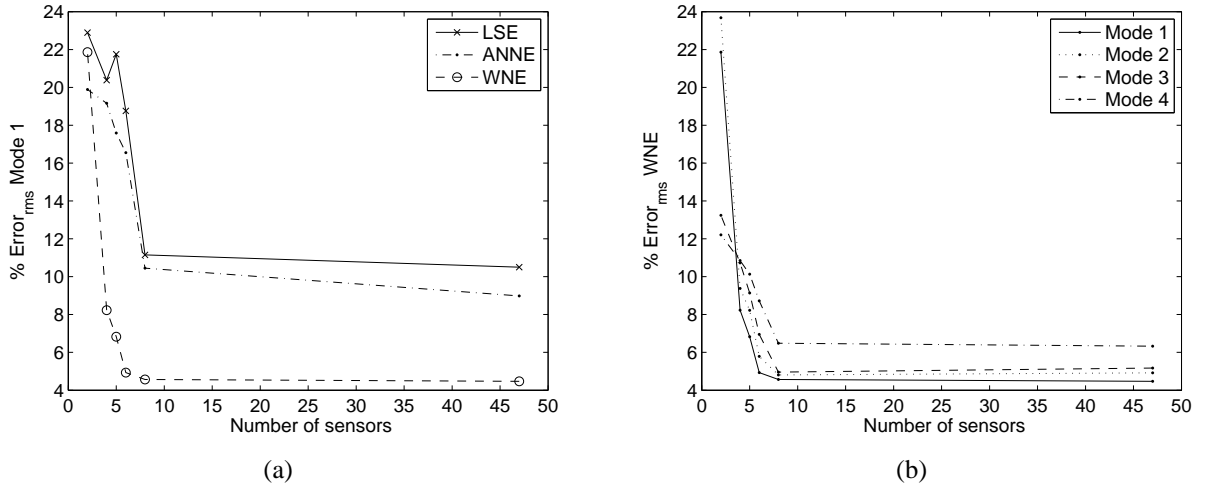


Figure 40: Estimation error for validation case $F_f = 600\text{Hz}$, $A/U_\infty = 0.1$. a) Root mean squared error of mode 1, $a_1(t)$, all estimators. b) Root mean squared error of modes 1-4 using the wavenet estimator (WNE).

interestingly, the wavenet estimation method resulted in only half the error of the other methods (4.5 per cent for $\dim(x_s) = 8$). In Figure 40b), the errors for all four modes as computed using the WNE estimator are plotted as a function of the number of sensors. The plot indicates that while the error increased somewhat for the higher modes, all modes were converged when using only eight sensors.

The results obtained with the full state sensor array along with surface POD time coefficients (Study 10-12) are shown in Figure 41. This is the *best* possible result given the amount of information and infinite training time. The conclusion of this study represented a trade off between the number of sensors needed for precise estimation and the wavenet training time. The goal was to have the minimal number of sensors for accurate estimation while maintaining a physically feasible sensor configurations.

Figure 42 shows the estimation results for only two sensors in the sensor configuration. From the error computations, it is clear that the estimators need larger sensor arrays for accurate estimations of the flow field. Figure 43 is the optimal sensor configuration which was determined to be an array of eight sensors between $x_s/H = 0.25$ and $x/H = 2$. RMS errors were on the order of 5 per cent for this sensor configuration, which was equivalent to the error of the estimation using the full state sensor estimate. Figure 44 shows a comparison of the actual time coefficients computed from Equation 17 with the simulated WNE computed from Equation 27 using the eight sensors. The estimator captures both the phase, frequency, and amplitude of the flow states for the validation case. At this point the density field could be reconstructed with an error of less than 5 per cent of the original flow field using only eight sensors by combining surface POD (Equation 17) and the flow state estimate (Equation 27) within the forcing parameter space.

5.3.2 Adaptive Control

Direct adaptive feedback control [see Fagley et al., 2009, for more details] was chosen to close the feedback loop. Adaptability allows for uncertainties when scaling the controller for validation in

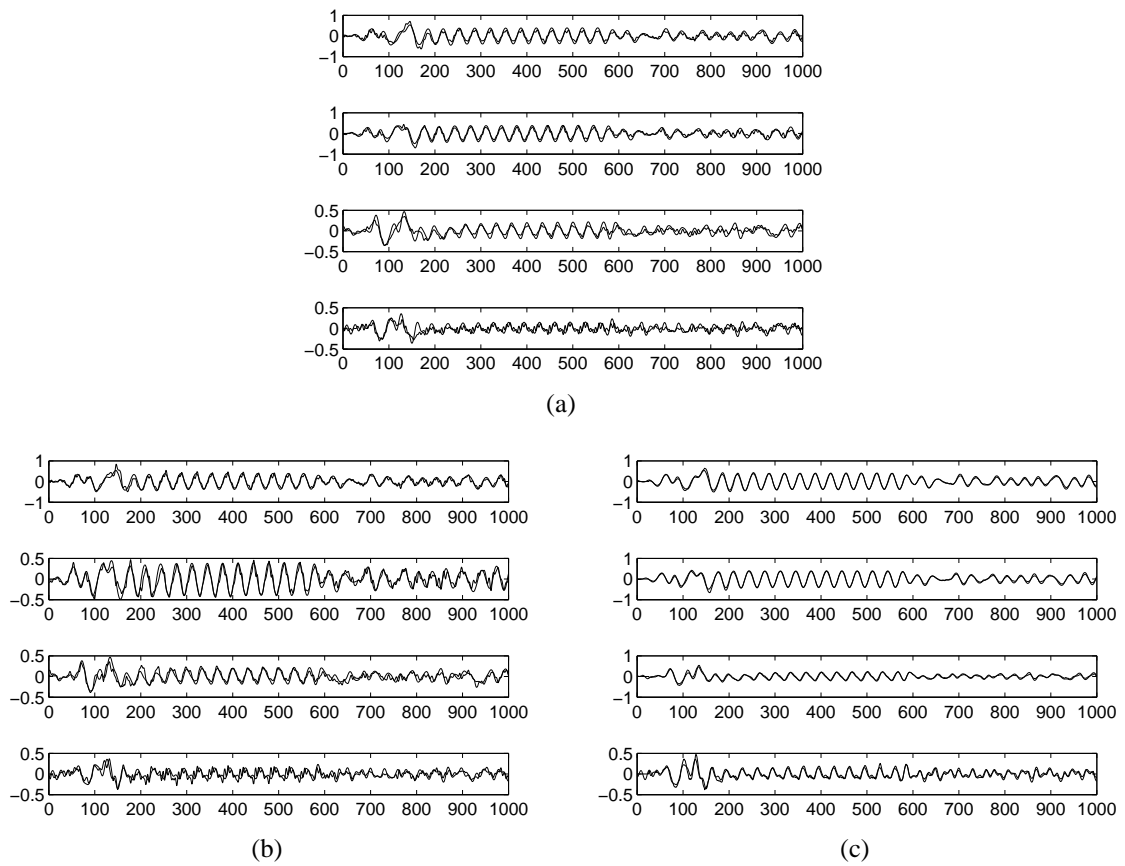


Figure 41: Estimation using full sensor array of forcing validation case ($F_f = 600\text{Hz}$, $A/U_\infty = 0.1$). Forcing on for first half of simulation, off for second. a) Study 10: LSE estimations ($\varepsilon = 10.9\%$) b) Study 11: ANNE estimations ($\varepsilon = 9.6\%$) c) Study 12: WNE estimations ($\varepsilon = 21\%$).

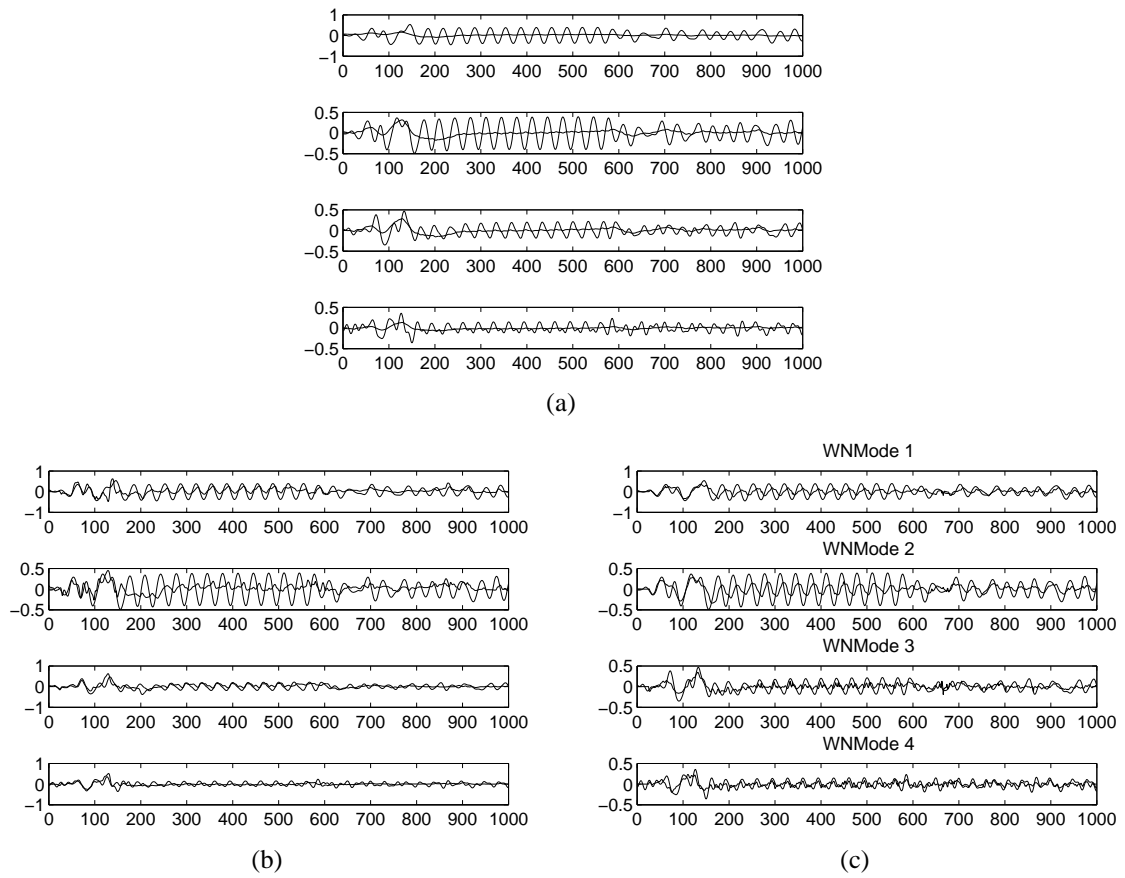


Figure 42: Estimation using smallest sensor array of forcing validation case ($F_f = 600\text{Hz}$, $A/U_\infty = 0.1$). Forcing on for first half of simulation, off for second. a) Study 22: LSE estimations ($\epsilon = 23.1\%$) b) Study 23: ANNE estimations ($\epsilon = 19.9\%$) c) Study 24: WNE estimations ($\epsilon = 4.6\%$).

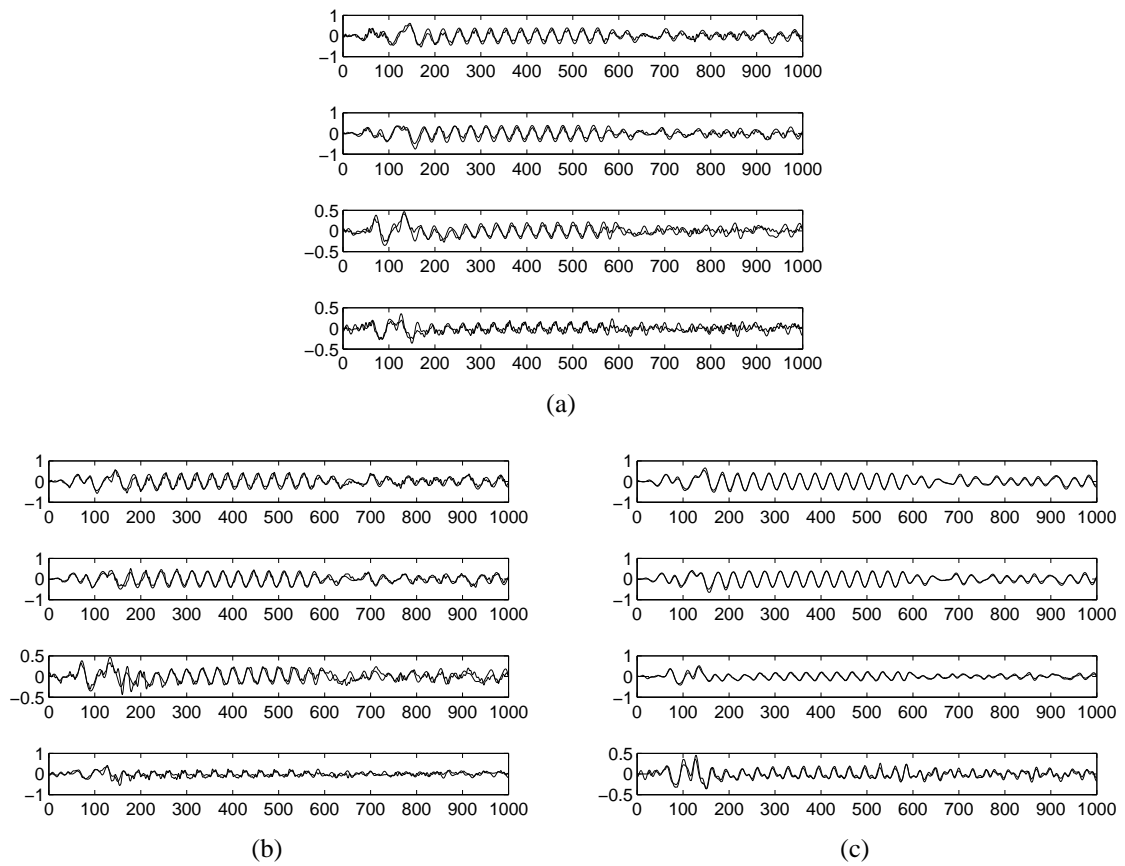


Figure 43: Estimation using full sensor array of forcing validation case ($F_f = 600\text{Hz}$, $A/U_\infty = 0.1$). Forcing on for first half of simulation, off for second. a) Study 13: LSE estimations ($\varepsilon = 11.2\%$) b) Study 14: ANNE estimations ($\varepsilon = 10.8\%$) c) Study 15: WNE estimations ($\varepsilon = 4.6\%$).

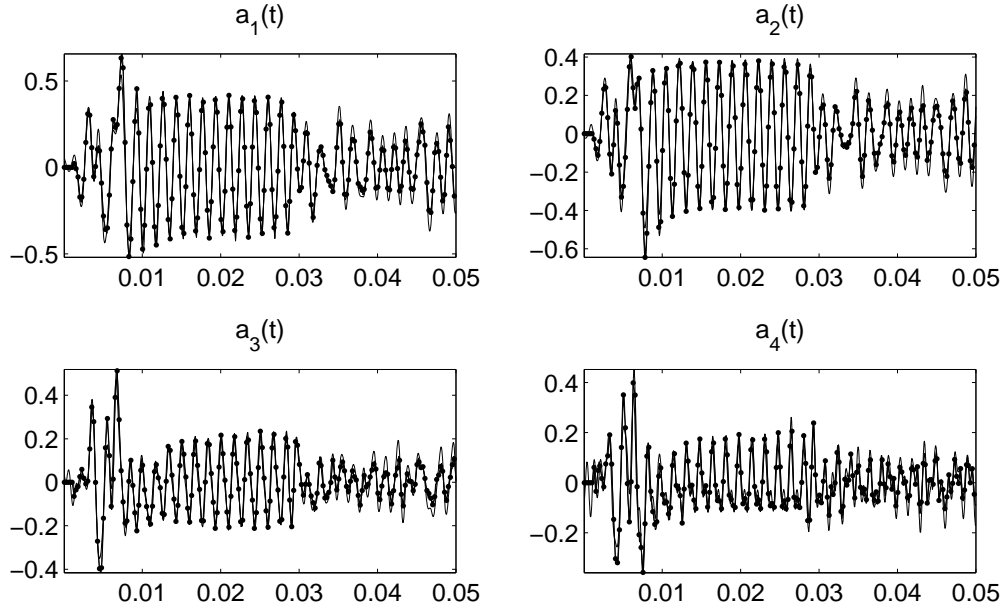


Figure 44: Comparison of first four POD time coefficients for the validation case $F_f = 600\text{Hz}$, $A/U_\infty = 0.1$. —, CFD results, - · -, WNE with eight sensors. Forcing was active for $t < 0.025\text{s}$.

CFD simulations and experiments. The basic equations describing direct adaptive control are

$$\begin{aligned} U &= G_e e_y \\ \dot{G}_e &= -e_y e_y^T \gamma_e, \end{aligned} \quad (70)$$

where G_e is the gain matrix, γ_e is the adaptability weight, and e_y is the error between output and desired reference signal,

$$e_y = \hat{a} - a_{ref}. \quad (71)$$

For multi input multi output (MIMO) systems, e_y and γ_e are matrices of size $n_{out} \times n_{in}$. Also, the gain matrix is of size $n_{in} \times n_{out}$. The derivative must be approximated numerically, because no analytic solution exists. Here, the fourth order Adams-Bashforth method,

$$\dot{G}_e \simeq \frac{G_{en+1} - G_{en}}{\Delta t} = \left(e_{yn} + \frac{1}{2} \nabla e_{yn-1} + \frac{5}{12} \nabla^2 e_{yn-2} + \frac{3}{8} \nabla^3 e_{yn-3} \right), \quad (72)$$

was utilized to determine the gain matrix derivative. The feedback parameters associated with this control strategy are primarily which mode is used for feedback and the adaptability weights which are typically less than one. Stability of this type of control system is only proven for linear systems Fuentes and Balas [2000]. Stability margins cannot be shown for our nonlinear system of equations with adaptive control; however, stable simulations provide empirical evidence.

5.3.2.1 Feedback control of the WNARX model Developing the components for a closed loop simulation is a multi-step iterative process. The model developed above provides accurate predictions of the mode amplitudes when the flow is forced within a given frequency and parameter range, including starting and ending transients. However, it remains to be seen if the model is

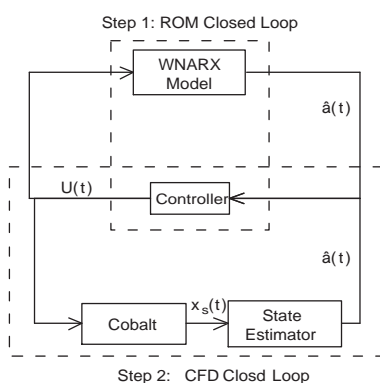


Figure 45: Block diagram of closed loop simulation strategy. Step 1: Design a controller for WNARX ROM. Step 2: Apply controller to CFD simulation with state estimator to verify model adequately predicts closed loop dynamics.

capable of adequately simulating the highly nonlinear dynamics expected for the closed loop case. Furthermore, a feedback scenario allows for a parameter study of adaptive control algorithms. The WNARX model allows for very quick simulation times, so that a parameter study can be carried out very quickly. The parameters were adjusted to feed back different combinations of modes and their derivatives along with preconditioned adaptability weights. Once desirable results were achieved with the model in a closed loop simulation, the designed control algorithm with the corresponding feedback mode combination and weights was scaled up and applied in a closed loop CFD simulation to validate both the WNARX ROM system and the adaptive controller. A diagram of the two parts of this approach is shown in Figure 45.

After the parameter study discussed above, it was determined that the POD mode amplitude a_1 and its time derivative, \dot{a}_1 , were the best parameters to be regulated in the feedback control system. The derivative of a_1 was computed by an implicit Euler approximation. Because this can be a poor approximation of the derivative and its susceptibility to noise, a moving average filter was added to smooth the estimated derivative. The initial idea was that the OPD would be reduced by simply reducing the mode amplitudes. Feedback of states a_1 and \dot{a}_1 allowed for excellent controllability of the mode amplitudes as shown in Figure 46. Note that by controlling mode 1, mode 2 was controlled as well because these modes represent the traveling wave character of the shear layer structures.

In this simulation, the open loop forced flow was used as the initial condition for the closed loop simulation to create periodicity in the flow and to improve startup performance of the controller when the loop was closed. Figure 46 shows the time coefficients for the four mode model. Periodic forcing was applied for $t < 0.015s$, at which point the closed loop control was switched on for a time period of $0.015s < t < 0.035s$, when the control is turned off and unforced flow redeveloped for $t > 0.035s$. As shown in the figure, the controller performs well, reducing the amplitudes of the time coefficients to approximately 35 per cent of the unforced state. As a final step to verify the efficacy of this control approach for aero-optical problems, the density field was reconstructed using the closed loop simulation results of the time coefficients, shown in Figure 46, and their corresponding spatial modes (Figure 32). The reconstructed density field, $\rho(x, y, t)$, allows for the evaluation of the effect of the three different forcing scenarios (unforced, open-loop forced, and

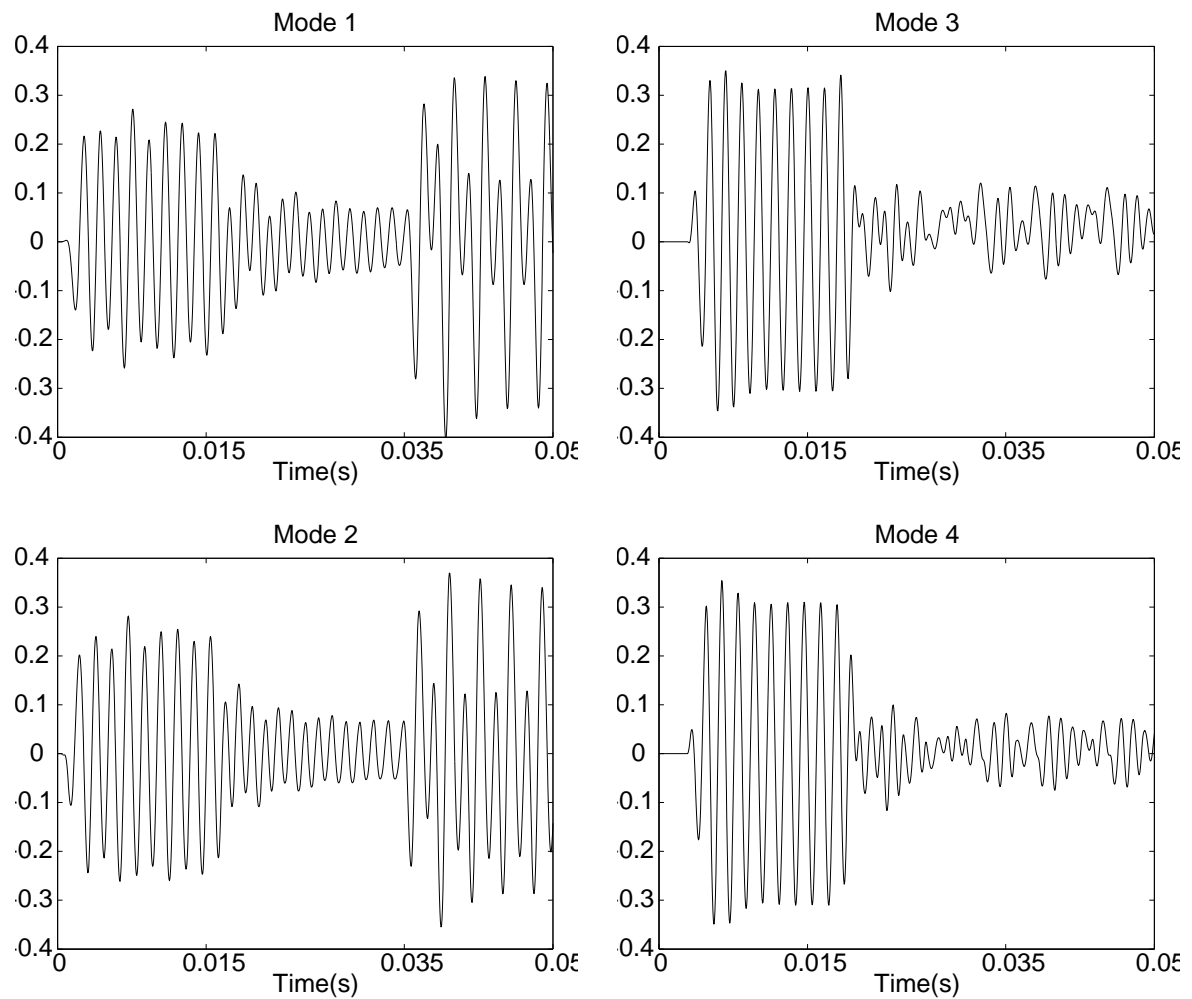


Figure 46: Feedback results using adaptive feedback control. Periodic forcing for $0s < t < 0.015s$, closed loop simulation for $0.015s < t < 0.035s$, and unforced simulation for $t > 0.035s$.

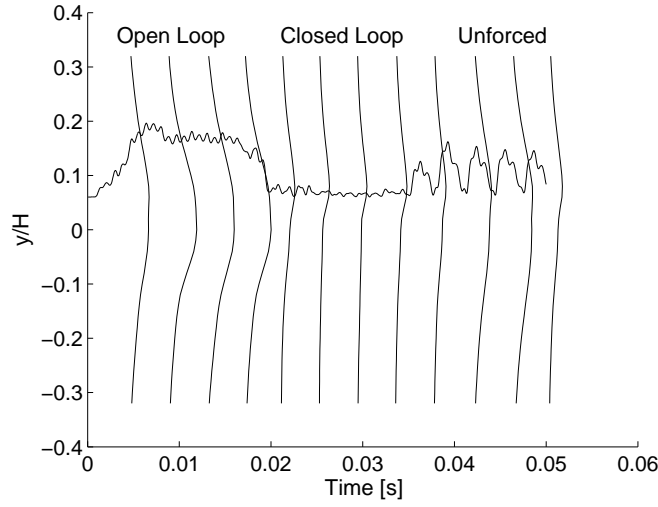


Figure 47: Feedback results using adaptive feedback control. Periodic forcing for $0s < t < 0.015s$, closed loop simulation for $0.015s < t < 0.035s$, and unforced simulation for $t > 0.035s$. Vertical solid lines indicate contours of $\rho'(y,t)$ normalized by the maximum density fluctuation. The Horizontal line shows the maximum density fluctuation at a given time.

feedback controlled), especially their effect on the density fluctuations. Because the density field is three dimensional in (x,y,t) -space, it is difficult to visualize the flow field dynamics. Here, the standard deviation of the density field was computed for visualization using

$$\rho'(y,t) = \sqrt{\frac{1}{N_x} \sum_{i=1}^{N_x} [\rho(x_i, y, t) - \overline{\rho(x, y, t)}^x]^2}. \quad (73)$$

Note that the mean was taken in the x -direction. In effect, with these two-dimensional simulations, perfect spanwise coherence was assumed. In Figure 47, contours of $\rho'(y)$ at discrete times are plotted as vertical lines. The figure shows that the magnitude of $\rho'(y)$ as well as the extent of the distortions in the y -direction were significantly reduced when feedback control was active. In addition, $\max(\rho'(y))$ is plotted for all times. It corroborates the reduction of the density fluctuations for the feedback controlled flow field.

As a final performance metric, the OPD for a beam passing through this flow field was computed using Equations (57)-(59). For the 2D simulations, the aperture size was $1.5 \leq x/H \leq 2.5$ with unit width. The OPD at the point of interest, $x/H = 2$, is plotted in Figure 48, which shows that the OPD was drastically reduced during the closed loop portion of the simulation, both in comparison to the periodically forced flow and to the unforced flow.

5.3.2.2 Feedback control in the CFD simulation The final validation of the controller developed during this research effort was performed by implementing the controller in the Cobalt CFD simulations. Hooks had been added in the Cobalt CFD code during an earlier AFOSR funded STTR project between Cobalt Solutions, LLC, and the US Air Force Academy. These hooks make sensor information available to Matlab[®] which handles the controller computations. After the actuator output had been determined, it was passed back to the Cobalt simulation using

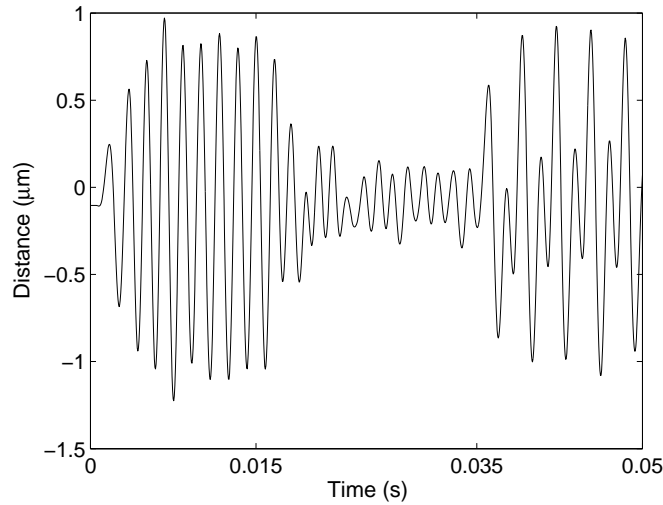


Figure 48: Calculated optical path difference at $x/H = 2$, $y/H = 0$ for the reconstructed flow field of the closed loop simulation. Periodic forcing for $0s < t < 0.015s$, closed loop simulation for $0.015s < t < 0.035s$, and unforced simulation for $t > 0.035s$.

externally controlled blowing and suction boundary conditions. The program communication between Matlab[®] and Cobalt allows for great flexibility when incorporating feedback control, filters, state estimators, etc. within a CFD simulation. More importantly, it allows for utilization of the exact programs developed in the previous sections, which significantly reduces the possibility of program errors.

For the first validation step, the controller in the previous section was directly used in the CFD simulation in conjunction with the state estimator developed in Section 5.3.1.1. The feedback controlled simulation proceeded as follows: First, the Cobalt simulation was advanced one time step. The new data at the sensor locations (predetermined, see Section 4.2.4.2) was then passed to the Matlab[®] state estimator to estimate the POD mode amplitudes; the estimation was seen to be essentially the same as what the model predicted. These POD mode amplitude estimates were then input into the control algorithm, whose output was converted to a blowing and suction mass flow rate for the blowing and suction slot. Finally, this information was passed back to Cobalt as a new boundary condition value to be used in the subsequent CFD iteration.

After completing the simulation with this controller, the density field data was used to compute the OPD. First, as before, the density fluctuations were computed and plotted using the same method as for the WNARX validation (Figure 47). Figure 49 shows that the controller developed using the ROM had a pronounced effect in reducing the density fluctuations, similar to the effect observed in the model simulation results.

The OPD results in Figure 50 show that the controller (active for $t > 0.025s$) reduces the OPD, but the reduction was slower than predicted by the WNARX model. This was most likely due to discrepancies between the reduced order model and the CFD simulation results, indicating that the ROM did not quite capture all the intricate nonlinear dynamics of the flow field which were resolved in the CFD simulation. As shown in Table 5, the model assumed that modes a_1 and a_2 are completely decoupled from modes a_3 and a_4 . This was likely the most dramatic modeling shortfall

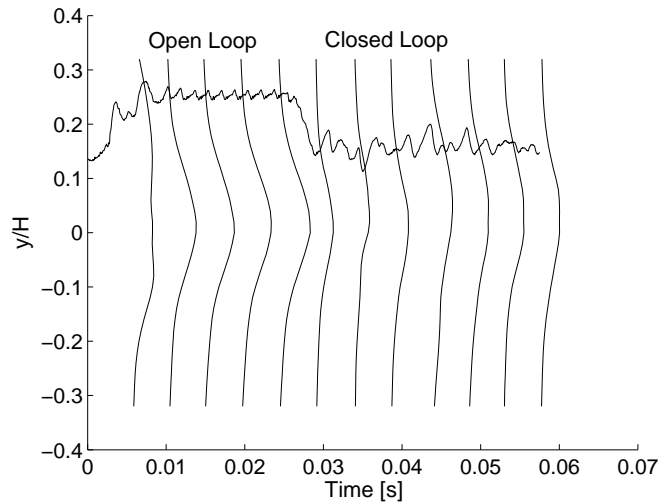


Figure 49: Density analysis of CFD closed loop simulation. Periodic forcing for $0s < t < 0.025s$, closed loop simulation for $t > 0.025s$. Vertical solid lines indicate contours of $\rho'(y,t)$ normalized by the maximum density fluctuation. The Horizontal line shows the maximum density fluctuation at a given time.

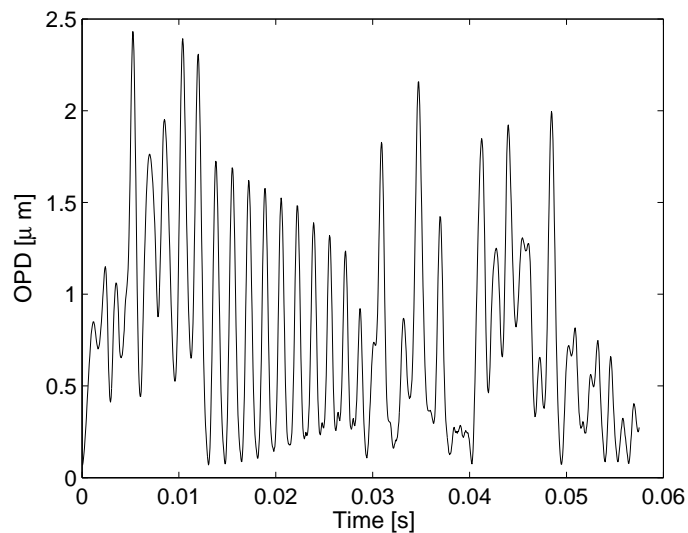


Figure 50: OPD as a function of time. CFD results with WNARX controller directly substituted into CFD closed loop simulation.

and the reason that the model did not correctly capture the nonlinear dynamics in the closed loop simulation. Further analysis of this closed loop simulation was performed to better understand these differences.

Figure 50 shows that it took approximately $\Delta t = 0.025\text{s}$ after the controller activation for the control to be effective in reducing the OPD. Full control was achieved for $t > 0.05\text{s}$, at which time the large amplitude oscillations due to flow transients, have convected downstream. The OPD amplitude was reduced by approximately 50 per cent. Scrutinizing Figure 51e, the time history of the control input, corroborates that at time $t = 0.05\text{s}$, the controller had started to achieve the control goal of minimizing the POD mode 1 amplitude (Figure 51a) and reduced the forcing amplitude to approximately $A/U_\infty \simeq 0.01$, which was less than one per cent of the free stream velocity.

The remaining POD mode time coefficients are shown in Figure 51b-d. Since POD mode 2 (Figure 51c) is the complement to mode 1 to comprise a traveling wave, it was not surprising that its amplitude was reduced in unison with mode 1. However, modes 3 and 4 behaved differently; the main effect of forcing on these modes seemed to be a stabilization of their oscillation frequencies and also their amplitudes.

When this research project was started, it was believed that a reduction of the OPD would have to be coupled to the minimization of these mode amplitudes, since each mode pair represents they flow state created when the shear layer is forced with a given frequency. However, the results indicate that the shear layer is far too unstable and quickly moves away from the natural periodic attractor when forcing is applied. A comparison of the OPD results with the POD mode amplitudes seems to suggest that the desired flow state is in fact achieved by introducing a new periodic state which reduces the OPD for a given aperture location and size. Because discrepancies between the reduced order model and the CFD simulations did exist, in the final step of this research project, the controller parameters in Equation 70 were adjusted by scrutinizing the CFD results directly to increase closed loop performance, efficacy and efficiency. These results are presented in the following.

Since it was determined from the initial feedback controlled CFD results that information about POD modes 3 and 4 needed to capture the transient behavior better, a combination of mode amplitudes and their derivatives were fed back in numerous CFD simulations to determine the optimum combination for the adaptive control algorithm. It was found that feeding back the time coefficients of one of the modes of the next mode pair, a_3 , with an aggressive adaptability weight, $\gamma_e = 1$, introduced this periodic attractor, which effectively reduced the density fluctuations and therefore the OPD over a given aperture. Figures 52 and 53 show the final successful closed loop simulation and the corresponding reduction of the OPD to approximately 30 per cent of its original value. This presents a performance improvement of almost 50 per cent over the original controller. In addition, the fluctuation amplitude was drastically reduced when compared to the periodically forced flow as well as when compared to the unforced flow. Scrutinizing the control signal, it was observed that the controller introduces two harmonic frequencies into the flow, the lower of which was approximately $F_f \simeq 720\text{Hz}$. Interestingly, the control amplitude did not decline as the controller became effective, as initially anticipated. In contrast, the amplitude seemed to stabilize at $A/U_\infty \simeq 0.04$, which was larger than for the controller obtained directly from the ROM.

The results from this closed loop simulation supported the idea that excitation of frequencies that are unstable further upstream (closer to the step) has a much larger effect on the OPD, even if the aperture is located downstream, than forcing at a frequency that is commensurate with the

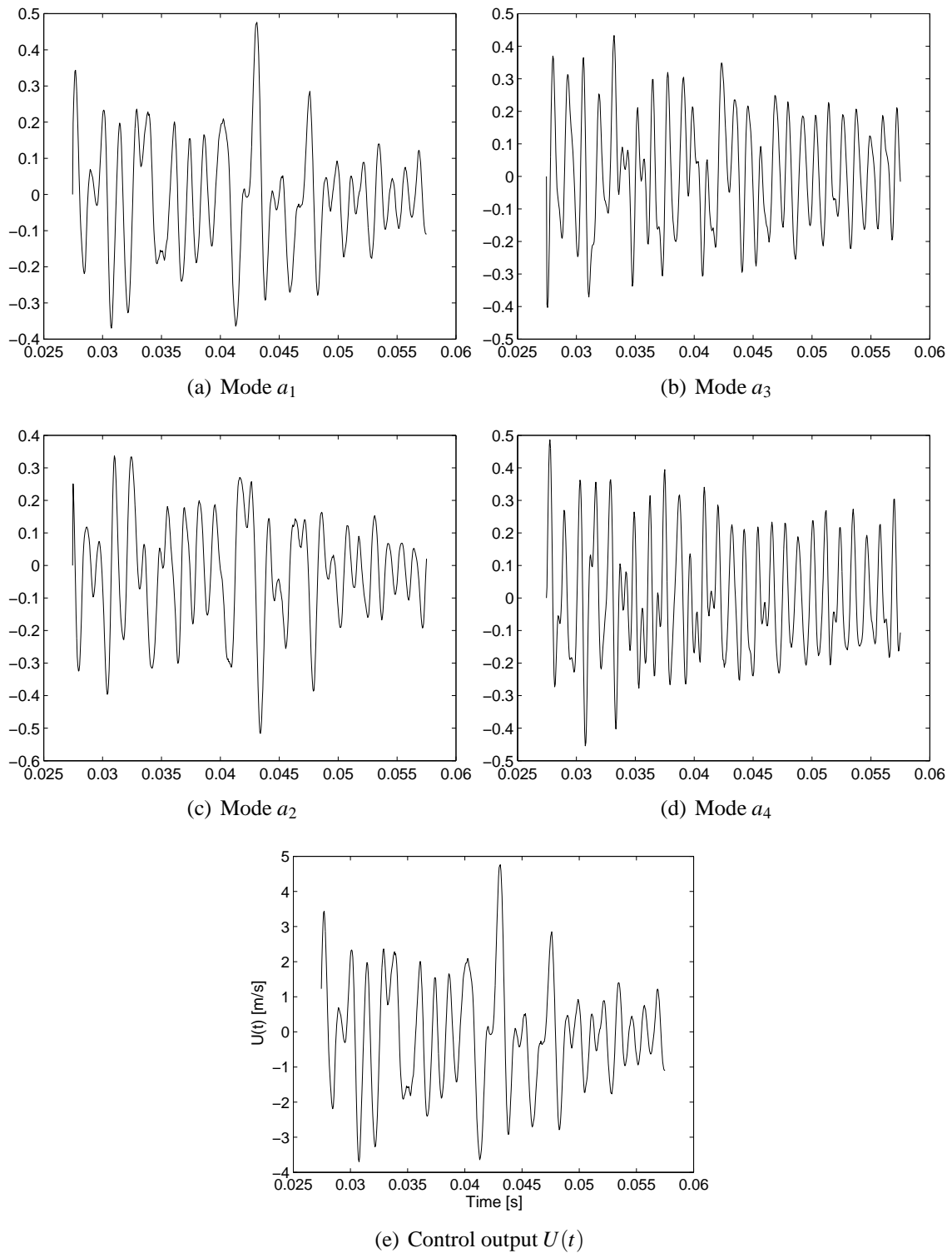


Figure 51: Mode amplitudes and control output of CFD closed loop simulation.

naturally occurring frequency at the aperture location. It is conjectured that forcing at the higher frequency kept the flow more periodic, thus reducing the vortex pairing tendency, which created the largest structures and therefore the largest optical distortions. Interestingly, open loop forcing at these higher frequencies did not show this level of performance, which was attributed to phase and frequency differences between flow states and forcing input. Only with feedback control was it possible to react to these differences in the adaptive manner necessary to reduce the density fluctuations in the shear layer.

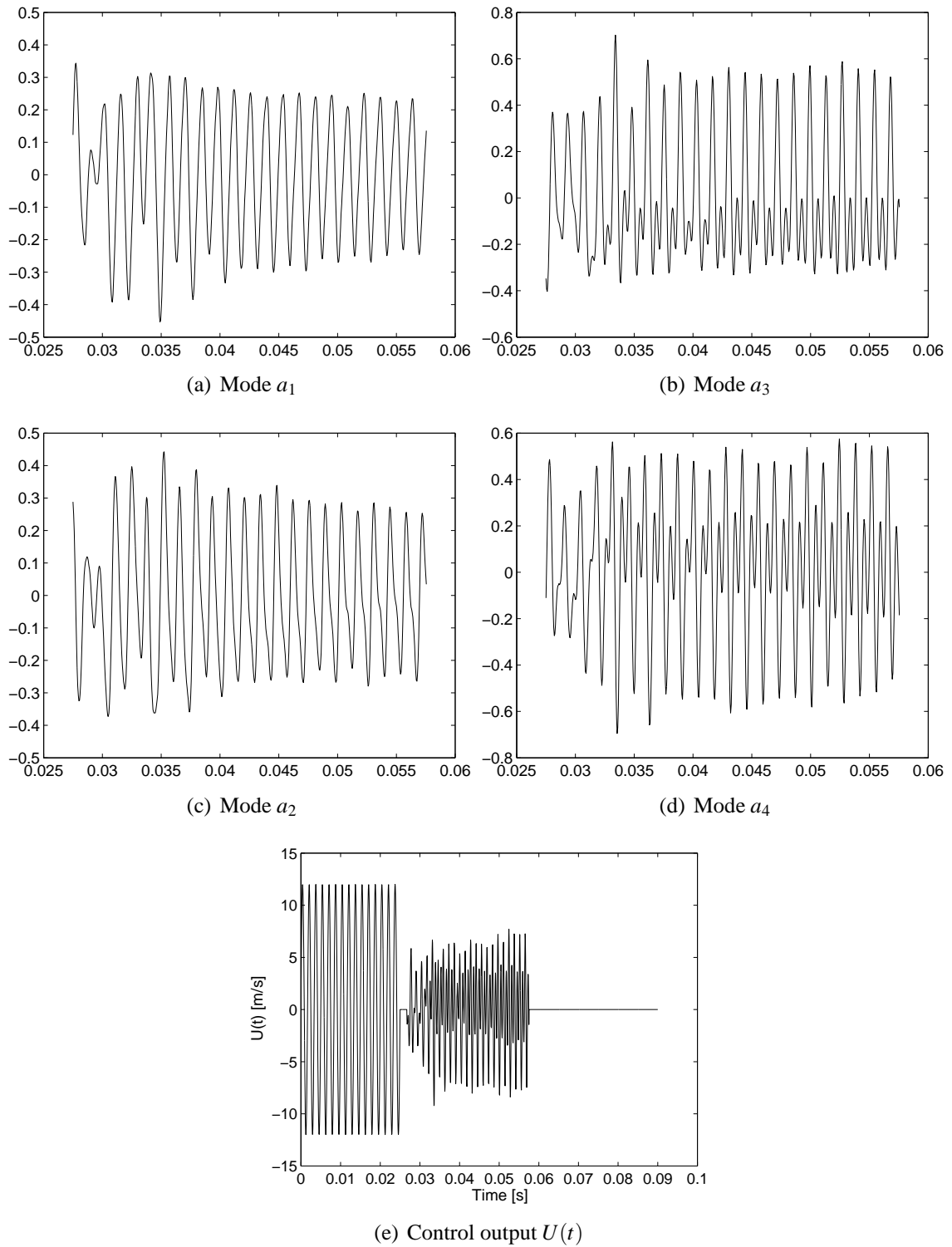


Figure 52: Mode amplitudes and control output of CFD closed loop simulation. The control output is shown for the complete simulation, periodic forcing for $t < 0.025$ s, feedback control for $0.025\text{s} < t < 0.06\text{s}$, and unforced for $t > 0.06\text{s}$.

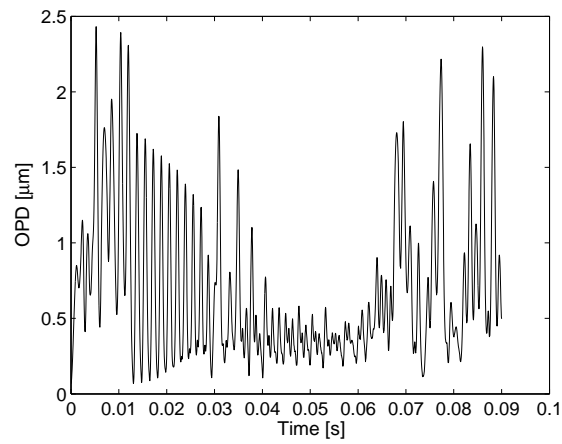


Figure 53: OPD calculation of closed loop CFD simulation with adjusted controller. Periodic forcing for $0s < t < 0.025s$, closed loop simulation for $0.025 < t < 0.06s$, and unforced for $t > 0.06s$. Reduction of OPD on the order of 30% of the OPD is seen.

5.4 Axisymmetric Bluff Body

5.4.1 Overview

Classical control theory is very limited when dealing with high-dimensional, extremely non-linear systems such as flow fields. Flow fields are governed by the Navier Stokes equations, Eq 74, a set of second order, non-linear partial differential equations. New techniques need to be established to make use of current control theories, while also allowing for a reasonable design process for linear, non-linear, or adaptive control for complex flow fields.

$$\rho \left(\frac{\partial \mathbf{u}}{\partial t} + \mathbf{u} \cdot \nabla \mathbf{u} \right) = -\nabla p + \nabla \cdot \mathbf{T} + \mathbf{f}, \quad (74)$$

The synopsis of active feedback flow control is to use a fluidic actuator on an aerodynamics body which is able to perturb the flow away from the original state and typically cause some type of desired response, for example increased lift coefficient, regulation of undersized loads, drag reduction, optical effects, vortex positioning, etc. Sensors on the body measure the flow state which is then translated into an actuation input through some control algorithm. This is shown by an example to a forebody at high angle of attack in Figure 54. The challenges associated with active feedback flow control are actuator placement, sensor placement and model/control algorithm design.

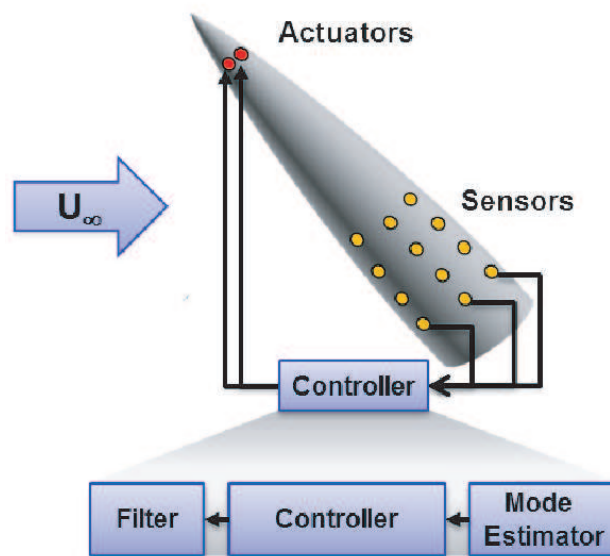


Figure 54: Flow control approach used for design and implementation of reduced order model based control

Figure 55 shows the approach adopted by the USAFA flow control research group. This framework is a systematic road map to developing a reduced order model, control algorithm, and optimal sensor placement for non-linear fluid dynamic systems. The ultimate goal of flow control research is to develop a robust model and control algorithm for a specific flow field to provide that as a

deliverable to the customer. The secondary goal of this flow control research is to gain physical insight into the fluid dynamics through closing the loop.

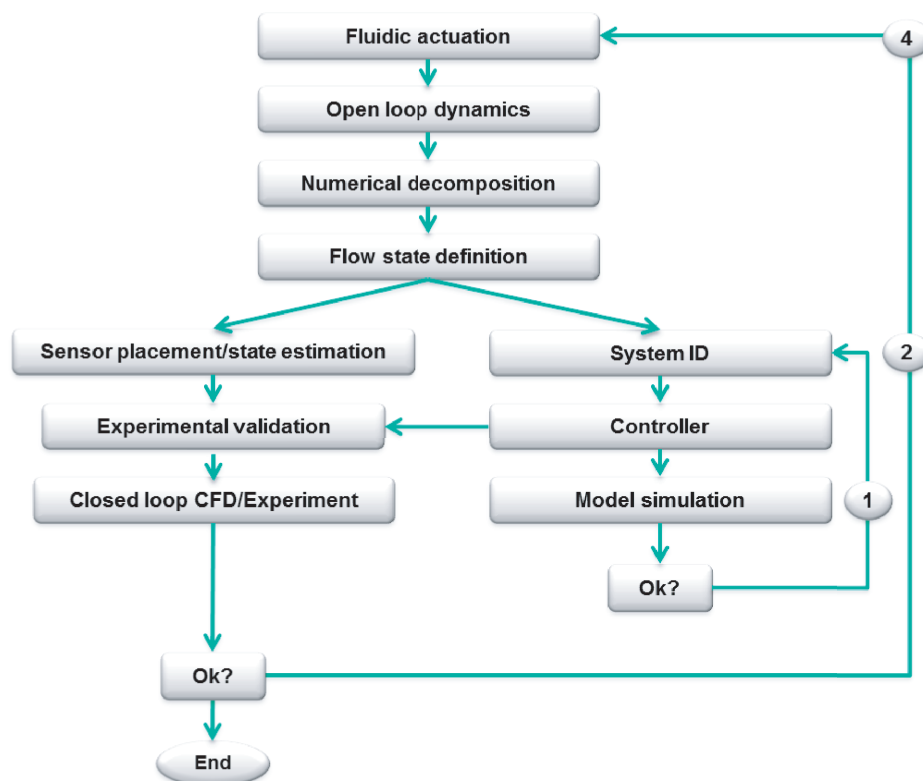


Figure 55: Flow control approach used for design and implementation of reduced order model based control

In the past it has been seen that the more insight and understanding of the fluidic mechanisms at play increase the fidelity of the reduced order model and performance of the control algorithm. For instance while closing the loop on the backward facing step, the closed loop dynamics showed that exciting the Kelvin Helmholtz structures in a certain location actually caused them to dissipate just afterwards. Thus, the optical aberrations were able to reduced over an aperture.

The approach begins with developing a fluidic actuator. Types of actuators consist of SDBD plasma, blowing and suction ports, synthetic jets, flow effectors, speakers, etc. Placement of actuators and number of actuators is typically chosen by rules of thumb from fluid dynamics. This is a suboptimal approach. For future success of feedback flow control, an autonomous method needs to be determined for actuator placement and design. This program will evaluate different technical solutions to this issue on the forebody flow control problem.

Once the fluidic actuator is in place either in CFD or experiments, open loop dynamics are acquired through various forms of input. Typically, step, impulse, ramp, and periodic inputs are used to quantify the system dynamics. As shown in previous applications of feedback flow control, these open loop dynamics are a crucial step in understanding the flow field. The actuator to fluidic response, i.e. the controllability of the fluidic system, is a critical relationship which is essential. For unsteady flow fields, the state trajectories from un-actuated to actuated states and vice versa is non-unique and highly dependent upon the initial state of the flow. This necessitates an optimal

selection of open-loop forcing which pseudo-randomly captures each state trajectory. This information will then provide for the compilation of a flow state database, which is essential for the development of a reduced order model which accurately represents the unforced, open-loop, and transient states near the desired controlled state. While these questions are best answered using CFD simulations because of the detailed data available, it is impossible to interrogate the whole parameter space this way. Experimental investigations are also necessary to provide the crucial survey of the parameter space to highlight regions of particular interest.

Once the open loop database is formulated, numerical decomposition techniques are used to extract pertinent dynamics. Specifically these decompositions decouple spatial and temporal modes in an optimal fashion. For the development of Reduced Order Models (ROMs) of the flow field, a software suite developed in the US Air Force Department of Aeronautics by the researcher will be readily available and applied to new problems. The data analysis part of the software suite consists of many tools such as: proper orthogonal decomposition (POD), double POD, balanced POD, dynamic modal decomposition (also referred to as Koopman analysis) and wavelet decompositions.

Each decomposition has unique advantages and disadvantages while the overarching goal is the same - to extract the dynamical behavior of large scale, coherent structures in the flow while decoupling spatial and temporal information. Extracting the desired or dominant dynamics of a fluid field is a highly debated topic. For instance POD defines the dynamics through largest energetic modes; BPOD defines the dynamical modes as a set which optimizes the observability and controllability grammians; DPOD emphasizes an energetic mode set coupled with shift or perturbation modes to the dominant modes due to actuated and un-actuated transients, and finally the Koopman analysis extracts spatial growth and decay rates (globally unstable and stable modes) as well as spatial frequencies (marginally stable modes). Each of these tools, while vastly different mathematical procedures produce the same result, decoupled spatial and temporal information. These decomposition techniques are commonly understood for unsteady flow fields, but the extension and application to deformable bodies in computational simulation or experimental testing has never been attempted. It is the intent of this research program to find a suitable strategy or combination of strategies to extract the dynamics of the fluid, structure, and fluidic actuation interaction.

Once an understanding of the underlying physics of fluid structure interactions is produced, a proper dynamic reduced order model can be developed. With this accurate system model the optimal type and distribution of actuators and surface sensors can be determined and implemented in both the simulations and experiments. During previous research projects, the flow control group at USAFA has found that the *low-dimensional modeling approach* is the most beneficial when it comes to realizing a structured model-based closed-loop strategy for flow control. Assuming a suitable mode set is determined from the previous section which represents the unforced, open-loop, and transient states, the associated temporal dynamics need to be modeled.

A widely accepted approach to model experimental and computational periodic flows is the Galerkin Method. A Galerkin projection is a method for obtaining approximations to a high dimensional dynamical system by projecting the underlying dynamics onto a reduced order subspace. In the application to fluid dynamics, the Navier Stokes equations are projected onto a subspace which is spanned by an orthogonal basis which represents a majority of the system dynamics typically obtained by POD. The resulting equations are a set of non-linear ODE's in the form of,

$$\dot{x}_f = f_0 + Lx_f(t) + Q(x_f(t) \otimes x_f(t)), \quad (75)$$

where the linear term is representative of the viscous term in the Navier Stokes and the quadratic

term is representative of the convective and pressure terms in the Navier Stokes. In some instances it is beneficial to also add a higher order cubic term to account for mean flow perturbations and experimental noise. An extension of the Galerkin Method is the Discontinuous Galerkin Method which may be essential for producing a stable discretization of the convective operator over unstructured, deformable meshes.

Previously, this research investigated wavelet basis networks (WNARX) to demonstrate the full capability of identifying complex flow response for a range of open loop parameters. The WNARX represents a dynamic model which can simulate off design flow cases, serve as reference signal, and ultimately predict closed loop behavior for control design. The WNARX model uses the same network architecture as a neural network; the only difference is radial basis functions are used as each neuron's transfer function. This is shown by, $\Psi(t)_{u,s} = \Psi\left(\frac{t-u}{s}\right)$, where u is the translation of the wavelet, s is the dilation, and Ψ is referred to as the mother wavelet, which is a radial basis function in this case. WNARX models are much better suited for identifying the frequency rich dynamics of complex, turbulent flow fields. The overall WNARX model is given by,

$$\hat{f}(t) = \sum_{i=1}^N w_i \Psi(s_i(t - u_i)) + c^T t + f_0 \quad (76)$$

where w_i are the weights, N is the number of wavelet functions, c^T represent the linear connections, and f_0 is the bias. This proposal will use this new system identification method to formulate an extremely low dimensional model based from CFD simulations and POD/DPOD decompositions to accurately predict closed loop dynamics of a given flow field. This model is then used to perform feedback simulations to condition control algorithms which can then be applied directly to CFD simulations and experiments.

Once this model (either Galerkin model, or WNARX) is validated over unforced and open-loop parameter space, it will serve as the basis for the control strategy development. Typical control approaches to non-linear systems can be used. For instance direct adaptive control, sliding mode control, or model predictive control may be used to achieve stable, robust reference tracking ability. Previous research supports that adaptive control adequately handles model uncertainties between model and CFD closed loop simulations. This research project aims at evaluating the performance and stability criterion of these three control approaches. As for differences between CFD simulations and experimental tests, the actuation dynamics and sensor dynamics will be unique to each environment, but the underlying control theory, flow/structure state definition, and estimation algorithms will remain constant. This will allow for model and estimation development to be based upon both numerical and experimental data. In a sense the control will be modularized by the actuation/sensing dynamics which will provide matching CFD and experimental results in closed loop simulation/experimentation.

5.4.2 Open Loop Dynamics Experiment

As presented in Farnsworth et al. [2012], at the current operating conditions, the system is shown to be proportional at an incidence of 50° . Figure 56 shows a schematic of the responsiveness of the asymmetric state (measured as the resulting side force) to plasma actuation. The positive x-axis represents the port forcing strength and the negative x-axis represents the starboard forcing strength; the zero location is the unforced state. The unforced state of the asymmetric vortex configuration varies based on geometry disturbances, flow conditions, misalignments, flow imperfections etc. Around this initial state is a dead zone in the actuator dynamics; that is, the actuation voltage must exceed a certain limit before plasma formation takes place. Above and below this region a linear response in asymmetric vortex state was found. At large enough forcing magnitudes the vortex system does saturate in the fully left or right asymmetric vortex state.

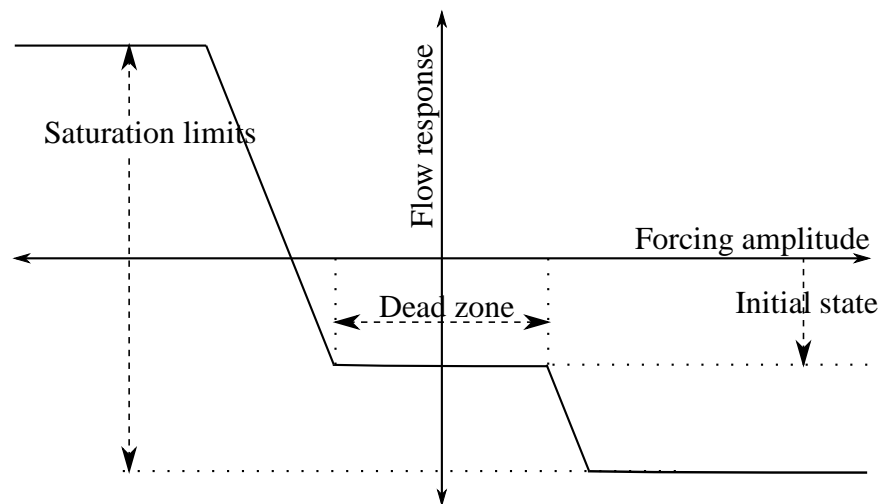


Figure 56: Representation of the forcing characteristics of the asymmetric vortex state due to plasma actuation.

Figure 56 is experimentally verified by side force and sectional pressure measurements as depicted in Figure 57. The side force, C_y and sectional pressure coefficient, ΔC_p , at $x/D = 3$ vary analogously with varying port/starboard plasma voltage which supports that time resolved pressure measurements do accurately correlate with integrated force measurements. As Figure 57 also shows, the system responds nearly proportionally, although non-linear effects are apparent. For instance, the dead zone in the actuation voltage range from $-5kV \leq V \leq 5kV$ does exist; this is, primarily due to the fact that plasma has not formed at these smaller voltage potentials. Also, a hysteresis is definitely observed, that is the path along a positive voltage gradient, $\frac{dV}{dt} > 0$, is different from the path along a negative voltage gradient, $\frac{dV}{dt} < 0$, in both time accurate (red/blue lines) and integrated measurements (black lines). Finally, a larger gradient, $\frac{d\Delta C_p}{dV}$ is seen near the symmetric vortex location ($C_y = \Delta C_p = 0$), supporting the fact that a small amount of bistability does exist at this flow condition.

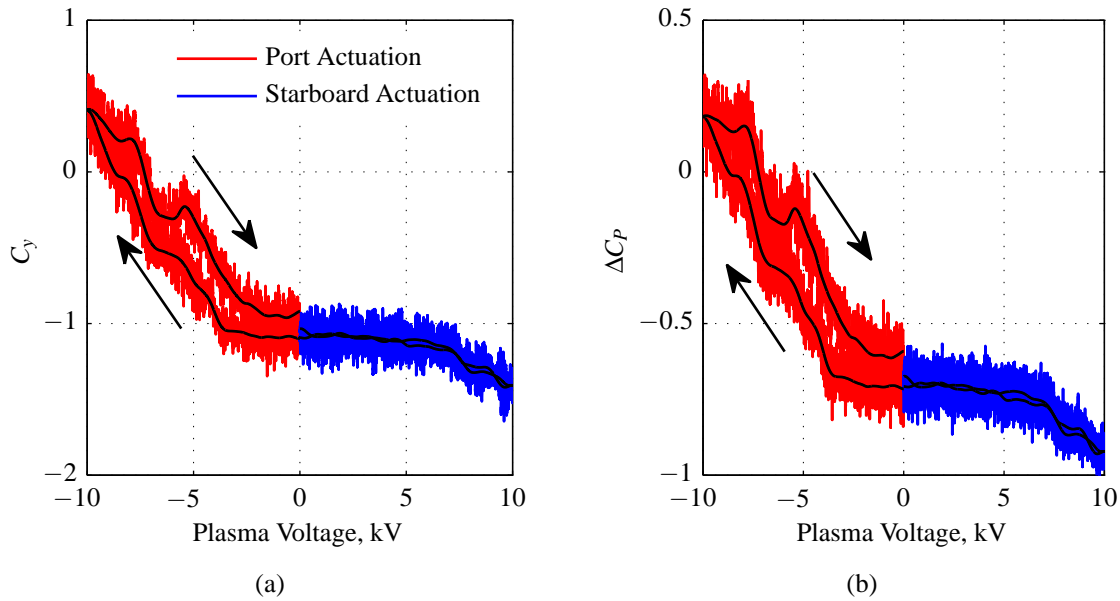


Figure 57: (a) Side force coefficient and (b) differential pressure coefficient at $x/D = 3$ versus the plasma actuator voltage during the ramp modulation.

The system response in Figure 57 is well modeled by a linear system with slight non-linearities present.

5.4.2.1 Step Response The response of the asymmetric vortex state due to a plasma actuation step input is used to develop a linear time invariant model. The step response test campaign consisted of a modulated square wave at a frequency of 1 Hz for a total of 20 periods. The data was then phase averaged over a test duration of 20 seconds to reduce measurement noise. The amplitude of the step was at maximum operational voltage of 12 kV before the amplifier began displaying non-linear effects. Figure 58 shows the normalized response to the step input at initial transient times and Figure 59 for the ending transient times.

The overall time delay consists of the convective time delay for the disturbance to reach the sensor location, lag time for the fluid to respond, and transition time to achieve 90% of the steady-state value. To decouple each of these sources of delay, the convective time delay is defined as the time from which the step begins to the time at which a 10% change in the unforced steady-state value is observed. The rise time is defined as the time from a 10% change in the unforced steady state value to the time at which 90% of the forced steady-state value was achieved. The time responses are then normalized by the flow through time, τ , which is defined as,

$$\tau = \frac{L_{cone}}{U_{\infty}}, \quad (77)$$

and was measured to be approximately 13 ms at the current operating conditions. These times are summarized for the rising and falling transients in Table 7. The lag time or presence of non-minimum phase are difficult issues to decouple in the dynamics so further analysis techniques are necessary.

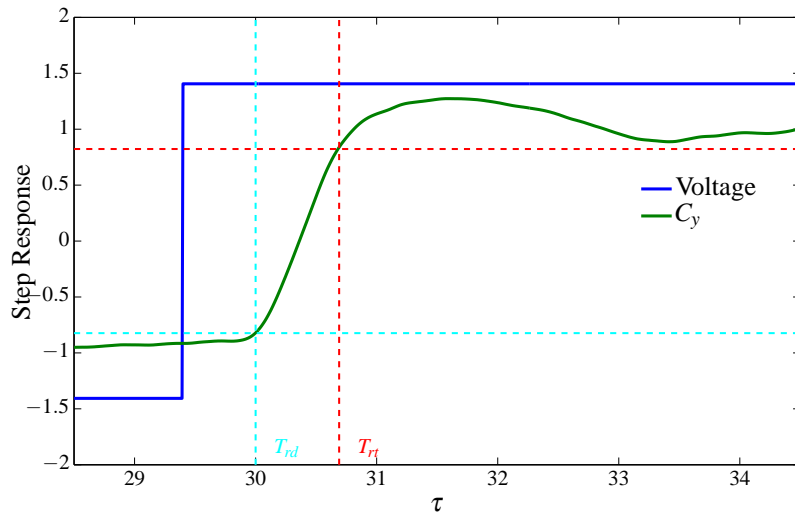


Figure 58: Initial transient of the vortex state due to step input. Linear combination of pressure measurements at $x/D = 2$ and $x/D = 3$ to estimate the side force shown in green. Blue shows the step change of the actuation input in kV. Also, the convective delay time, T_{rd} , is shown in cyan and the transition/rise time, T_{rt} , is shown in red.

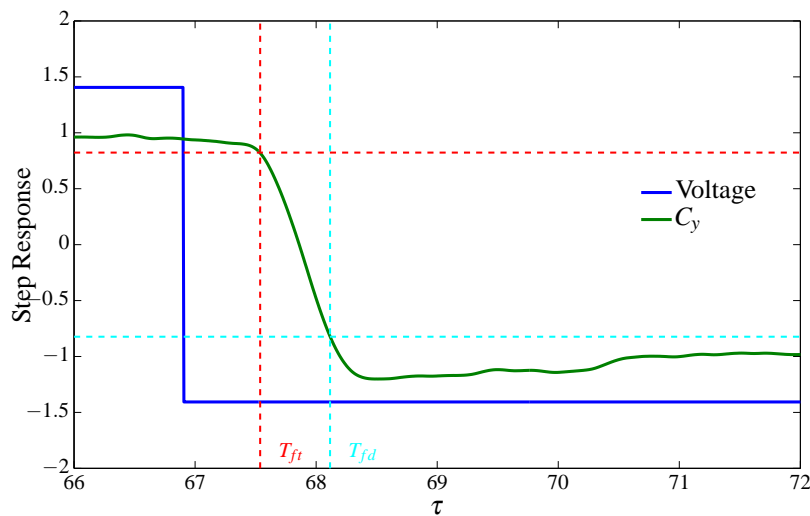


Figure 59: Ending transient of the vortex state due to step input. Linear combination of pressure measurements at $x/D = 2$ and $x/D = 3$ to estimate the side force shown in green. Blue shows the step change of the actuation input in kV. Also, the convective delay time, T_{fd} , is shown in cyan and the transition/rise time, T_{ft} , is shown in red.

Table 7: Rise and fall time summary

	Initial Transient (Port - Starboard) Time [t^*]				Ending Transient (Starboard-Port) Time [t^*]			
	Delay Time	Rise Time	Total	% Overshoot	Delay Time	Rise Time	Total	% Overshoot
\hat{C}_y	0.6375	0.69	1.3275	18.5 %	0.6070	0.57	1.177	24.4%

As shown in Table 7, the convective times for a port to starboard or vice versa are very consistent, as expected. The rise or transition time from starboard to port is a bit faster than the transition time from port to starboard. This is, arguably, because the initial asymmetric state prefers the port side due to geometry imperfections, flow misalignments, etc.; thus the flow prefers transition back to the port state and induces a restoring force, reducing transient time and also causing a larger overshoot of the steady state value. Nonetheless, the dynamics of the asymmetric vortex problem as shown by the step response are very well represented by a linear time invariant system.

5.4.2.2 Sinusoidal Response To determine the frequency response of the system dynamics, sinusoidal forcing is used on the port actuator and the system response is observed by the linear combination of all of pressure measurements as given by \hat{C}_y . The actuation voltage is modulated by an offset sinusoid, by the equation,

$$A(t) = V_{max}(\sin(2\pi\omega t) + 0.5).$$

The test durations consisted of 30 seconds with a sampling frequency of 10 kHz. An example of forcing at a frequency of 20 Hz is shown in Figure 60. The input-output signals are shown as well as the frequency spectrum. Figure 60b shows a large peak at the forcing frequency showing the fluidic receptivity to the forcing. A frequency sweep was conducted over a wide frequency range to determine the cutoff frequency as well as the magnitude and phase of the system.

The natural rise time of the fluidic response is approximately $1.1t^* \rightarrow 1.6t^*$, depending upon port to starboard actuation or vice versa, due to a unit step input as shown in section Table 7. The natural frequency is approximately 50 Hz. This suggests that a pole exists near this location. Because of this observation, the modulation frequency was chosen at discrete locations over the range of $0.1\text{Hz} \leq \omega \leq 200\text{Hz}$, to determine magnitude, phase and cutoff frequency.

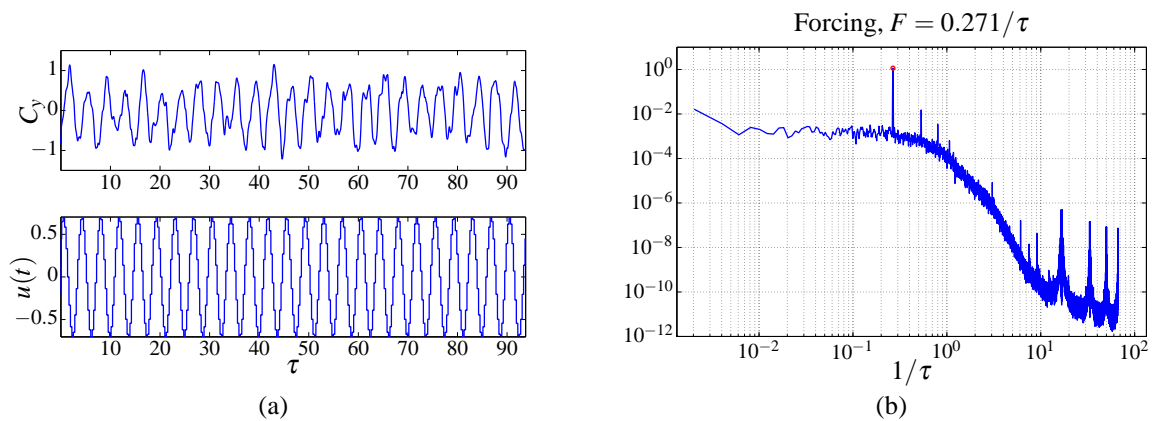


Figure 60: Pressure location $x/D = 2$ (a) Time domain forcing and response data for Frequency = 20 Hz (b) Time domain forcing and response data for Frequency = 20 Hz.

For all of the forcing frequencies the data is summarized in Figure 88 where the experimental data is plotted in red. From this frequency response information the cutoff frequency can be estimated by a -3 dB attenuation point. This is computed to be approximately 50 Hz and corresponds to a 80 degree phase lag.

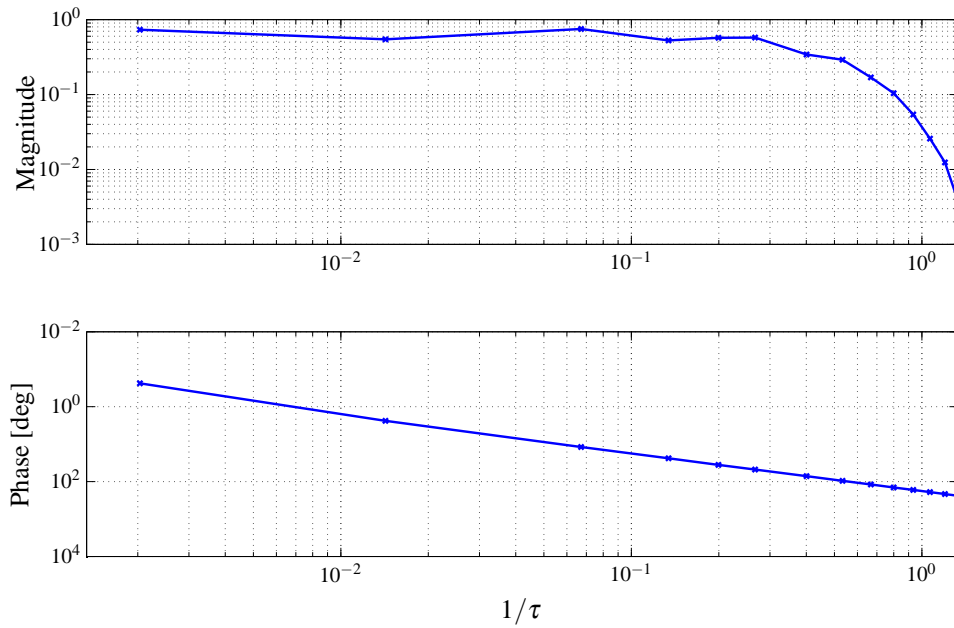


Figure 61: Experimental frequency and phase response information for sinusoidal forcing campaign

5.4.2.3 Impulse Response The impulse response of the asymmetric vortex state was also measured. For these open-loop tests the duty cycle was varied for a square modulation wave at a frequency of 10Hz over a range of 1% to 20%. The experimental measurements are shown below in Figure 89 for the different duty cycles. The initial flow state was shifted to $C_y = 0$, i.e. the symmetric state for modeling purposes. All of the impulses were initiated at $t = 0$, so that the flow response is aligned for each duty cycle. These measurements were phase averaged over a 100 total cycles. The results in Figure 89 are well depicted by a linear system. As the duty cycle increases beyond 10% an amount of undershoot is seen by the vortex dynamics. This data set is used completely as validation for the model formulation and model selection technique.

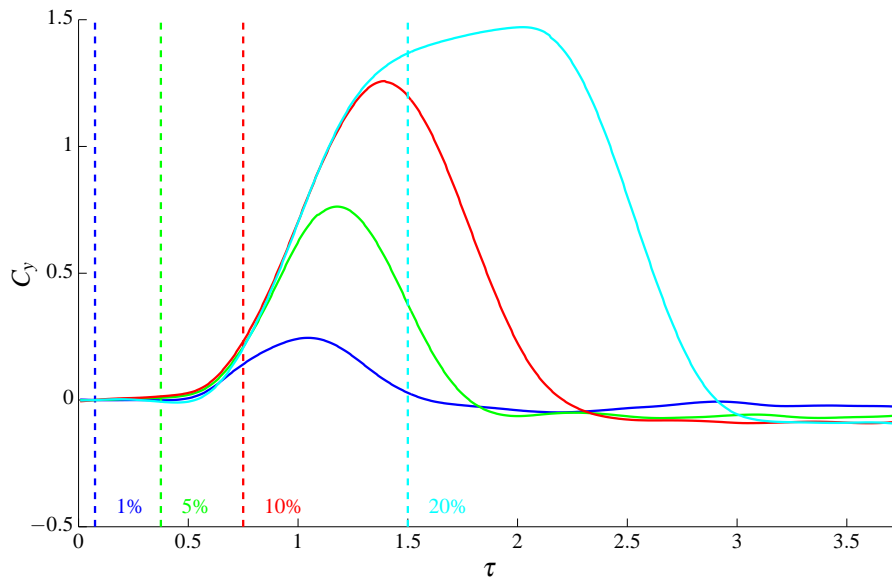


Figure 62: Experimental measurements of the impulse response with varying duty cycle of the pulse width at a maximum voltage of 1.4 kV. This data serves purely as validation data for model development in subsequent sections.

5.4.3 Open Loop Dynamics Simulations

As presented in Farnsworth et al. [2012], at the current operating conditions, the system is shown to be proportional at an incidence of 50° . Figure 63 shows a schematic of the responsiveness of the asymmetric state (measured as the resulting side force) to plasma actuation. The positive x-axis represents the port forcing strength and the negative x-axis represents the starboard forcing strength; the zero location is the unforced state. The unforced state of the asymmetric vortex configuration varies based on geometry disturbances, flow conditions, misalignments, flow imperfections etc. Around this initial state is a dead zone in the actuator dynamics; that is, the actuation voltage must exceed a certain limit before plasma formation takes place. Above and below this region a linear response in asymmetric vortex state was found. At large enough forcing magnitudes the vortex system does saturate in the fully left or right asymmetric vortex state.

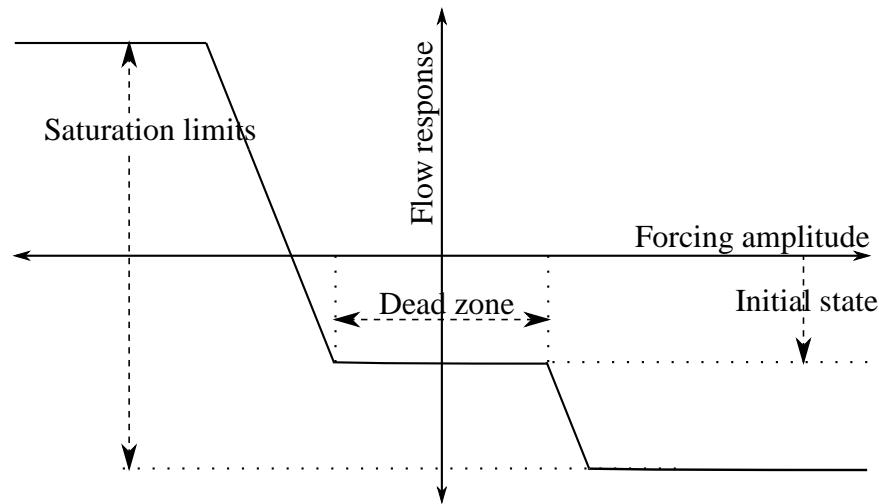


Figure 63: Representation of the forcing characteristics of the asymmetric vortex state due to plasma actuation.

Figure 63 is verified in CFD simulations by side force as depicted in Figure 64. The side force, C_y varies proportionally with varying port/starboard plasma voltage. As Figure 64 also shows, the system responds nearly proportionally, although non-linear effects are apparent. For instance, the dead zone in the actuation strength from $-0.025g/s \leq \dot{m} \leq 0.025g/s$ does exist. Saturation regions are also seen for $\dot{m} > 0.75g/s$.

The system response in Figure 64 is well modeled by a linear system with slight non-linearities present.

5.4.3.1 Step Response The response of the asymmetric vortex state due to a plasma actuation step input is used to develop a linear time invariant model. The step response test campaign consisted of a modulated square wave at a frequency of 1 Hz for a total of 20 periods. The data was then phase averaged over a test duration of 20 seconds to reduce measurement noise. The amplitude of the step was at maximum operational voltage of 12 kV before the amplifier began displaying non-linear effects. Figure 65 shows the normalized response to the step input at initial transient times and Figure 66 for the ending transient times.

The overall time delay consists of the convective time delay for the disturbance to reach the sensor location, lag time for the fluid to respond, and transition time to achieve 90% of the steady-state value. To decouple each of these sources of delay, the convective time delay is defined as the time from which the step begins to the time at which a 10% change in the unforced steady-state value is observed. The rise time is defined as the time from a 10% change in the unforced steady state value to the time at which 90% of the forced steady-state value was achieved. The time responses are then normalized by the flow through time, τ , which is defined as,

$$\tau = \frac{L_{cone}}{U_{\infty}}, \quad (78)$$

and was measured to be approximately 13 ms at the current operating conditions. These times are summarized for the rising and falling transients in Table 8. The lag time or presence of non-

minimum phase are difficult issues to decouple in the dynamics so further analysis techniques are necessary.

Table 8: Rise time summary

Initial Transient (Port - Starboard) Time [τ]				
	Delay Time	Rise Time	Total	% Overshoot
\hat{C}_y	0.62	0.39	1.01	15.5 %

When comparing CFD transient times to experimental transient times, very good agreement exists, see Table 8 and Table 7. The simulations are slightly faster than the experiments (30%). This is mainly due to transient dynamics of the experimental circuitry which is non-existent in the CFD simulation. Nonetheless, the dynamics of the asymmetric vortex problem as shown by the step response are very well represented by a linear time invariant system.

5.4.4 Impulse Response

The impulse response of the asymmetric vortex state was also simulated. For these open-loop tests the duty cycle was varied for a square modulation wave at a frequency of 10Hz over a range of 1% to 10%. The simulation results are shown below in Figure 67 for the different duty cycles. The initial flow state was shifted to $C_y = 0$, i.e. the symmetric state for modeling purposes. All of the impulses were initiated at $t = 0$, so that the flow response is aligned for each duty cycle. The results in Figure 67 are well depicted by a linear system. This data set is used completely as validation for the model formulation and model selection technique.

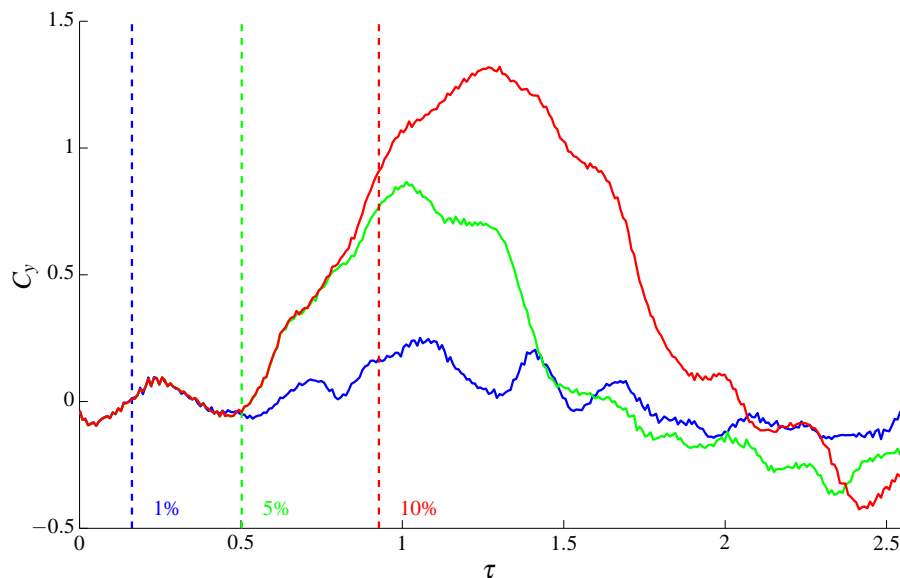
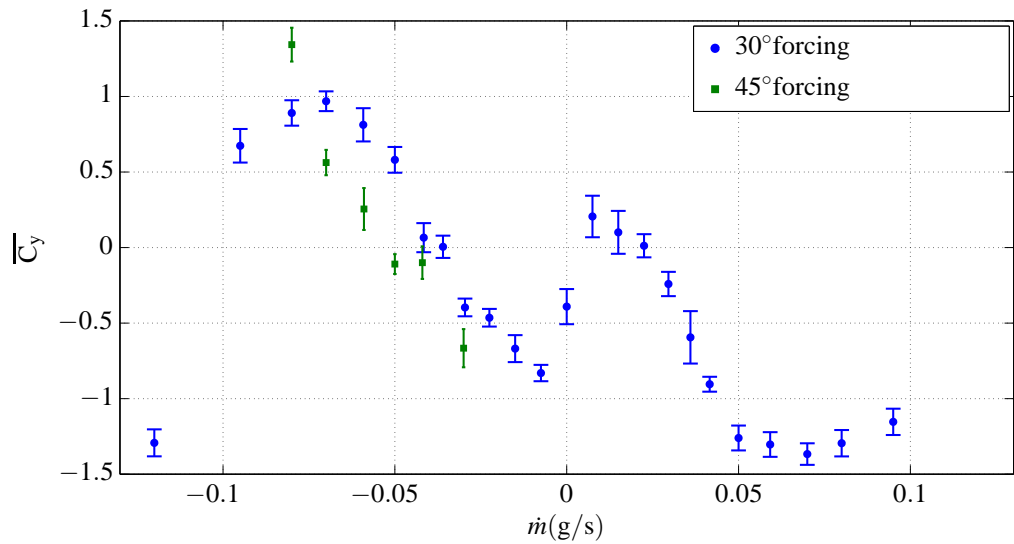
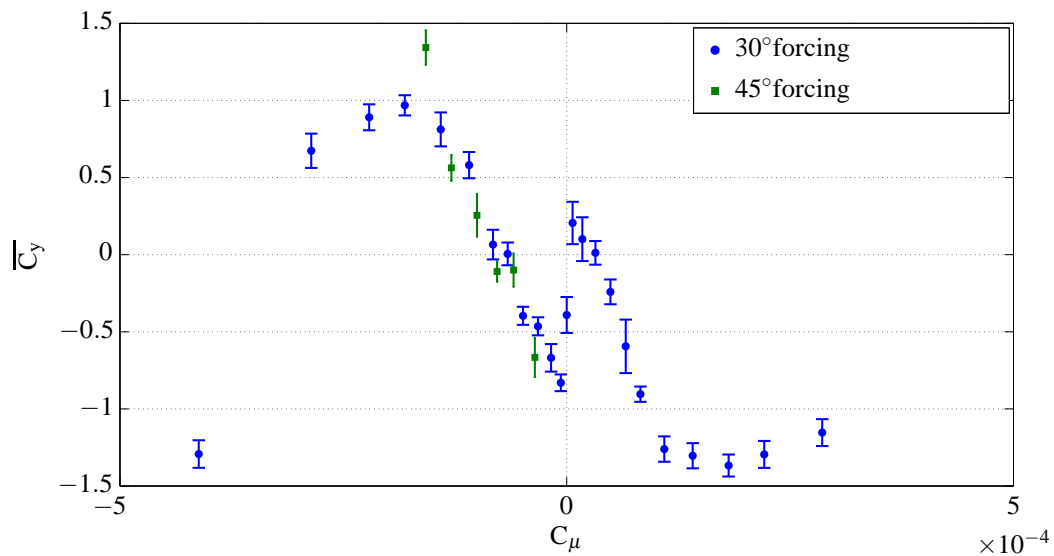


Figure 67: Impulse response of the CFD simulation varying duty cycle of the pulse width at a unity magnitude of C_μ . This data serves purely as validation data for model development in subsequent sections.



(a) Mass flow rate



(b) Momentum Coefficient

Figure 64: Average side force coefficient for different forcing parameters. Port forcing corresponds to a negative x-values while starboard forcing corresponds to a positive x-values.

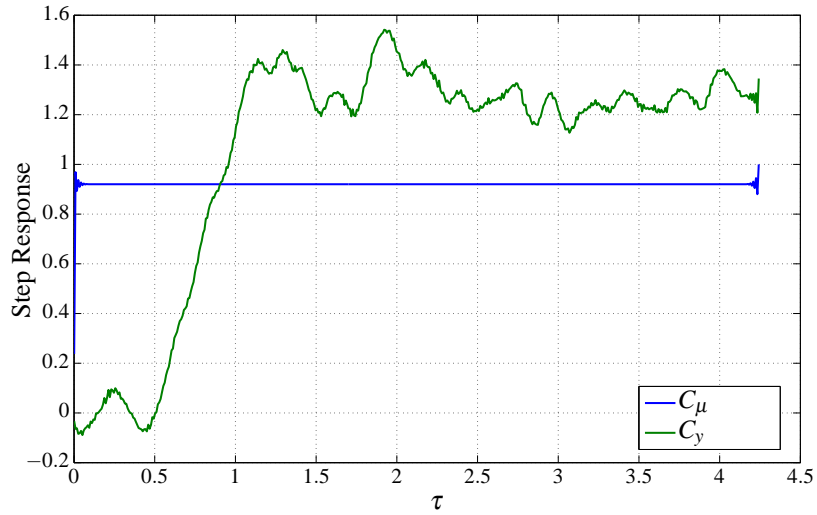


Figure 65: Side force in green shows the response due to a step input in C_μ in blue.

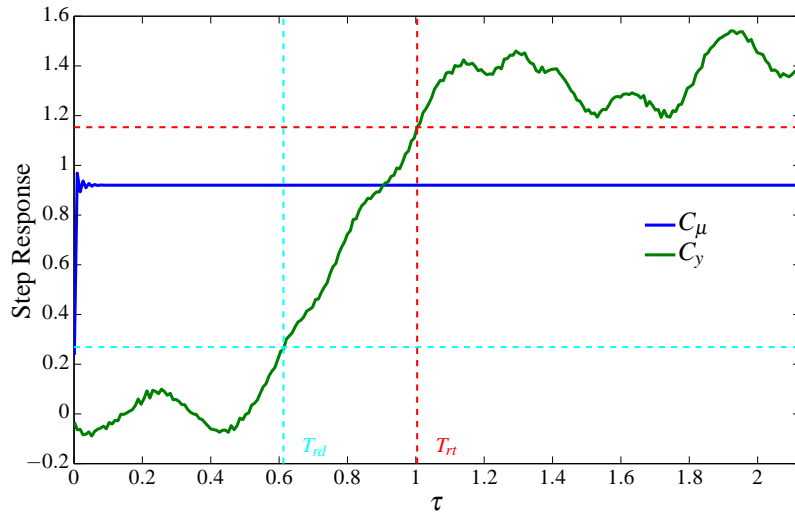


Figure 66: Initial transient of the vortex state due to step input. Side force in green shows the response due to a step input in C_μ in blue. Also, the convective delay time, T_{fd} , is shown in cyan and the transition/rise time, T_{rt} , is shown in red.

5.4.5 Numerical decomposition and flow state definition

To further investigate the flow field around a von Kármán tangent ogive and develop a Reduced-Order-Model (ROM) for feedback flow-control, unsteady numerical investigations were undertaken. The simulations are performed using Cobalt, an unstructured finite-volume code developed for the solution of the compressible Navier-Stokes equations. The basic algorithm is described in Strang et al., [1999] although substantial improvements have been made since then. The numerical method is a cell-centered finite volume approach applicable to arbitrary cell topologies (e.g, hexahedra, prisms, tetrahedra). The spatial operator uses a Riemann solver, least squares gradient calculation with QR factorization to provide second order accuracy in space. A point implicit method using analytic first-order inviscid and viscous Jacobians is used for advancement of the discretized system. For time-accurate computations, a Newton sub-iteration scheme is employed, resulting in a method that is formally second order accurate in time. For parallel performance, Cobalt utilizes the domain decomposition library ParMETIS to provide optimal load balancing with a minimal interface between zones. [Karypis et al. [1997]]

5.4.5.1 Grid and Model Geometry The geometry considered in this investigation is a generic tangent ogive with fineness ratio $f_r = 3.5$ and a model base diameter of $D = 0.1$ m. At the base of the ogive, a 0.05 m long cylindrical section has been added such that the overall length of the model is 0.40 m. This model geometry was chosen to match an accompanying wind tunnel experiment. [Fagley et al. [2012a]] For reference, the center of the coordinate system is at the nose of the model. The positive x-direction extends along the body, the positive y-direction points in the starboard direction, and the positive z-direction is up, normal to the body. For the simulations, all the reference conditions are set to standard sea level, with an inflow Mach number of $M=0.1$; this results in a Reynolds number based on the base diameter of $Re = 220,000$.

The grid was generated using Simcenter/SolidMesh and had approximately 16M cells (Fig. 68). To avoid asymmetries in the flow field as a result of an asymmetric grid, the grid was generated around half the model and then mirrored; therefore, the grid is symmetric on the port and starboard sides of the model. Two patches to simulate the plasma actuators used in the accompanying experiment were added to the model at 90° from the model's meridian. The start of the boundary patch was placed 0.4 cm from the tip of the model and was 1 cm long. All model boundaries were always set to solid-wall, no-slip conditions except during the open-loop forcing investigations where one of the actuator boundary patch (either port or starboard) was switched to a moving wall boundary patch. In the open-loop simulations, the moving wall boundary patch prescribed a tangential velocity at the wall in the direction of the freestream. A spherical farfield boundary was placed 40 diameters away from the model to minimize the influence of pressure reflections. For all the calculations, the farfield used a modified Riemann condition and the time step was specified at $\Delta t = 0.0001$ s.

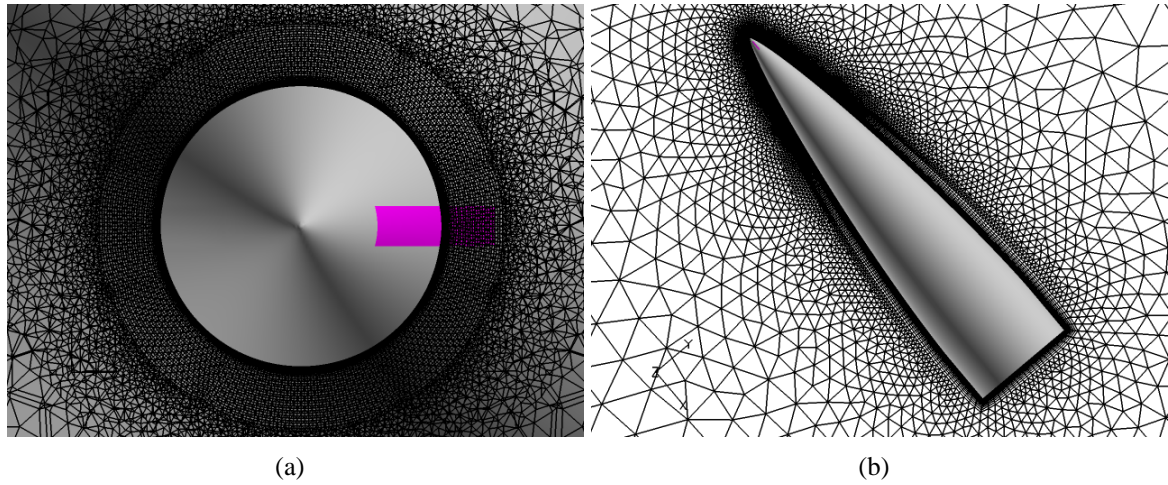


Figure 68: Ogive geometry and grid with simulated port actuator shown in purple: a) front view with grid shown at the center plane of the forcing patch, b) side view of the grid along the centerline of the model.

To extract the time-resolved simulation data around the ogive body, an array of Cobalt 'taps' was used. Figure 69 shows the tap grid used around the ogive model. The tap grid extended along the whole body, from $x/D = 0$ to $x/D = 4$ and 110° from the leeward meridian. The taps were non-uniformly spaced, such that a high spatial resolution is obtained near the body, especially near the tip of the model. In total, 37,625 taps were used to extract all the flow quantities during each time iteration.

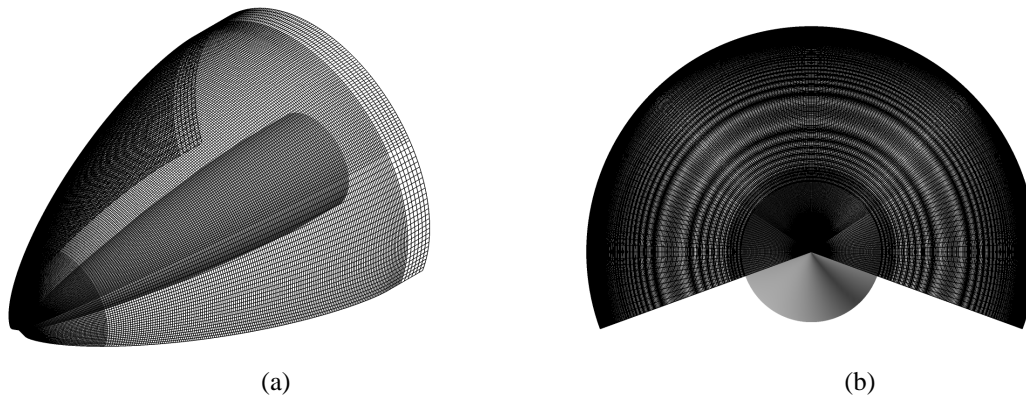


Figure 69: Ogive geometry with tap grid: a) isometric view and b) front view.

5.4.5.2 Proper Orthogonal Decomposition For data analysis, Proper Orthogonal Decomposition (POD) has been shown to be a very effective tool to characterize flow fields. Sirovich [1987], Berkooz et al. [1993] In POD, highly complex flow fields are decomposed into spatial modes with a corresponding time varying amplitude (or coefficients):

$$\varphi(x, y, t) = \sum_{k=1}^K a_k(t) \phi_k(x, y) \quad (79)$$

where ϕ is a flow quantity, $\phi_k(x, y)$ are the spatial modes, and $a_k(t)$ are the time coefficients. While this decomposition is well suited to time periodic flow fields, it faces problems for transient flows Siegel et al. [2005b] and potentially aperiodic flows. In these cases, POD is based on all the snapshots used to generate the modes, minimizing the overall error with the fewest number of modes possible. Therefore, transients or aperiodicity in the flowfield can be missed due to the small contribution made to the overall estimates of the spatial and temporal modes. Different additions to the basic POD procedure have been proposed, most notably the addition of a shift mode as introduced independently by Noack Noack et al. [2003] as well as Siegel et al. Siegel et al. [2003b]

5.4.5.3 Results Before investigating the effects of open-loop forcing on the side force generated from the asymmetric vortex state, unforced simulations were carried out where both the port and starboard forcing patches were set to solid-wall, no-slip boundary conditions. In this configuration, the model is geometrically perfect such that no disturbance exists to cause the leeward vortices to lock into an asymmetric state. Figure 70 shows the resultant side force on the model as a function of time. As shown, the side force coefficient, C_y , fluctuates between the port (negative C_y values) and starboard (positive C_y values) direction reaching magnitudes slightly greater than 0.5. As summarized by Bridges et al., Bridges [2006] if the root cause of the asymmetric vortex configuration is the result of a convective instability, numerical codes should not produce an asymmetric wake on geometrically perfect bodies. If they do, then the potential exist that the asymmetry is due to numerical issues and is not necessarily real; in other words, the right solution is obtained for the wrong reasons. Figure 70 shows that the geometrically perfect model produces an average side force of zero using the current numerical setup. To verify that the numerical code would produce an asymmetric wake when a geometrical disturbance was present, simulations were also run with a small bump (0.5 mm diameter pin, 0.5 mm tall) placed on the port side near the tip of the model. Figure 70 also shows the resultant side force on the model with this geometric disturbance present. As shown, the geometric disturbance causes the side force on the model to lock into one side (in the opposite direction of the disturbance) and the magnitude of the asymmetry increases. Therefore, at this Reynolds number, a disturbance on the port side causes the port side vortex to lift off the body, causing the side force in the starboard direction.

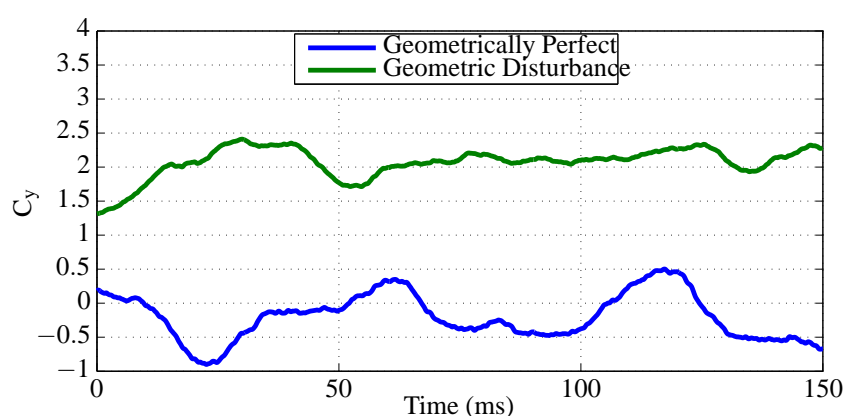


Figure 70: Comparison of the side force coefficient on a tangent ogive forebody with and without a geometric disturbance located near the tip of the model.

Following the unforced simulations, open-loop simulations which modeled the plasma actuator used in the experiments were performed. To simulate the plasma actuator, a moving wall boundary condition was implemented, where instead of setting the tangential velocity at the wall to zero (i.e. no slip), a fixed velocity is prescribed. Therefore, downstream of the moving wall patch, a wall jet is formed as the velocity at the wall diffuses into the rest of the boundary layer. The prescribed velocity of the moving wall boundary patch was changed throughout a series of simulations, ranging from 4 m/s up to 16 m/s (10 to 45 percent of freestream). While these velocities are much greater than those generated by the plasma actuators in the experiments, the resultant wall jets downstream of the actuator are similar. Lee et al. [2012]

Figure 71 shows the resultant side force on the model for a moving wall velocity of 12 m/s, where the actuation is switched from the starboard to the port side every 300 ms. As shown, there is a delay (≈ 100 ms) between the time actuation is turned on and the time when the side force fully switches sides and locks into its new value. From the simulations, it takes approximately 50 ms (five convective time scales Lanser and Meyn [1994]) before the side force begins to respond to the forcing input. The other 50 ms is the approximate time it takes for the vortices on the model to switch states. This is in contrast to experimental findings based on dynamic pressure transducers on the model which show that the model responds to forcing from the plasma actuator within one to two convective time scales. Farnsworth et al. [2012]

Based on the data shown in Fig. 71, the side on which forcing is applied causes the vortex on that side of the model to separate from the body and the side force is directed away from the side of actuation. This is the same trend observed with the geometric disturbance introduced on the model as well as experimental data ? for a similar Reynolds number range. This indicates that at this Reynolds number, instead of the plasma adding momentum to the flow to help keep the boundary layer attached, it is instead creating a disturbance causing the flow to separate. This is a different trend from Matsuno et al. Matsuno et al. [2009] who tested the use of DBD plasma actuators on a ogive model at a lower Reynolds numbers ($\approx 50,000$). During their tests, the plasma actuator caused the lifted vortex to attach to the body; this reattachment of the lifted vortex was attributed to the Coanda effect. At the lower Reynolds numbers tested, it is surmised that the strength of the wall jet created by the plasma relative to the freestream is much larger creating a Coanda type effect, while at the higher Reynolds numbers, the jet creates a disturbance causing the flow on that side to separate.

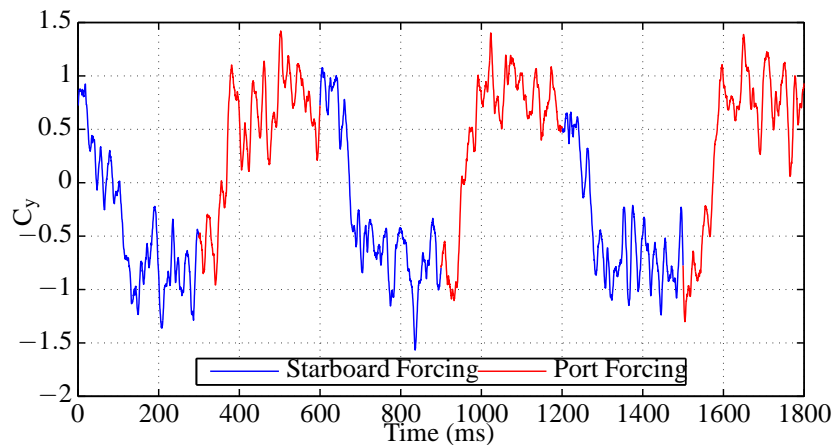


Figure 71: Open-loop side force coefficient on a tangent ogive body, switching between starboard and port forcing every 300 ms.

To illustrate the coherent vortical structures in the flowfield, Fig. 72 shows an isosurface of Q with a moving wall velocity of 12 m/s for the starboard actuator turned on. Jeong and Hussain [1995] As shown, at this Reynolds number, the asymmetry of the two primary vortices is small, even though the side force coefficient is approximately -1.0 at this instant. To help distinguish between the port and starboard vortices, Fig. 72 is colored by the x -vorticity. Looking at the side view of Fig. 72, smaller coherent structures can be seen feeding into the primary vortices, as the flow separates off the model forming a shear layer.

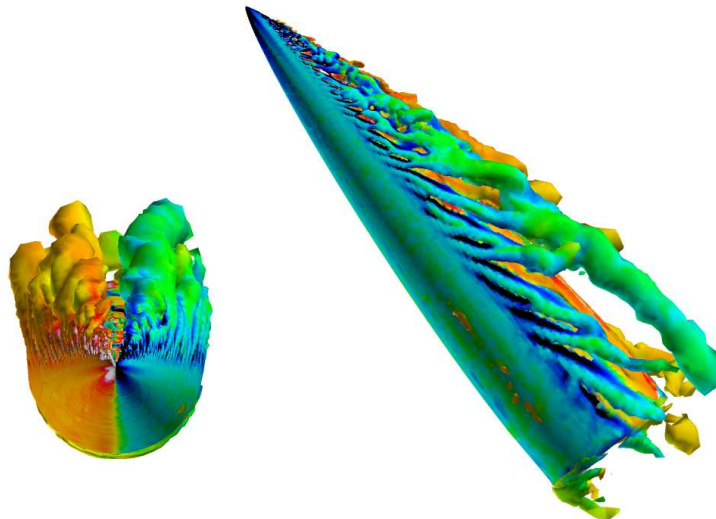


Figure 72: Isosurface of Q -criteria around the ogive model with starboard actuation turned on at 12 m/s.

To investigate the effect of changing the strength of the disturbance created by the forcing patches near the tip of the model, the moving wall velocity was varied from 4 m/s to 16 m/s in

4 m/s intervals. A high frequency component to the side force can be seen in Fig. 71 and was observed for the other moving wall velocities tested as well. Therefore to gauge the effect of forcing on the resulting side force, the final 150 ms of each forcing cycle was used to estimate the average side force on the model. Figure 73 shows the resulting time-averaged side force coefficient, \overline{C}_y , as a function of the set moving wall velocity. To differentiate between port and starboard forcing, negative moving wall velocities indicate forcing on the port side, while positive moving wall velocities indicate forcing on the starboard side. From Fig. 73, the average side force appears proportional to the moving wall velocity, at least at this angle of attack and Reynolds number. This same trend is seen in the companion experiments when the average side force is compared to the applied voltage to the plasma actuation. Fagley et al. [2012a]

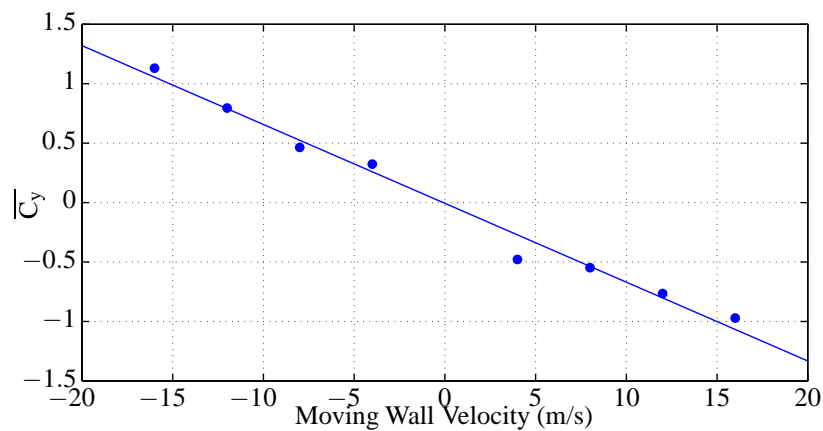


Figure 73: Average side force coefficient, \overline{C}_y , for different moving wall velocities. A positive moving wall velocity indicates forcing on the starboard side, while a negative moving wall velocity indicates forcing on the port side. All forcing is tangential to the model in the downstream direction.

5.4.5.4 Proper Orthogonal Decomposition of the Flow Field The serial dataset alternating between port and starboard forcing at 12 m/s (see Fig. ??), which was saved on the tap grid shown in Fig. 69, was analyzed and the spatial/temporal POD modes were calculated. Figure 74 shows the cumulative energy captured in the calculated POD modes based on the pressure field. As shown in the inset of Fig. 74, using the pressure field for the POD analysis requires over 50 modes to capture approximately 99 percent of the energy in the flowfield. However, the very first mode (in this case the mean) captures 98 percent of the energy. Therefore, a large number of modes are required to account for the fluctuations from the mean in the pressure field.

Figure 75 shows the resulting first five spatial POD modes based on the pressure from the tap data. In this case, the first mode exactly corresponds to the mean pressure field, while the second spatial mode accounts for the shift of the primary vortices into an asymmetric state. As shown in Fig. 75b), a 'X'-shaped pattern in the mode can be seen, especially near the rear of the model. Therefore, when the time coefficient is positive, the port vortex is shifted away from the ogive, while the starboard vortex is shifted towards the body. This shifting of the two primary vortex positions is confirmed by the second POD mode time coefficient, Fig. 76, in which the time coefficient and the model side force are clearly correlated. Note that in Fig. 76, the time coefficient

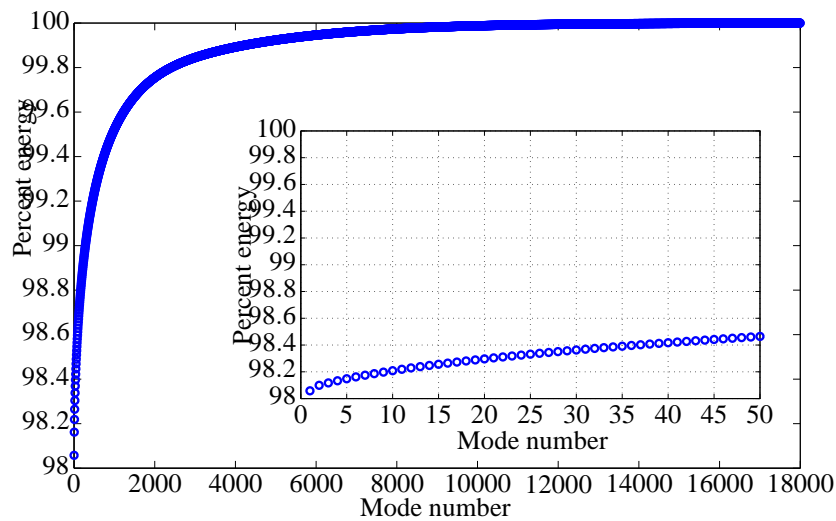


Figure 74: Cumulative energy content captured in each POD Mode. The inset shows a zoomed in view of the first 50 Modes energy content.

has been scaled to match the scaling of the side force coefficient. Furthermore, very similar spatial structures were also obtained when POD modes based on total vorticity were calculated.

As for the higher spatial modes and associated time coefficients, no clear correlation between these modes and the resultant side force has been found. However, based on the results shown in Fig. 74, these higher order modes contribute very little to the total amount of energy contained in the flowfield. Notice however that these higher-order modes do not appear in conjugate pairs like POD modes from periodic flowfields which create traveling structures. This is because, while there are minor fluctuations in the positions of the vortex, once locked into one state the vortices tend to stay there.

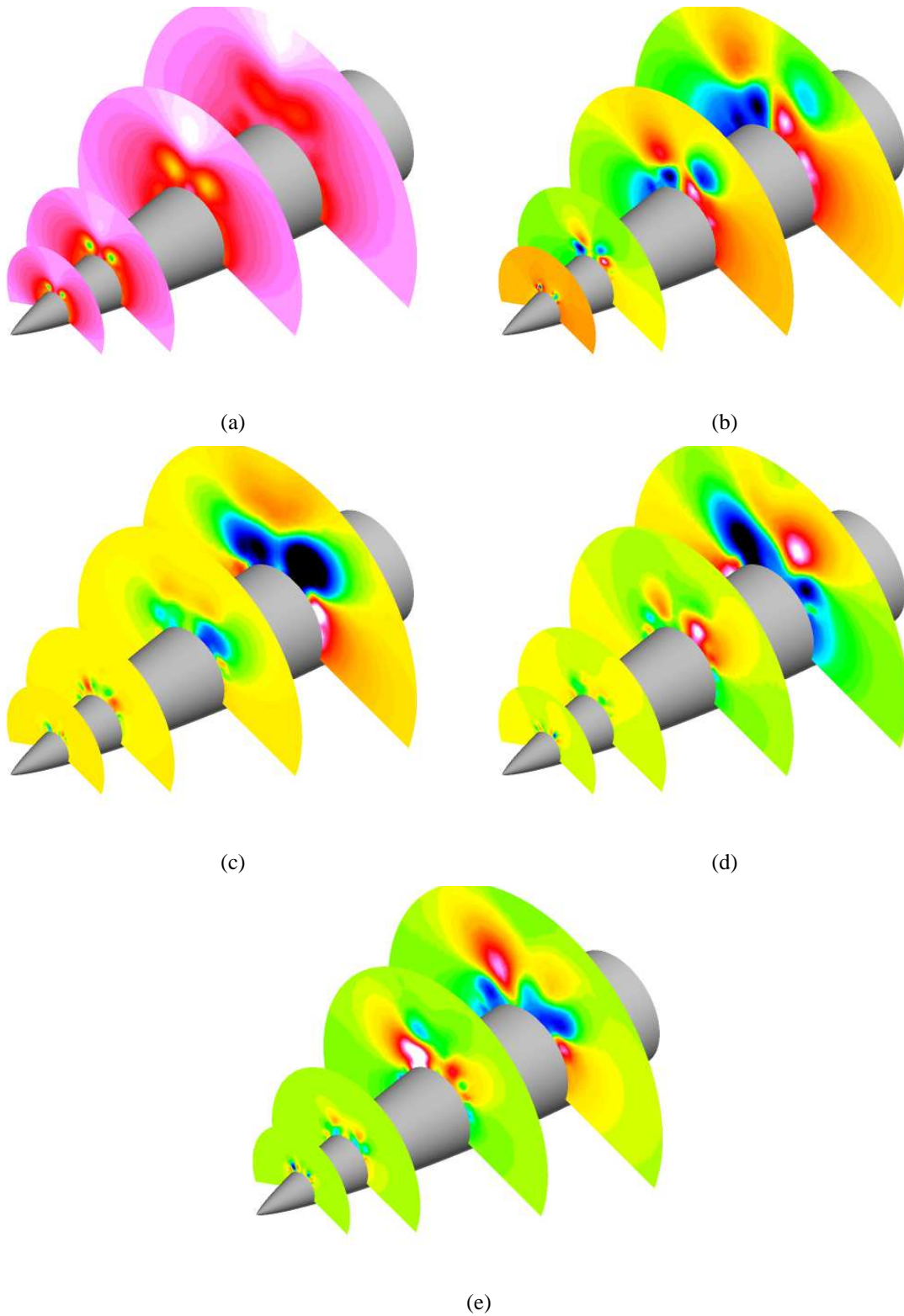


Figure 75: First five spatial POD modes: a) Mode 1, b) Mode 2, c) Mode 3, d) Mode 4, and e) Mode 5.

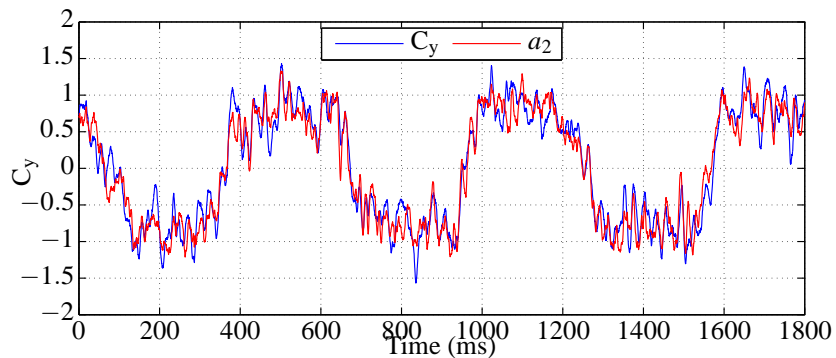


Figure 76: Comparison of the instantaneous side force coefficient and the 2nd POD mode time coefficient.

As a check, POD was performed on the time-resolved simulation data. The port and starboard data sets at a mass flow rate of 0.07 were concatenated into a single data before performing the analysis. As shown in Figure 77, very similar results are obtained using the time-resolved data, especially in the 1st and 2nd spatial modes, where the 'X'-shaped pattern can still clearly be seen in the 2nd mode. Furthermore, as shown in Figure 78, the 2nd mode still closely follows the side force on the model. In this case, a large spike occurs in the 3rd POD time coefficient corresponding to the swap in side force.

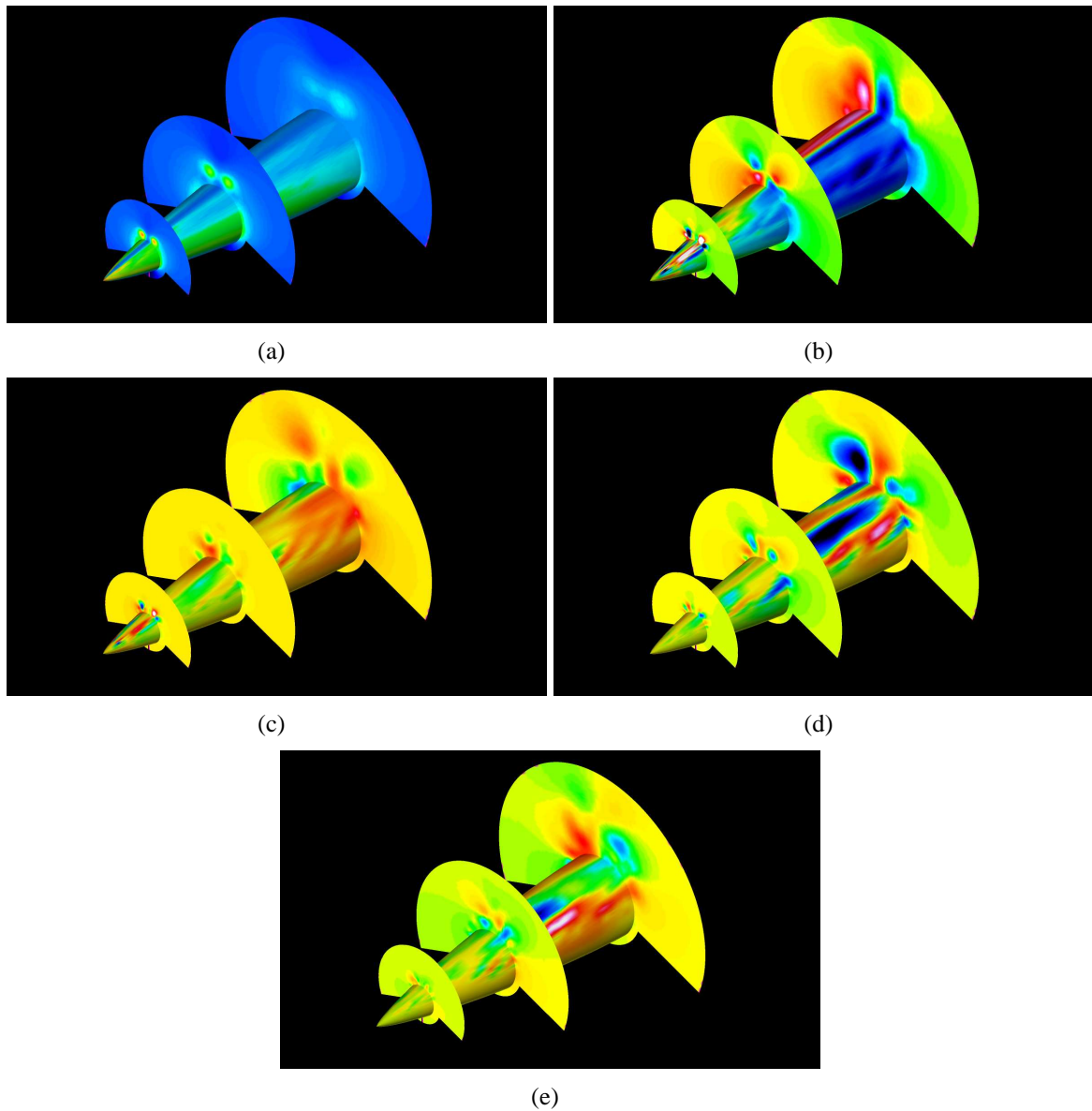


Figure 77: First five spatial POD modes using the time-resolved simulation data: a) Mode 1, b) Mode 2, c) Mode 3, d) Mode 4, and e) Mode 5.

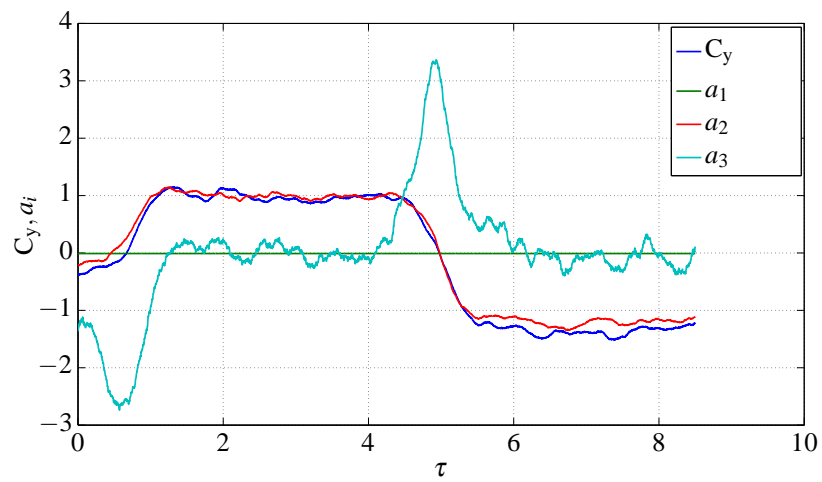


Figure 78: Comparison of the instantaneous side force coefficient and the first three POD mode time coefficient from the time-resolved data.

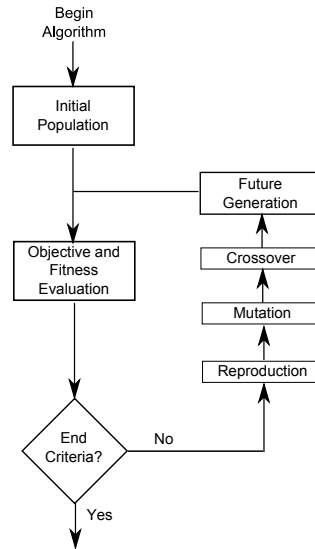


Figure 79: Procedure for genetic search algorithm.

5.4.6 Sensor placement

This section presents a numerical study on optimal sensor location and number of sensors to adequately estimate both the asymmetric vortex states and transients therein. For the purpose of this study, the flow state is defined as the side force coefficient (C_y) which entirely captures the asymmetric vortex behavior. The side force is the desired control variable, and thus it is imperative to have a surface sensor arrangement that accurately predicts the dynamics of this quantity. The following sections outlay the approach used for determining surface sensor placement for the von Kármán ogive.

5.4.6.1 Optimal Method The optimization problem is solved by using a constrained, evolutionary genetic algorithm (GA). The constrained optimization problem as a stochastic search routine is designed for the problem,

$$\min_{\mathbf{x} \in \mathbb{R}^n} F(\mathbf{x}), \quad (80)$$

where \mathbf{x} is the search variable defined in space $\in \mathbb{R}^n$ subject to an arbitrary function $F(\mathbf{x})$. This is a constrained optimization problem with \mathbf{x} subject to the constraint,

$$L_i \leq x_i \leq U_i, \quad (81)$$

where L_i is the lower bound and U_i is the upper bound for our search vector x_i . This evolutionary search based method is a classical approach for these multidimensional constrained optimizations. The basic architecture of the GA is shown in Fig. 79. With any GA search routine an initial population or array of potential solutions is randomly selected. The objective function is then evaluated at each member of the population. The objective function provides a measure on how well that member of the population performed. The fitness function transforms the result into a relative fitness. Poorly fit members are discarded and fit members are replicated in the reproduction step. Combinations of fit members are randomly selected and then mutated to form the next iterative population. This process continues until a desired stop criteria is satisfied.

In application to the problem of the von Kármán ogive, the objective function is defined as

$$f(\mathbf{x}_s) = C_y(t) - Cp(\mathbf{x}_s, t) \quad (82)$$

where C is the observation and computed from a least squares estimate (see below). The fitness function is defined as the 2-norm of the objective function,

$$F(\mathbf{x}_s) = \|f(\mathbf{x}_s)\|_2. \quad (83)$$

The search domain ($L_i \leq x_i \leq U_i$,) is restrained to the upper surface of the ogive. Symmetric sensor placement is enforced, such that at each axial position two sensors are placed at the $\pm\theta$ positions.

5.4.6.2 Linear Stochastic Estimation Linear stochastic estimation (LSE) is chosen as the baseline estimation method. Since flow fields of interest are typically highly non-linear, the performance of this method usually tends to be poor for most flow fields. However, a linear analysis is always important because it serves as a benchmark comparison for the more complex, non-linear system ID methods. Secondly, the computational time for the linear analysis is negligible, thus allowing for an optimal study in terms of sensor location and number.

The CFD simulation provides surface pressure at any point on the surface of the ogive. The array of surface sensors is defined as the vector, \mathbf{x}_s . A linear mapping which estimates the state of our flow field is sought. The observation matrix C is computed to best represent the flow state in a least squares sense. C is computed by a matrix inversion,

$$C = C_y(t)p(\mathbf{x}_s|t)^{-1} \text{ where } C \in \mathbb{R}^{m \times k}. \quad (84)$$

Future estimates can then be approximated by the matrix multiplication,

$$\hat{C}_y(t) = C\mathbf{p}(\mathbf{x}_s, t)label(e.P_{est}) \quad (85)$$

The performance of the linear estimation approach is quantified by the error norm of the estimate. The error is defined as

$$\varepsilon = \|C_y(t) - Cp(\mathbf{x}_s, t)\|_2 \quad (86)$$

This is the very basic estimation method. The linear and stationary approach provides for a means to optimally solve for ideal surface arrangement. A surface sensor array is sought to minimize the error in (86). Once the sensor array is determined, the estimation method can be extended to non-stationary, higher order, non-linear methods. The optimal arrangement of sensors in a linear fashion will also be optimal for higher order methods as well.

5.4.6.3 Results The unforced data, shown in Fig. 80 a), indicates that while a significant side force coefficient, $|C_y| \approx 1$, can be achieved with this geometry in simulations, it is smaller than the experimental findings. However, the unsteadiness of the side force coefficient around the zero point shows that the flow is unstable with respect to the vortex state when no geometric disturbance is present to enforce either the port or starboard asymmetric vortex states.

Fluidic actuation is introduced into the numeric simulation via two moving wall boundary conditions at the tip of the von Kármán ogive, as shown in Fig. 68. The forcing is duty cycled

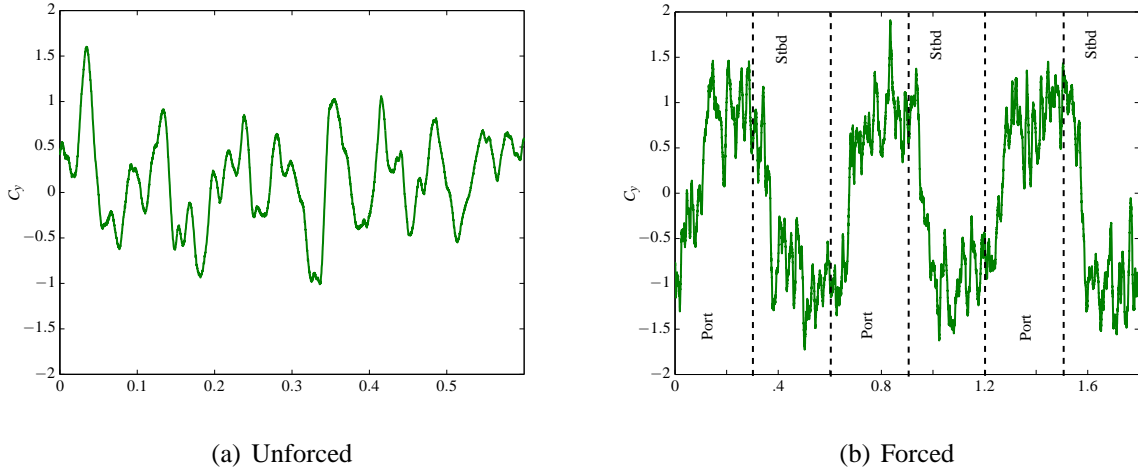


Figure 80: a) Unforced side force coefficient. b) Forced side force coefficient.

between port and starboard actuators to produce both asymmetric states, deterministically within the flow field. For both forcing situations, the unforced state of the vortices is altered resulting in a side force comparable to experimentally measured values, such that the flow has entered into a pseudo-steady asymmetric state, see Fig. 80 b). It was determined from this data that the data for the unforced case would provide more difficulty for the estimation/optimal routine because of the large number of transients between asymmetric states as well as the reduced magnitude of side force (i.e. smaller differential pressures from port to starboard). The unforced data was then selected to be the training data for the optimal routine and the forced data was selected for the validation of the resulting sensor configuration.

The sensor location are bounded to the leeward side, $\theta = \pm 110^\circ$, of the ogive over an axial range of $1 \leq x/D \leq 4$. Another spatial constraint is the sensor array must be symmetric about the $z = 0$ plane to ensure symmetric sensor placement. Thus the necessary parameters to optimize over are the axial and the azimuthal positions of a sensor pair, $\mathbf{x}_s = [x_1, \theta_1, x_2, \theta_2, \dots, x_k, \theta_k]^T$, for $2k$ sensors. The bounds or constraints on the search criteria are thus,

$$\begin{aligned} 1 &\leq x/D \leq 4 \\ 0 &\leq \theta \leq 110^\circ \end{aligned} \quad (87)$$

The (x,y,z) coordinates are then computed from the axial and theta orientations, such that,

$$\mathbf{x}_{\text{surf}} = \begin{bmatrix} x_1 \\ y_1 \\ z_1 \\ x_2 \\ y_2 \\ z_2 \end{bmatrix} = \begin{bmatrix} x_1 \\ r(x_1)\cos(\theta_1) \\ r(x_1)\sin(\theta_1) \\ x_1 \\ r(x_1)\cos(\theta_1) \\ r(x_1)\sin(-\theta_1) \end{bmatrix} \quad (88)$$

where the radius at that axial location, $r(x_1)$ is computed from (??)- (??). The vector \mathbf{x}_{surf} contains the coordinate pairs over the bounded region and mirrored about the meridian plane. The pressure information at \mathbf{x}_s is linearly interpolated from a surface tap grid on the ogive using Delaunay triangulation.

To ensure the correct optimal method with associated parameters (i.e. population size, mutation rate selection/deletion properties and mutations/crossover operators) were chosen for the optimal study of sensor location and number of sensors, the entire error surface was computed for a single sensor pair and compared to the results from the genetic algorithm. The error surface plot is shown in Fig. 81.

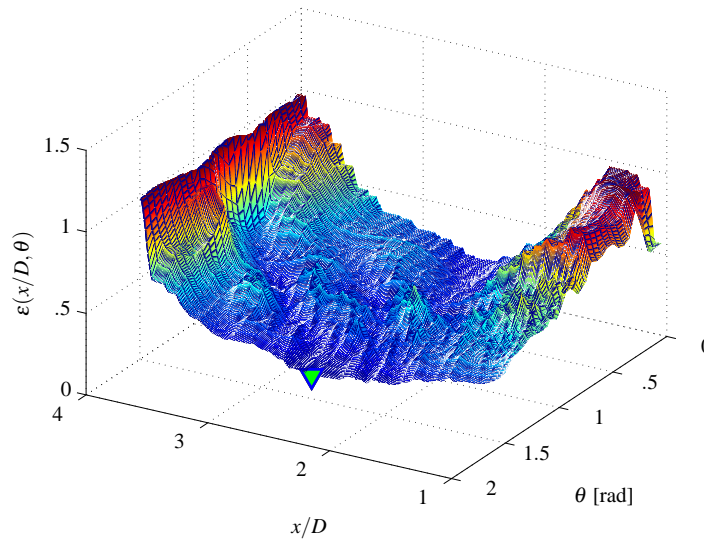


Figure 81: Error surface of a single sensor pair and optimal solution shown to be at location of minimum error thus validating the optimal routine.

The optimal solution as computed by the above method produces $x_{opt}/D = 2.4$ and $\theta_{opt} = 1.5$ which is plotted as a green triangle in Fig. 81. This does align with the minimum of the error surface, so the optimal method is validated for this type of minimization problem. Note also that the error of the linear estimator becomes much worse outside the bounds of $x/D \geq 3.5$ and $x/D \leq 1.5$. This is mainly due to the dynamics of the asymmetric vortex phenomena. The strongest asymmetries are seen in the axial region from $1.5 \geq x/D \geq 3.5$. Also it is seen that the minimal amount of error is at the largest azimuthal positions, i.e. $\theta = \pm 110^\circ$. This indicates that the sensors near the separation lines are critical to capture the asymmetric dynamics.

The optimal solution was repeated for 2, ..., 6 pairs of sensors. The results are shown in Fig. 82. As the number of sensors is increased the error of the linear estimator is decreased for the training data. Interestingly though, the error does not decrease for the validation data but rather increases if more than 6 sensors (3 pairs) are used. Because experimental implementation is crucial for this project, it was determined that a sensor array with two sensor pairs provided the best compromise. Also, the prediction error was not significantly reduced when more sensor pairs were used. The optimum positions for the two sensor pair array were found to be,

$$\begin{aligned} x/D &= [2, 3.25] \\ \theta &= [\pm 105^\circ \pm 98^\circ] \end{aligned} \quad (89)$$

Figure 83 shows the unwrapped surface of the ogive colored in gray by the mean pressure distribution for the training data ensemble. The locations of the two sensor pairs are shown in Fig. 83 as

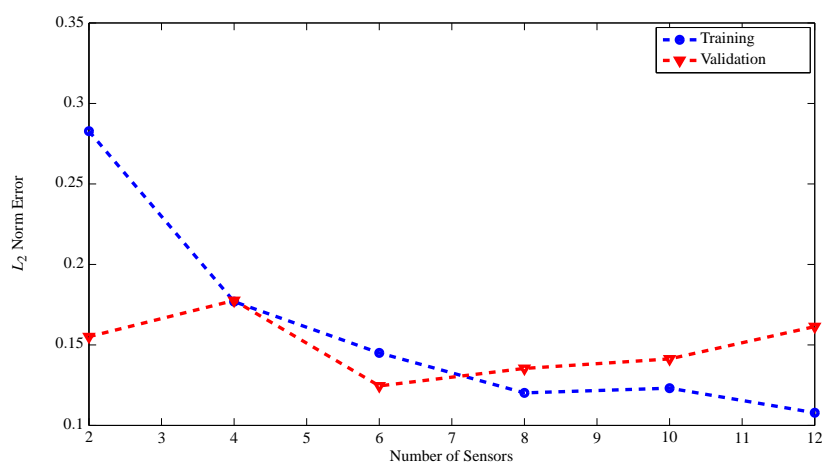


Figure 82: Overall error plotted versus number of sensors at their optimal locations. Performance of the training and validation are shown in blue and red, respectively.

green dots. Figure 83 also shows instantaneous separation locations for the port asymmetric state (red) and instantaneous separation locations for the starboard asymmetric state (blue). This figure shows that the critical sensing locations for estimating the asymmetric state are near the separation locations. Also, the separation locations do slightly move depending on which asymmetric state is present. This small fluctuation in the separation location provides for very large fluctuations in relative pressures at the sensor location as shown in Fig. 84 for each asymmetric state.

The optimal routine found the point at which the largest differential pressure occurred just near the separation location. The time history of the estimation results for the training and validation cases are shown in Fig. 85. As shown the two sensor pairs predict the asymmetric behavior for the forced and unforced case producing less than 17% error for each case. Some high frequencies are not captured with this sensor placement, probably due to the fact that those asymmetric pressure changes are occurring further upstream or downstream on the body of the ogive.

5.4.6.4 Experimental Validation The flow state estimation technique laid out in Fagley et al. [2012b], is experimentally verified by the following technique. The estimated side force, \hat{C}_y , as described by Eqn. ??, needs to be validated and compared to the actual force on the model. To compare these two signals, the force balance sensor dynamics need to be measured and modelled. For this an impulse response to the wind tunnel model and resulting forces are measured to model the frequency response. Figure 86a shows the frequency response of the side force measurement due to an impulse. A multi-modal resonance is seen due to the complex orientation of strain gauge/flexure arrangement of the 6 degree of freedom force balance; additionally, each balance channel shows a cross coupled behavior which is also a factor for the multi-modal resonance.

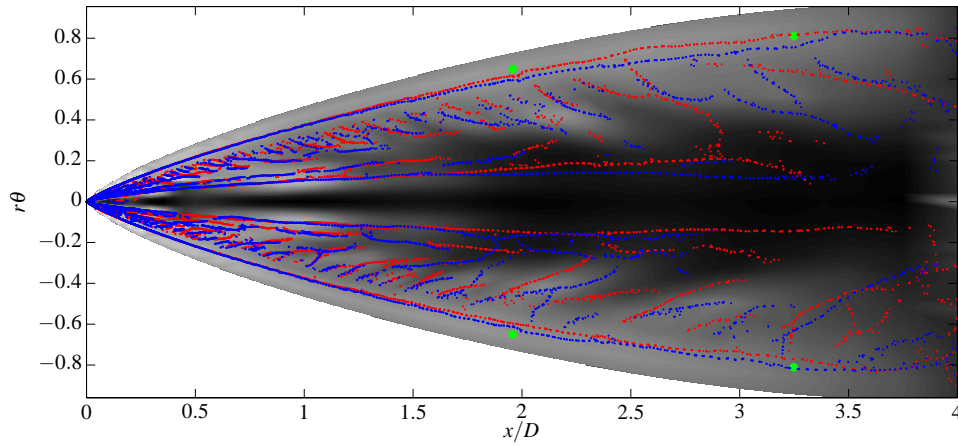
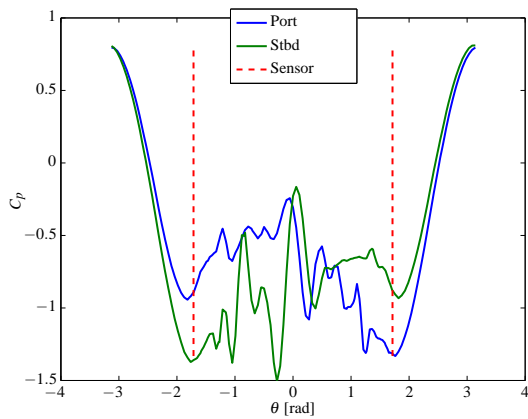
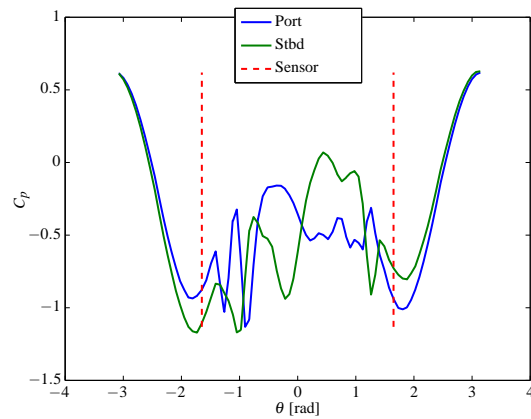


Figure 83: Unwrapped surface of the von Kármán ogive colored by mean pressure distribution. Red lines indicate separation locations for port forcing and blue lines indicate separation location for starboard forcing. Optimal sensor placement is shown as green dots.



(a) $x/D = 2$



(b) $x/D = 3.25$

Figure 84: Sensor placement as well as azimuthal pressure coefficient for port forcing (blue) and starboard forcing (green) at axial location a) $x/D = 2$ and b) $x/D = 3.25$

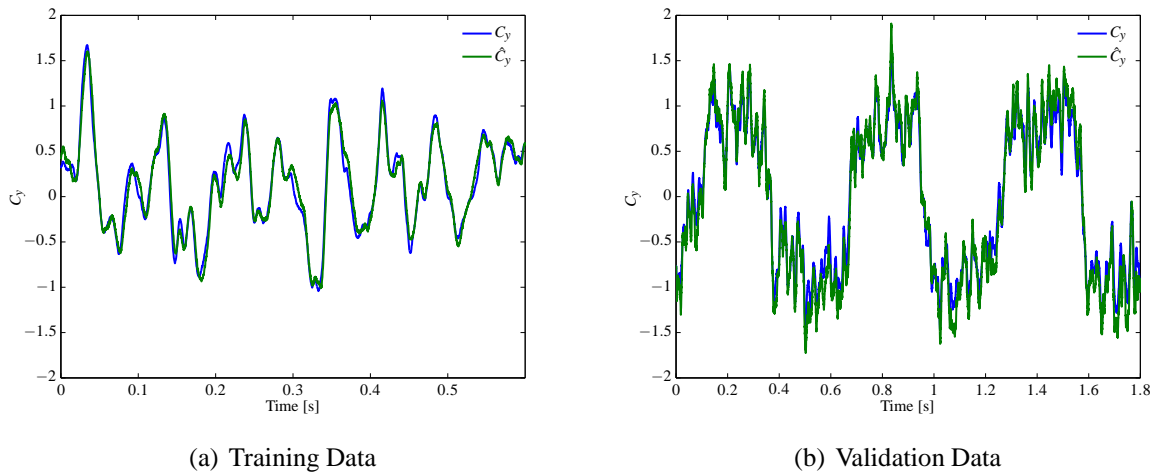


Figure 85: Time histories and estimation performance for training and validation data.

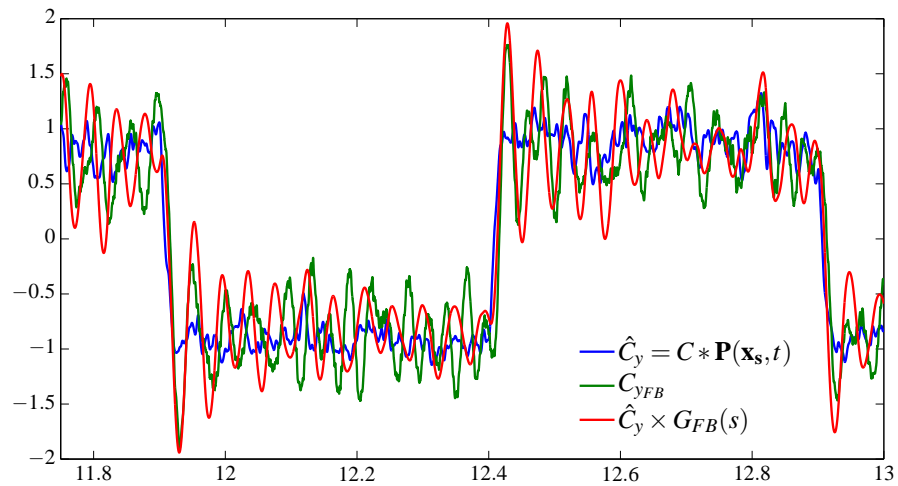
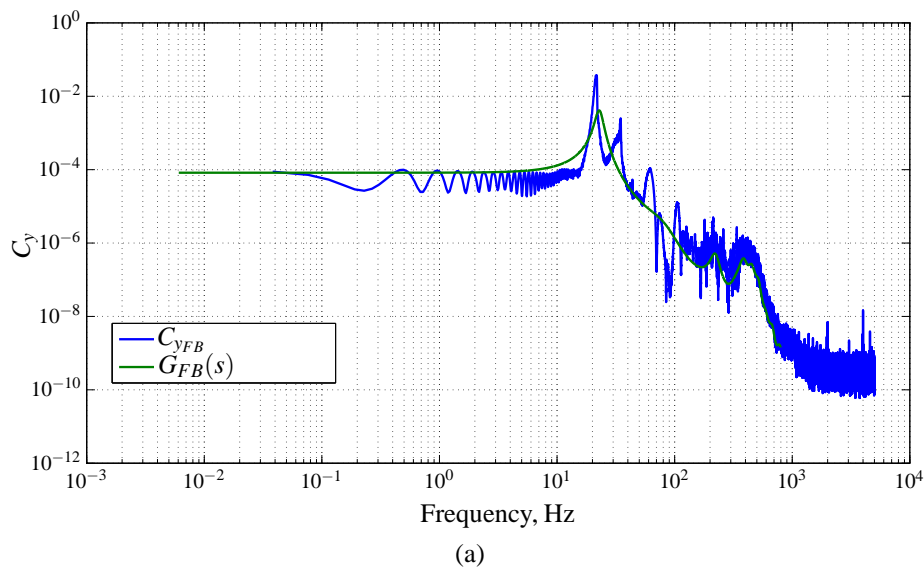


Figure 86: (a) Frequency spectrum of the side force measurement due to an impulse response [blue] and 8th order AR model [green]. (b) Time domain measurement of side force coefficient [green], estimated side force from pressure signals [blue] and estimated side force measurement when coupled with the dynamics in the AR model [red]

Nonetheless the spectrum shown in Figure 86b allows for modeling of the sensor dynamics. The impulse response of this measurement device is fit by an auto-regressive system in the form,

$$G_{FB}(q)C_{y_{FB}}(t) = e(t) \quad (90)$$

where $C_{y_{FB}}$ is the measurement of the side force and $G_{FB}(q)$ is a frequency domain model of the force balance. All three signals can be compared by the following equation,

$$C_{y_{FB}} \approx G_{FB}(s) * C \times \mathbf{P}(\mathbf{x}_s, t). \quad (91)$$

An example of these signals due to alternating port and starboard forcing is shown in Figure 86b. The green curve represents the actual side force measurement. The experimental measurements of the force balance are compared directly to the pressure based estimates of the force as shown in Eq ???. Figure 86b shows the actual force measurements in green, the estimated side force from the linear combination of pressure signals in blue, and the estimated force measurement with the force balance dynamics included in red. As shown qualitative agreement exists between all three signals; the determination is thus that the estimated side force \hat{C}_y is a more suitable signal for the actual force on the model, because the sensor dynamics of the force balance are excluded.

5.4.6.5 Summary Unforced and forced CFD simulations were used to understand the asymmetric vortex state behavior on a von Kármán ogive. The state of the flow was modeled using the side force coefficient. A genetic algorithm was used to solve for optimal sensor placement and investigate the performance as a function of number of sensors. The fitness function of the genetic algorithm was defined as the error between the least squares approximation of the surface pressure to the defined flow state.

An optimal arrangement of sensors was chosen which is experimentally feasible and in fact has been experimentally implemented. The current study showed that a total of two sensor pairs placed at position of $x/D = [2, 3.25]$ and $\theta = [\pm 105^\circ, \pm 98^\circ]$, accurately predicted the flow state to within 17% error for training (unforced) and validation (forced) simulations. The placement algorithm showed that sensors placed very near the separation point were optimal. This region showed the largest differential pressures for port and starboard asymmetric vortices, which heuristically is the best location for flow state sensors.

5.4.7 System dynamics and modeling

To model the system dynamics of the asymmetric vortex state behind the von Kármán ogive at high angles of attack, open-loop experimental tests were conducted to understand system characteristics in terms of stability/bi-stability, controllability, observability, and linear/non-linear behavior. The flow behind an axisymmetric slender body has previously been shown to be completely bistable at a sufficiently large angle of attack and small Reynolds numbers. Because few tests have been conducted at a Reynolds number in the range of the current experiment ($Re = 156,000$), determining if a bi-stable or proportional flow regime exists is critical in designing a suitable model structure and control system design.

The system with the characteristics shown in Figure 56 is suitable for being modeled by a linear system with saturation points as well as a dead zone. Therefore, standard linear system identification methods can be used for the system identification to extract critical features such as delay time, rise time, cut-off frequency, phase/gain margin and minimum phase behavior. Once these critical features are well quantified, the linear system will provide the means for closed-loop controller development. For the open-loop database, the plasma actuator voltage is varied in different manners to fully describe and model the dynamics. In this experimental investigation three separate campaigns were conducted to develop the open-loop database. For training the model, a step response is measured, which contains all necessary information for a linear model to be developed. Linear modeling methods, such as the output error, prediction error and subspace identification methods are implemented to capture the dynamic response to the step input. For validation of the developed model, both impulse and sinusoidal forcing responses are compared to experimental validation.

Initially, due to geometric asymmetries, angular misalignments or flow imperfections the system is in the port asymmetric state which causes a port attached vortex, i.e. a negative C_y or ΔC_p . This steady state value is removed and relative changes to the asymmetric state are analyzed. For all modeling purposes the side force estimate, \hat{C}_y , will be used. Also, for all of the data presented, only the port (negative voltages) and starboard (positive voltages) actuators are employed to influence the flow state.

5.4.7.1 Modeling Techniques The system response is modeled using a linear system parametrization. The input output relationship for this system is

$$Y(s) = G_s(s)U(s). \quad (92)$$

The structure of the model in continuous time will take the form,

$$G_s(s) = \frac{N(s)}{D(s)} = Ke^{\theta s} \frac{s^m + a_{m-1}s^{m-1} + a_{m-2}s^{m-2} \dots a_1s + a_0}{s^n + b_{n-1}s^{n-1} + b_{n-2}s^{n-2} \dots b_1s + b_0} \quad (93)$$

for a linear system with m zeros and n poles and a pure time delay, $e^{\theta s}$. Different system identification techniques exist for parameterizing suitable orders $G(s)$ and solving for coefficients of the polynomials in numerator and denominator. The three techniques for time domain identification which are examined in this effort are: Output Error (OE), Prediction Error (PEM), and Subspace Identification (SSID) methods.

5.4.7.2 Output Error Method The output error method is an autoregressive exogenous input (arx) model structure, and the identification method is well representative of discrete time and frequency domain data of the form,

$$y(k) = \frac{B(q)}{F(q)}u(k - n_k) + e(t). \quad (94)$$

The OE method minimizes the cost function

$$\|y(k) - \hat{y}(k|\theta)\|_2^2, \quad (95)$$

given a parameterized vector which contains numerator order, denominator order and pure time delay, n_B, n_F, n_k , respectively. The optimal parameter vector, $\hat{\theta}$ is given by

$$\hat{\theta} = \min \frac{1}{N} \sum_k^{N-1} \|y(k) - \hat{y}(k|\theta)\|_2^2, \quad (96)$$

For this study the pure, convective time delay is estimated from the step response measurements as shown in Table 7. Six values for n_k are chosen for these formulations. The true pure delay time is shown to be 8 ms with a sample time of $T_s = 0.1$ ms which corresponds to a discrete delay time of $n_k = 80$. Because convective time and non-minimum phase aren't decoupled, the convective time parameter was varied to allow for the zeros to adjust accordingly to any non-minimum phase behavior. Both the numerator orders, n_B , and denominator orders, n_F , are chosen over a range from 1 to 5. With these three parameter ranges, a total of 150 OE models were compared and validated.

5.4.7.3 Prediction Error Method The prediction error method (PEM) has a model structure given by an autoregressive moving average (arma) system, and is an iterative identification approach for multi-input multi-output time domain data with a model structure of the form

$$A(q)y(k) = \frac{B(q)}{F(q)}u(k - n_k) + \frac{C(q)}{D(q)}e(t). \quad (97)$$

This linear time model incorporates a system disturbance term which is filtered by the $\frac{C(q)}{D(q)}$ transfer function (a type of moving average). The parametrization for this model structure consisted of a total of six parameters as shown by,

$$\theta = [n_a, n_b, n_c, n_d, n_f, n_k]^T, \quad (98)$$

where each numerator and denominator order is denoted by n_i . Each order was varied from 1 through 5 and the delay term was set to the convective time delay computed from the step input which was approximately 8 ms. All models were compared and validated against experimental validation data in following sections.

5.4.7.4 Subspace Identification Method The subspace identification (SSID) method is widely used for black box modeling of linear dynamical systems directly in the state space domain, which are written as,

$$\begin{aligned} x_{k+1} &= Ax_k + Bu_k + Ke_k, \\ y_k &= Cx_k + Du_k + e_k, \end{aligned} \quad (99)$$

where u_k is the m -dimensional input, x_k is the n -dimensional state, y_k is the l -dimensional output and K is the Kalman gain. The SSID method is highly useful for MIMO systems, because of its numerical robustness, and its model order optimization based on the singular values of the Hankel matrix. On the downside, large data sets are needed to form the block Hankel matrices, known deterministic processes are difficult to implement, and a strong theoretical understanding of observability and controllability is necessary. The basic premise is to form the Hankel matrices of the input-output data set; the observability matrix,

$$\mathcal{O} = [C \ CA \ CA^2 \cdots CA^{n-1}]^T, \quad (100)$$

and the reversed controllability matrix,

$$\mathcal{C} = [A^{n-1}B \cdots A^2B \ AB \ B]^T, \quad (101)$$

are imbedded within this large input-output Hankel data matrix. An appropriate model order can be estimated by the singular values of this Hankel matrix. Once the model order is selected, system matrices as shown in Eq (99) can be extracted.

5.4.7.5 Model Selection Experiments The three modeling techniques described in section 5.4.7 are applied to the training data. The RMS error between the predicted response and actual response serves as the figure of merit for model selection. Transient areas where the input contained high frequency changes were weighted more heavily in the calculation of the prediction error. The best model from each reduced order modeling technique was chosen and model order and structure was compared. Model structure was consistent around a 4th or 5th order model. Also, the poles of the models tended to migrate outside the unit circle if the convective time delay was inaccurate; this non-minimum phase behavior allowed for the discrepancy in the time delay of the model.

The results for the best simulated model responses in comparison to experimental measurements of the step response are shown in Figure 87. Initial and ending transients show very good prediction of convective delay as well as rise/fall time constants as shown in Table 7. The dynamics vary slightly differently when the asymmetric state transitions from port to starboard versus from starboard to port. The transient time from starboard to port vortex states is shorter and the overshoot is greater, as Table 7 indicates. This is potentially because the initial state prefers the port asymmetric state which may provide an additional restoring force to the vortex dynamics. The linear approach taken in this paper finds the mean dynamics between each state trajectory as shown by Figure 87. Nevertheless, each of the models replicates the asymmetric vortex dynamics to a step input very well, thus validating the model parameterizations as well as model selection technique.

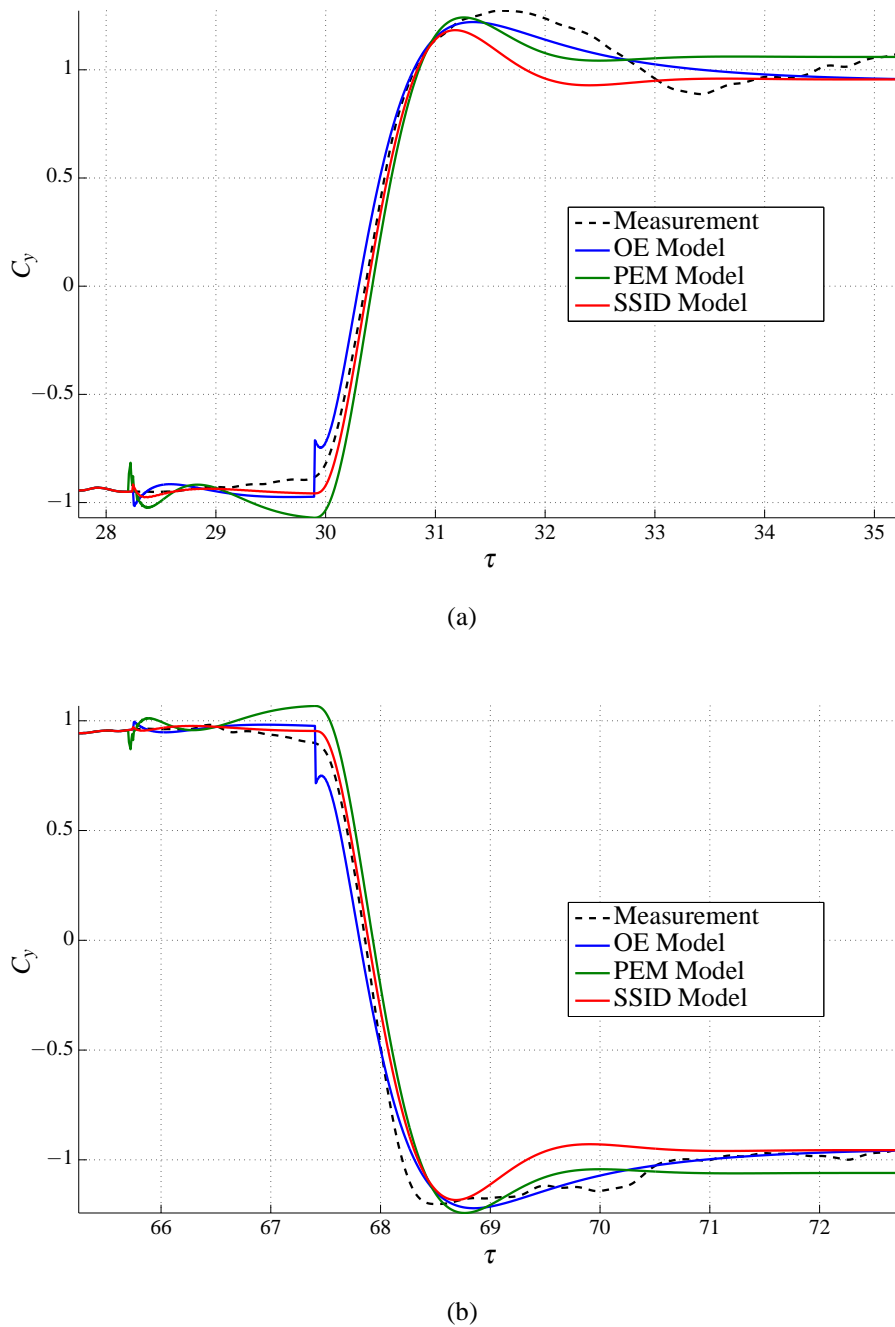


Figure 87: Step response comparison of OE, PEM, and SSID modeling methods. (a) Initial transient and (b) ending transient of step response of estimated side force, \hat{C}_y , based on pressure measurements

The validation data sets were also used to evaluate model performance. The models were calculated against both of the sinusoidal forcing and impulse forcing inputs. The response of the asymmetric state and model responses were compared. Figure 88a shows the summary of the frequency response data which aligns well with the raw frequency measurements. The phase relationship is also shown in Figure 88b. To select between the three different model development

approaches, the error is minimized in the frequency domain. The prediction error technique most adequately fits the frequency domain data, in both magnitude and phase.

Interestingly, the cutoff frequency of the system which is determined from a -90° phase is approximately $1/(2\tau)$. This means more or less that any frequencies larger than an associated period of two flow through times will be greatly attenuated. This is shown in Figure 88a.

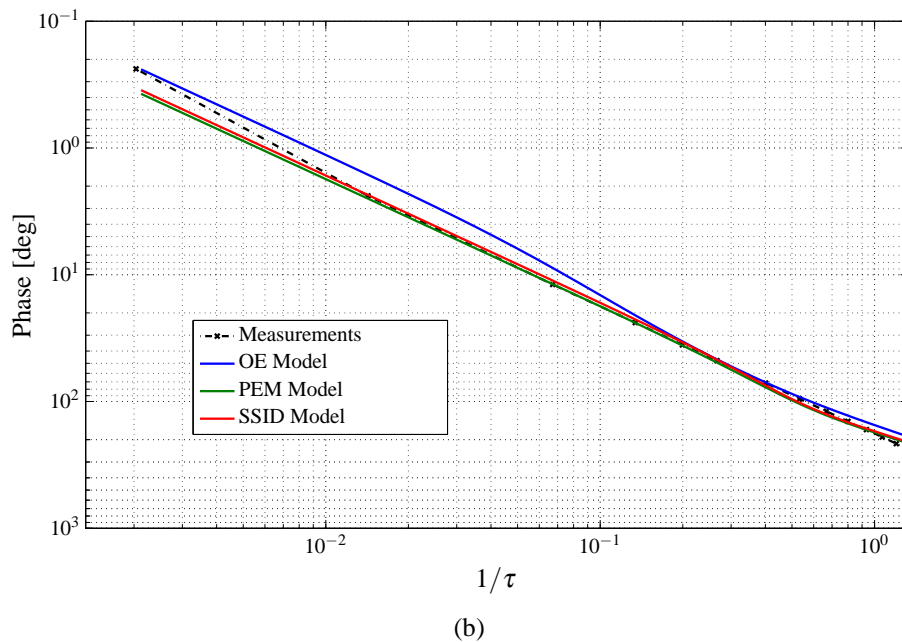
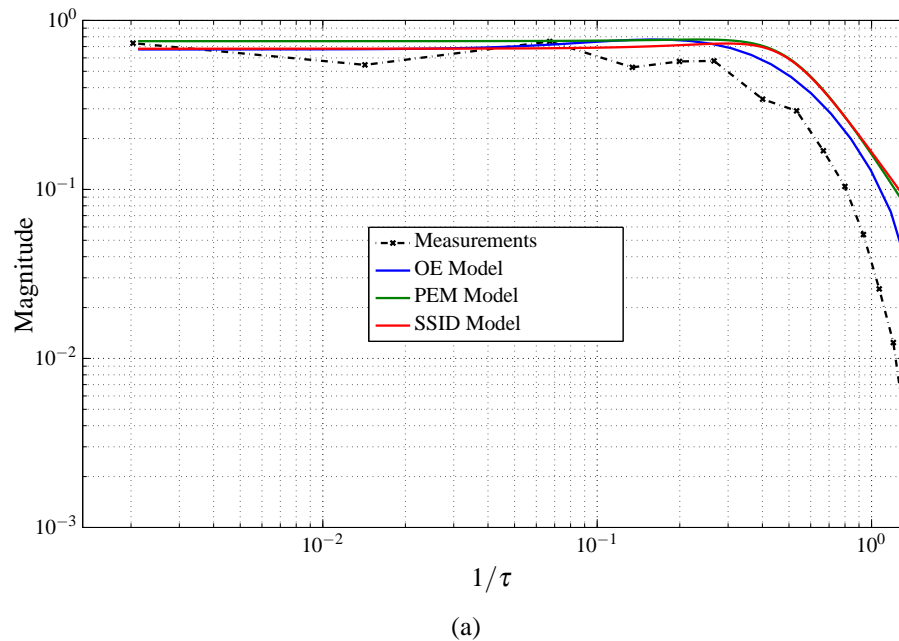


Figure 88: Comparison of model frequency response and experimental measurements.

Figure 89 shows the impulse response with varying duty cycles for the experimental and sim-

ulated output error model results. The various colors represent the different duty cycles. The solid lines represent experimental measurements and the dashed lines represent the PEM model prediction. All of the impulses were initiated at time equal to zero with the ending duration of the impulse indicated by a vertical dashed line. The linear model has a slightly different gradient during transient times and a small amount of overshoot when returning to the initial state.

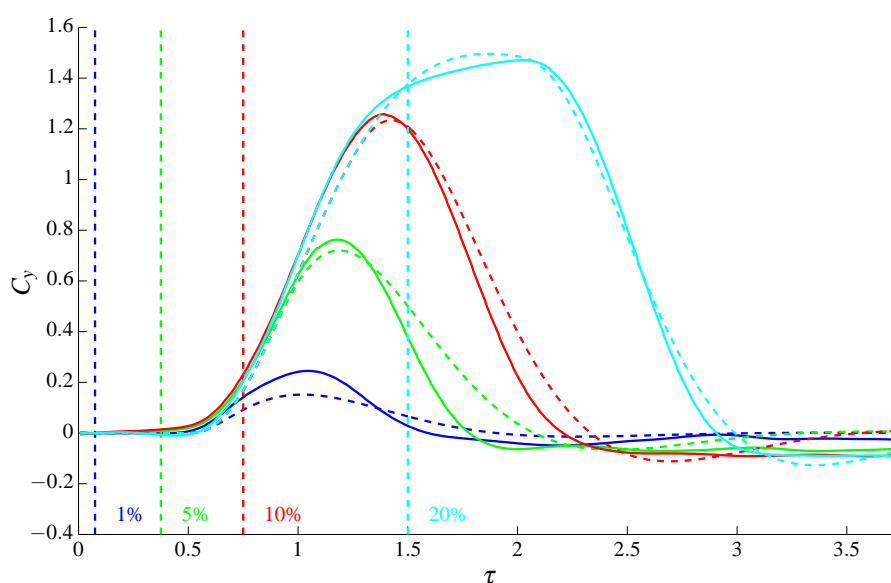


Figure 89: Validation of output error model for simulation of impulse response with varying duty cycles. Model response is shown in dashed line and experimental measurement is shown in solid line

5.4.7.6 Model Selection Simulations The three modeling techniques described in section 5.4.7 are applied to the step response data. The RMS error between the predicted response and actual response serves as the figure of merit for model selection. Transient areas where the input contained high frequency changes were weighted more heavily in the calculation of the prediction error. The best model from each reduced order modeling technique was chosen and model order and structure was compared. Model structure was consistent around a 4th or 5th order model. Also, the poles of the models tended to migrate outside the unit circle if the convective time delay was inaccurate; this non-minimum phase behavior allowed for the discrepancy in the time delay of the model.

The results for the best simulated model responses in comparison to experimental measurements of the step response are shown in Figure 90. Initial and ending transients show very good prediction of convective delay as well as rise/fall time constants as shown in Table 7. The dynamics vary slightly differently when the asymmetric state transitions from port to starboard versus from starboard to port. The transient time from starboard to port vortex states is shorter and the overshoot is greater, as Table 8 indicates. This is potentially because the initial state prefers the port asymmetric state which may provide an additional restoring force to the vortex dynamics. The linear approach taken in this paper finds the mean dynamics between each state trajectory as shown by Figure 90. Nevertheless, each of the models replicates the asymmetric vortex dynamics

to a step input very well, thus validating the model parameterizations as well as model selection technique.

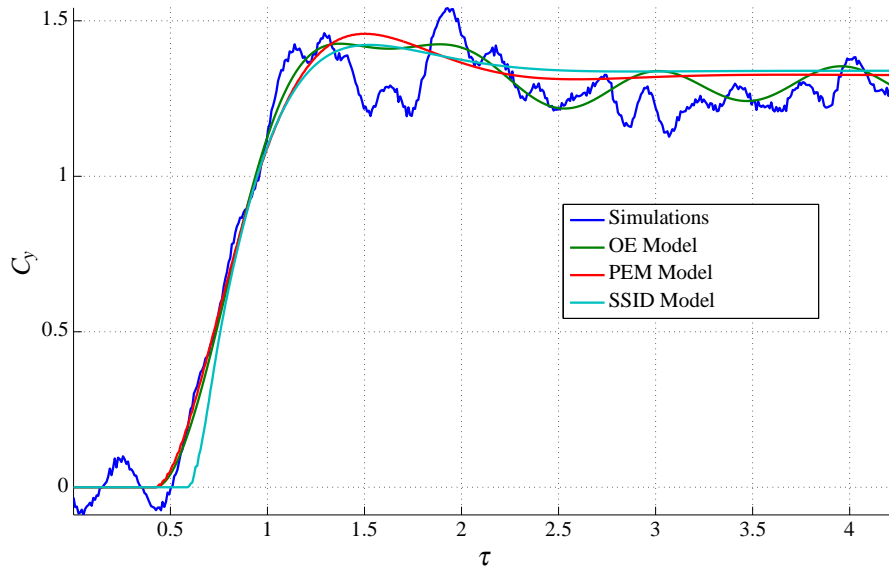


Figure 90: Step response comparison of OE, PEM, and SSID modeling methods. (a) Initial transient and (b) ending transient of step response of estimated side force, \hat{C}_y , based on pressure measurements

The validation data sets were also used to evaluate model performance. The models were calculated against both of the sinusoidal forcing and impulse forcing inputs. The response of the asymmetric state and model responses were compared. Figure 91a shows the summary of the frequency response data which aligns well with the raw frequency measurements. The phase relationship is also shown in Figure 91b. To select between the three different model development approaches, the error is minimized in the frequency domain. The prediction error technique most adequately fits the frequency domain data, in both magnitude and phase.

Interestingly, the cutoff frequency of the system which is determined from a -90° phase is approximately $1/(2\tau)$. This means more or less that any frequencies larger than an associated period of two flow through times will be greatly attenuated. This is shown in Figure 91a.

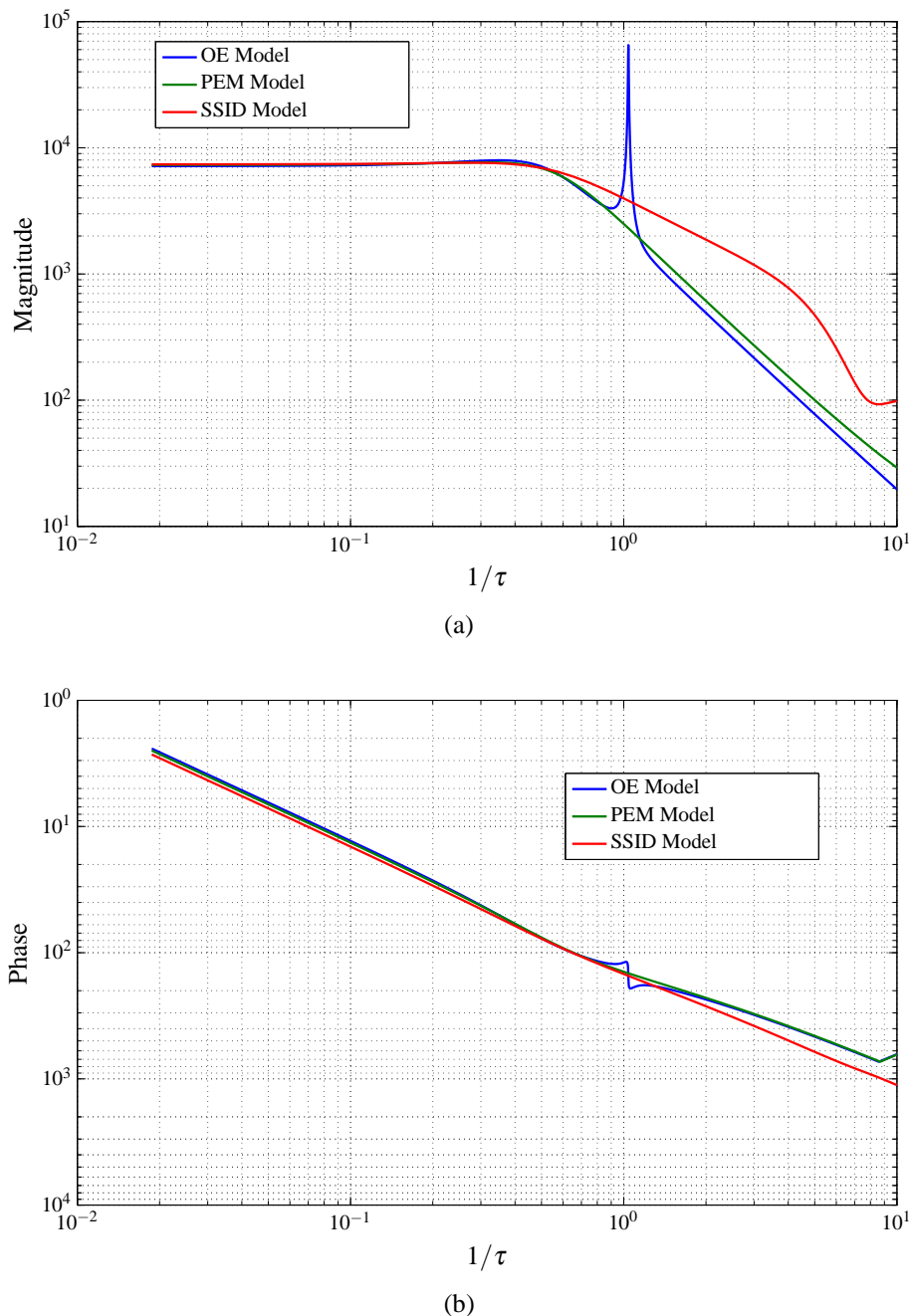


Figure 91: Comparison of model frequency response, both magnitude (a) and phase (b).

Figure 92 shows the impulse response with varying duty cycles for the CFD simulation results and simulated prediction error model results. The various colors represent the different duty cycles. The solid lines represent experimental measurements and the dashed lines represent the PEM model prediction. All of the impulses were initiated at time equal to zero with the ending duration of the impulse indicated by a vertical dashed line. The linear model has a slightly different gradient during transient times and a small amount of overshoot when returning to the initial state.

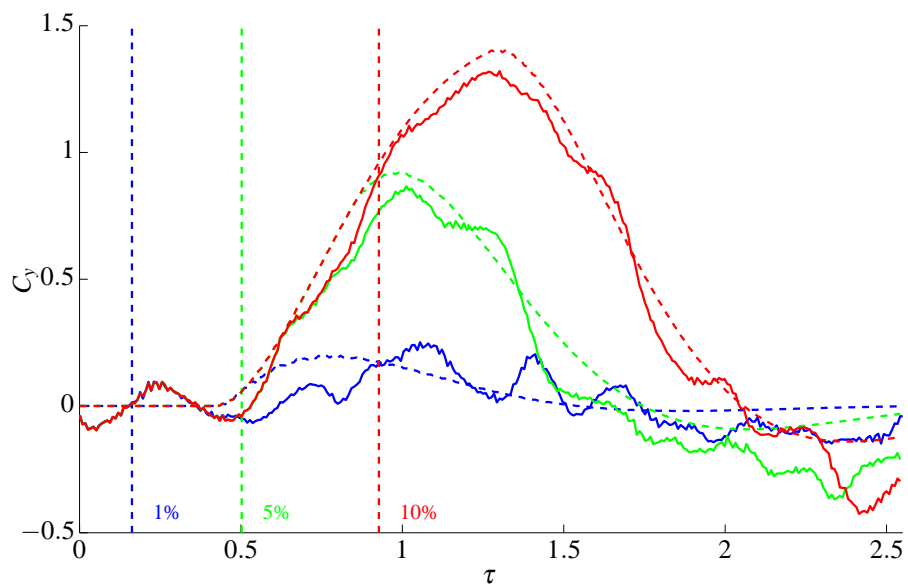


Figure 92: Validation of prediction error model for simulation of impulse response with varying duty cycles. Model response is shown in dashed line and CFD simulation results are shown in solid line

5.4.8 Closed loop dynamics

Now that the system dynamics in Eq 92 have been modeled, i.e. the relationship between plasma voltage and estimated side force response is determined, the closed-loop system can be realized. The overall design of the control diagram is shown in Figure 93. The type of control system selected is a reference tracking feed forward approach where $G_s(s)$ is the plant as developed in section 5.4.7, $G_c(s)$ is the control system, and $G_d(s)$ is the output disturbance/measurement noise. The unforced fluid state and measurement noise is modeled by an output disturbance, which is colored by the unforced dynamics of the sensor measurements. The output disturbance, $G_d(s)$, may be represented by the unforced, natural fluctuating state of the flow. An autoregressive model is suitable for the determination of this system. The success of the feedback control scheme will be determined if adequate disturbance rejection as well as reference tracking ability are shown.

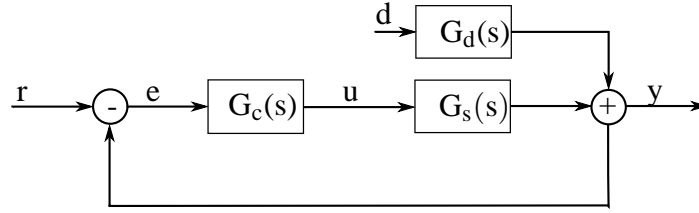


Figure 93: Closed-loop block diagram of output disturbance model for controller verification.

The closed-loop system is formulated such that

$$Y = \begin{bmatrix} \frac{G_s G_c}{1 + G_s G_d} & \frac{G_d}{1 + G_s G_d} \end{bmatrix} \begin{bmatrix} r \\ d \end{bmatrix}, \quad (102)$$

where r and d are the reference and disturbance inputs, respectively. The transfer function between different input-output pairs can be analyzed for varying forms of $G_c(s)$. For the purpose of this paper, the design of the controller, $G_c(s)$, is standard PID control. A PID control algorithm is implemented because of the simplicity and ease of design. The asymmetric vortex dynamics lend themselves very well to linear time invariant systems, so a simple control algorithm is appropriate for control of the vortex flow behind the ogive. The control algorithm is given by

$$G_c(s) = K_p + K_d s + \frac{K_i}{s}, \quad (103)$$

where K_p , K_d , K_i are the proportional, derivative and integral terms, respectively. A standard tuning method is adopted where the gains are varied in a systematic fashion to achieve proper closed-loop response to a step reference input.

5.4.8.1 Closed Experimental Model Results The response of $G_s G_c / (1 + G_s G_d)$ is shown for varying proportional and integrator gains in Figure 94. Selected gains for the PI controller are, $K_i = 80$ and $K_p = 1.2$. The derivative term caused an instability in the transfer function, $G_s G_c / (1 + G_s G_d)$, purely due to the time delay in the system.

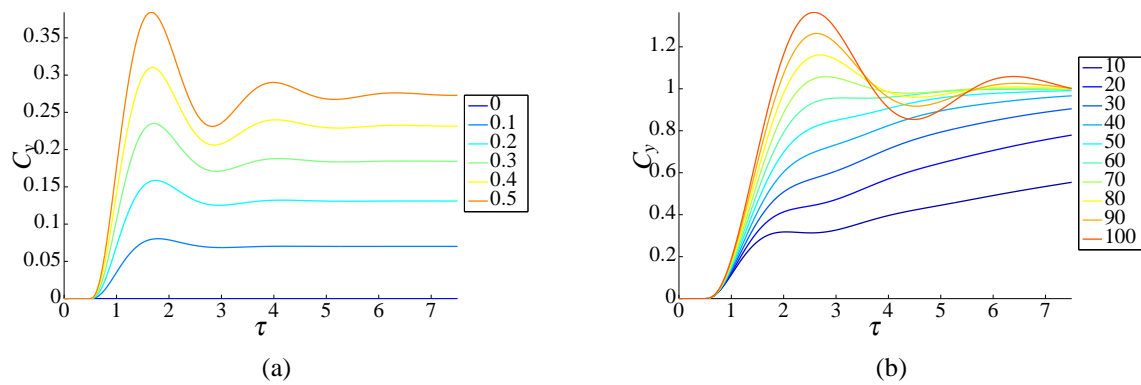


Figure 94: (a) Closed-loop step response with varying proportional gain. (b) Closed-loop step response with varying integral gain.

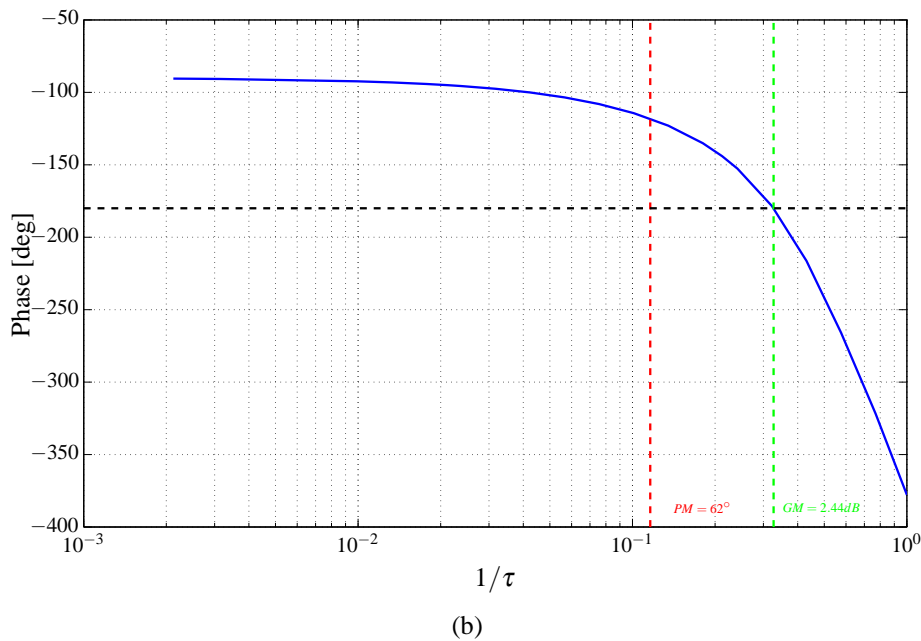
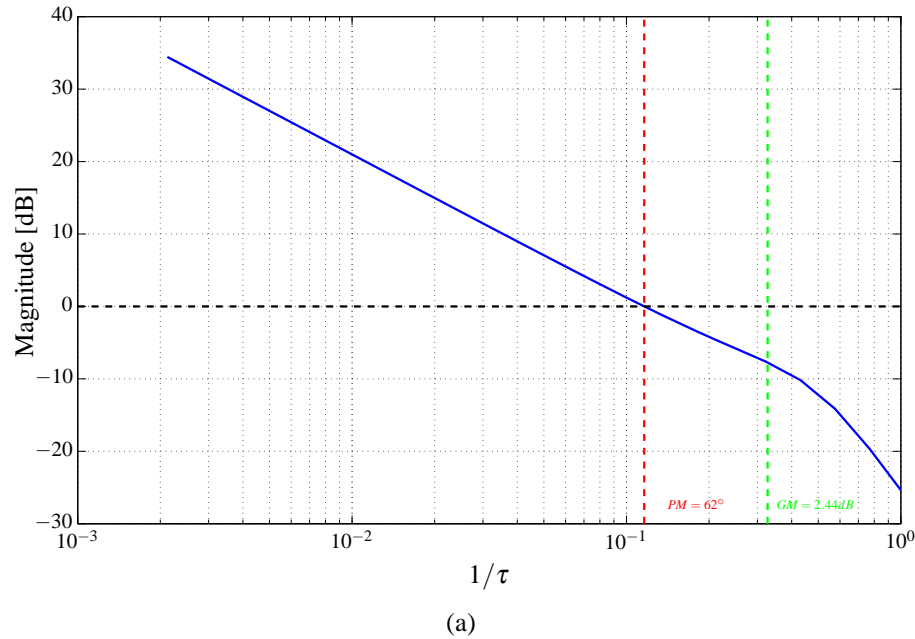
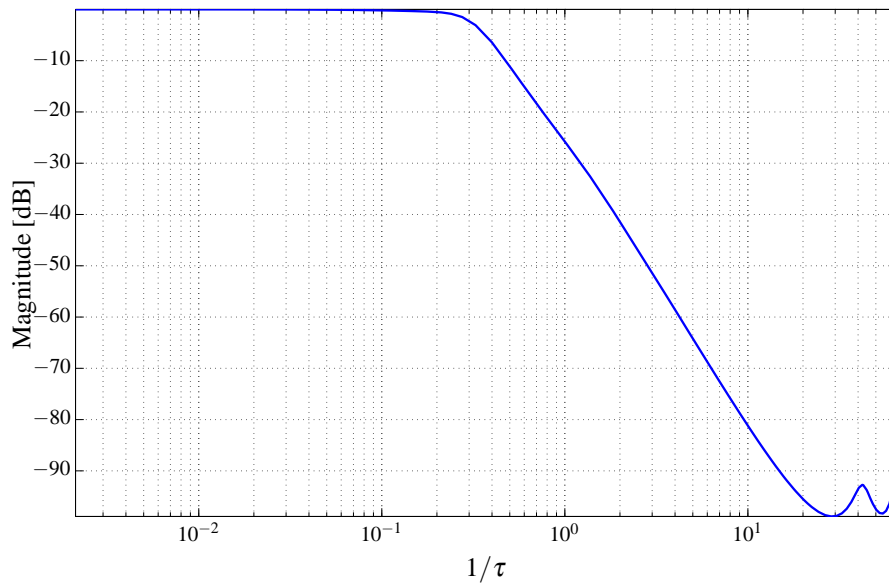


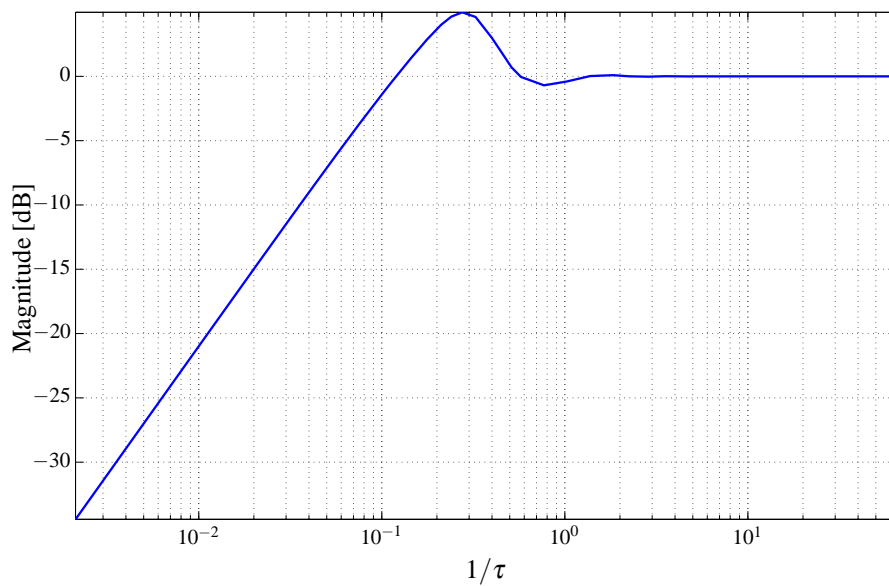
Figure 95: Magnitude (a) and phase (b) response of open loop system, $G_{ol} = G_s G_c$. The gain and phase margins are computed as $2.44dB$ and 62° , respectively.

The frequency response for the reference tracking and disturbance rejection capabilities are shown in Figure 96. As shown in Figure 96a, the closed-loop system response adequately follows reference signals up to approximately $1/(2\tau)$ which was determined to be the cutoff frequency in the open-loop analysis of the dynamics. Figure 96b shows the closed-loop system attenuation of disturbances (i.e. the ability of the closed-loop system to reduce fluctuations as a function of frequency). Disturbances are attenuated up to a frequency of $1/(4\tau)$ which turns out to be half of

the cut off frequency.



(a) Reference tracking



(b) Disturbance rejection

Figure 96: (a) Closed-loop system response for input reference to output response. (b) Closed-loop system response for input disturbance to output response.

A typical time simulation is shown in Figure 98 to a time varying reference with a uniform random disturbance input. As shown the response of the side force adequately follows a reference signal. The controller is designed aggressively enough to have over/under shoot characteristics with step changes. Additionally, the disturbances at lower frequencies are reduced in size.

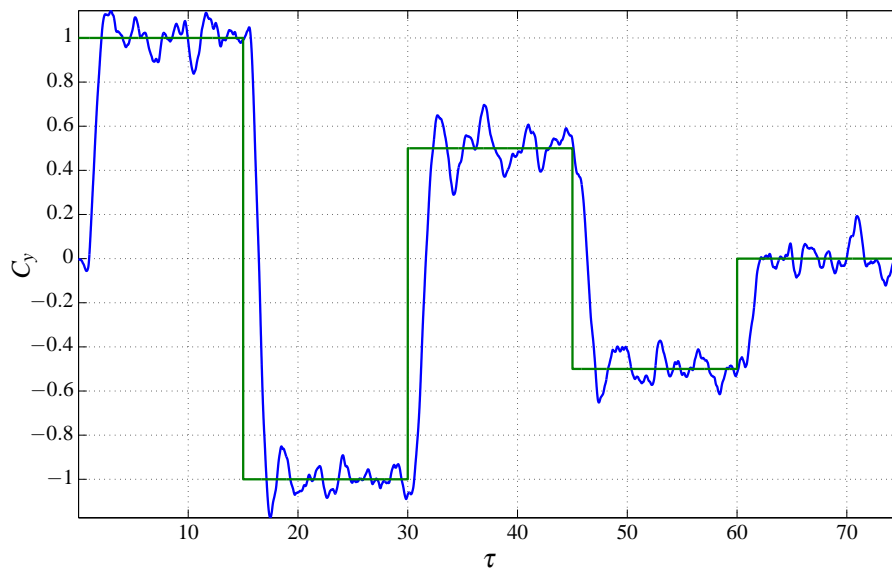


Figure 97: Time simulation of closed-loop system for varying reference and disturbance excitation.

5.4.9 Closed Experimental Results

Once the closed-loop model was fully developed and analyzed (as discussed in Section ??) a reference tracking exercise was conducted with the experimental model in the wind tunnel to assess the performance of the closed-loop controller. For these investigations an arbitrary piecewise reference waveform was generated for the controller to track, where the target side force coefficient was changed seven times across the 15 sec. testing period to both positive and negative side force coefficients. A PID (Proportional-Integral-Derivative) controller was developed utilizing both the port and starboard actuators to impart control and all four time-resolved pressure transducers were used to estimate the instantaneous side force coefficient on the body for feedback. Figure 98 displays the performance of the experiment for the reference tracking exercise, where the experimental signal is a phase averaged result of five independent experimental tests following the same arbitrary reference signal (also presented). For the experiments the proportional and integral gains were 0.25 and 0.000977, respectively. The derivative gain was set to zero because it was found during the modeling that any amount of derivative gain forced the model to go unstable. Clearly, the experiment was successfully able to track the reference signal in the mean of the linearly estimated side force coefficient, however significant higher frequency fluctuations were still observed, which the controller was unable to modify.

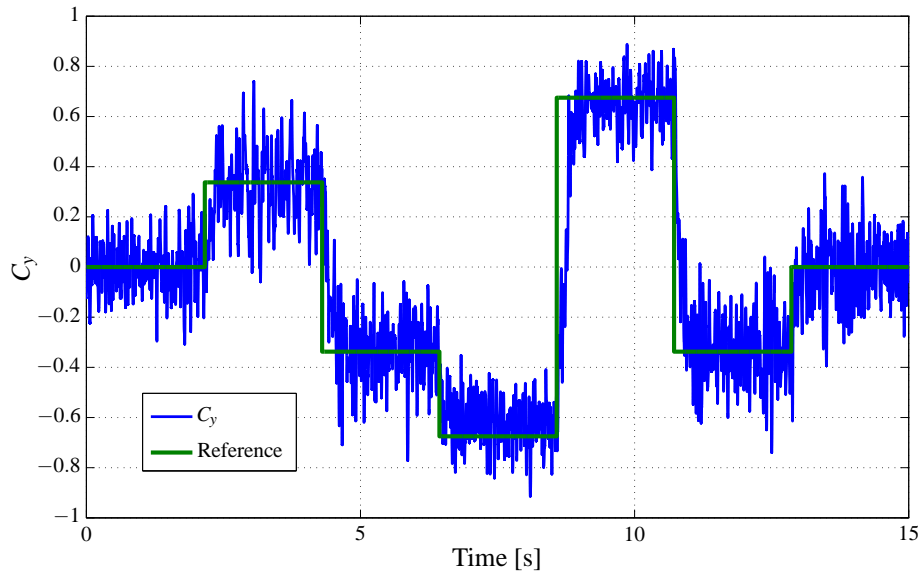


Figure 98: Closed loop experimentation results with same controller from above section.

5.4.9.1 Closed Simulation Model Results The response of $G_s G_c / (1 + G_s G_d)$ is shown for varying proportional and integrator gains in Figure 94. Selected gains for the PI controller are, $K_i = .012$ and $K_p = 7 \times 10^{-7}$. The derivative term caused an instability in the transfer function, $G_s G_c / (1 + G_s G_d)$, purely due to the time delay in the system.

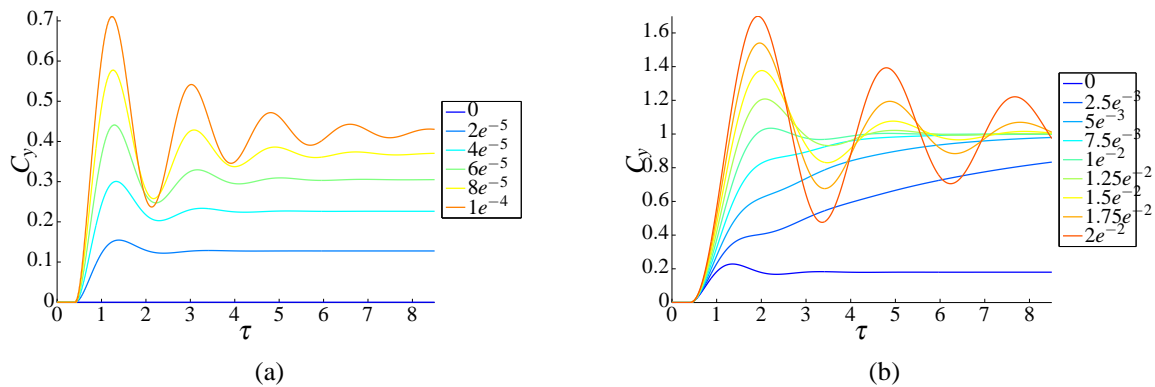


Figure 99: (a) Closed-loop step response with varying proportional gain. (b) Closed-loop step response with varying integral gain.

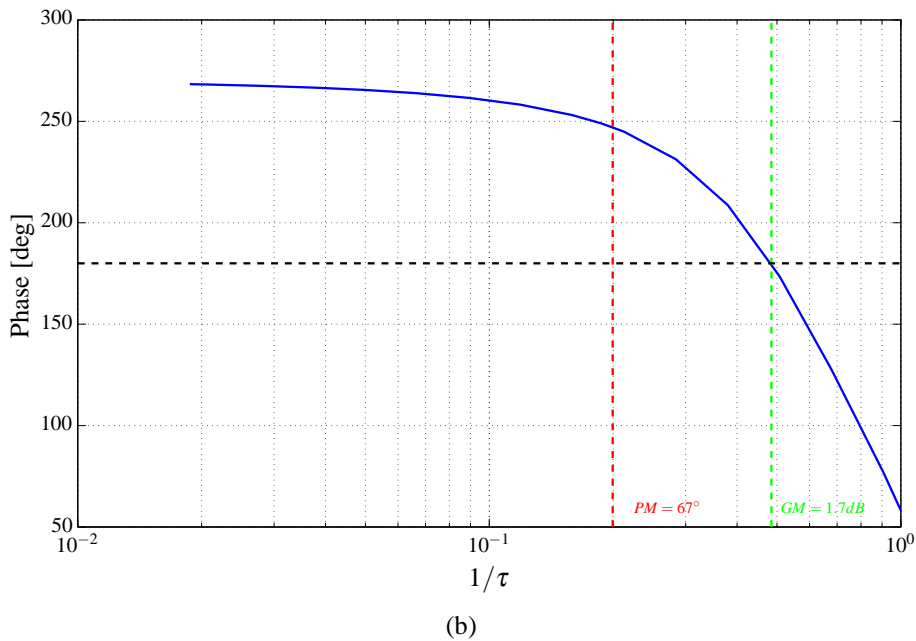
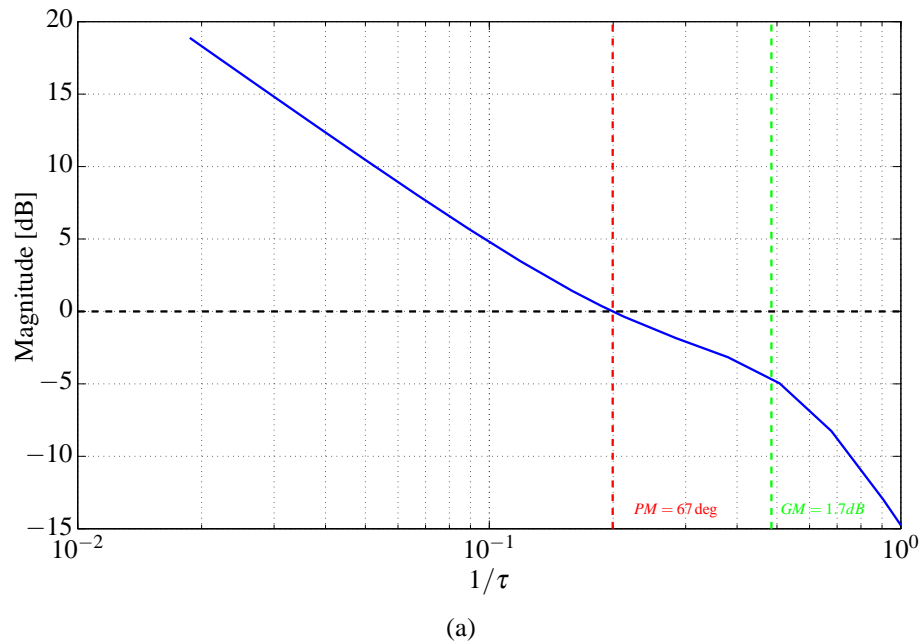
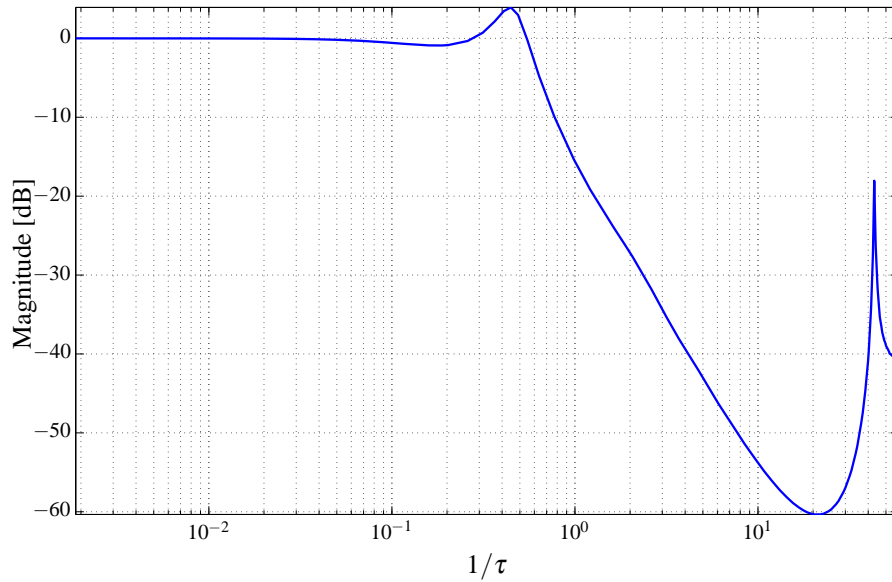


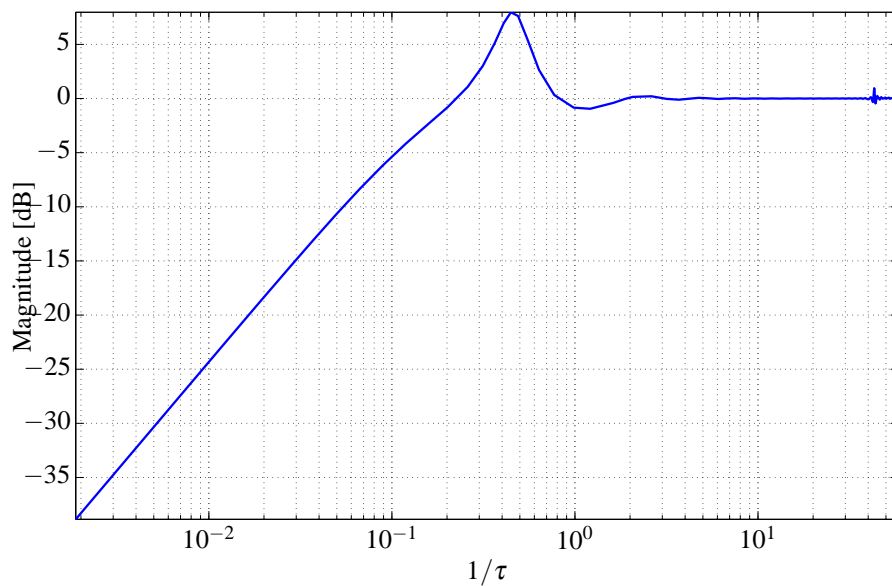
Figure 100: Magnitude (a) and phase (b) response of open loop system, $G_{ol} = G_s G_c$. The gain and phase margins are computed as 1.7dB and 67° , respectively.

The frequency response for the reference tracking and disturbance rejection capabilities are shown in Figure 101. As shown in Figure 101a, the closed-loop system response adequately follows reference signals up to approximately $1/(2\tau)$ which was determined to be the cutoff frequency in the open-loop analysis of the dynamics. Figure 101b shows the closed-loop system attenuation of disturbances (i.e. the ability of the closed-loop system to reduce fluctuations as a function of frequency). Disturbances are attenuated up to a frequency of $1/(4\tau)$ which turns out to

be half of the cut off frequency.



(a) Reference tracking



(b) Disturbance rejection

Figure 101: (a) Closed-loop system response for input reference to output response. (b) Closed-loop system response for input disturbance to output response.

A typical time simulation is shown in Figure 98 to a time varying reference with a uniform random disturbance input. As shown the response of the side force adequately follows a reference signal. The controller is designed aggressively enough to have over/under shoot characteristics with step changes. Additionally, the disturbances at lower frequencies are reduced in size.

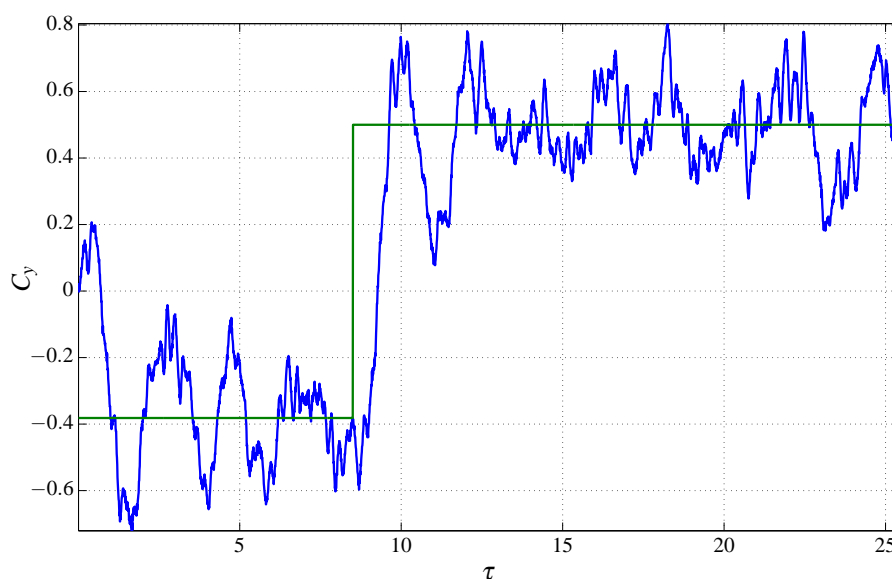


Figure 102: Time simulation of closed-loop system for varying reference and disturbance excitation.

5.4.9.2 Closed Simulation Results Using the unforced data, a linear prediction-error minimization method was used to model the dynamics of the flowfield for different momentum coefficients. Based on the model, a PID controller was developed to reference track a prescribed side force trajectory. The details of the model development as well as the PID controller can be found in Fagley et al. [submitted 2012] (experimental) as well as Porter et al. [2013] (computational). Figure 103 shows the initial results obtained using the PID controller in conjunction with Cobalt. A reference side force of $C_y = 0.5$ was used to test if the controller could reference track. For this simulation, an aggressive gain for the proportional and integral components was used. As a result, the side force overshoots its reference condition. At this point, the controller turns on the starboard actuator to counteract this overshoot, creating a large oscillation in the side force. However, note that this is exactly what was predicted in the model simulation of the controller (Fig. ??). While there is a small discrepancy in the transition time between the controller model and the CFD simulation, the general overall trends are captured in the model. As shown in the model, this oscillation from aggressive PID gains eventually damps out and the controller is able to stabilize the side force at the desired reference. It is postulated that if the current CFD simulation were carried out farther, the same results would be seen, especially since the overshoot of the second peak in the CFD is smaller than the initial overshoot, indicating that it is starting to be damped out.

5.4.10 Modeling summary

The asymmetric vortex regime of a von Kármán ogive with a fineness ratio of 3.5 is experimentally studied at a Reynolds number of 156,000. Both port and starboard plasma actuators are used to introduce fluidic disturbances at the tip of the ogive. These disturbances are amplified through the flow's convective instability to produce a deterministic port or starboard asymmetric vortex state

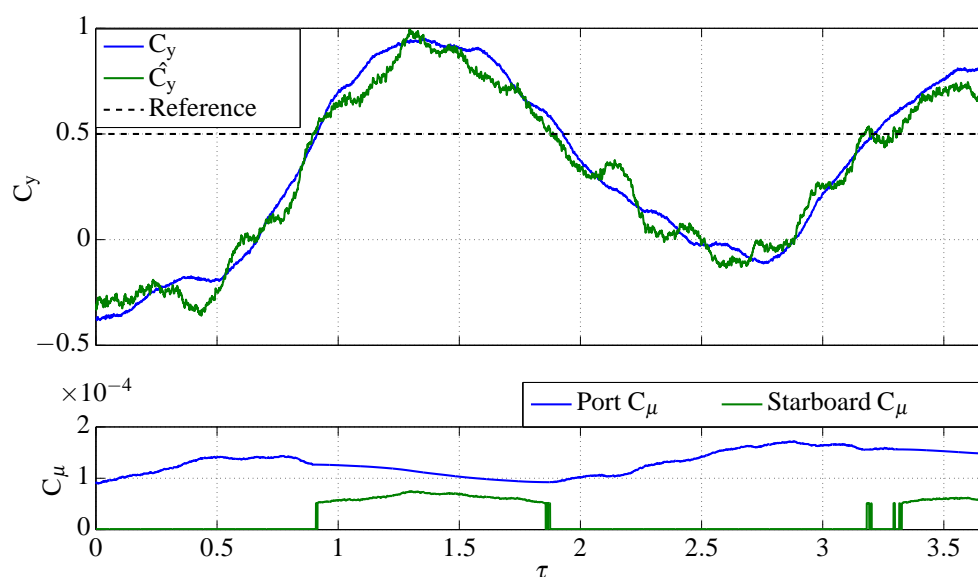


Figure 103: Closed-loop simulation with a reference $C_y = 0.5$ and the corresponding C_μ out of the port and starboard actuators.

(i.e. side force). Accurate control or manipulation of this asymmetric vortex phenomenon holds the potential for increased maneuverability and stability characteristics of slender flight vehicles.

Unforced and open-loop experimental tests were carried out to understand and quantify the vortex dynamics. Step, impulse and sinusoidal modulation inputs provided the necessary dynamics and diverse training and validation data sets for the formulation of a linear time invariant dynamical model. Standard linear system identification approaches were implemented to represent the training data set. In particular, output error, prediction error and subspace identification methods were used to capture the asymmetric vortex dynamics. These methods were validated by time and frequency domain methods. The measurements and modeling methods showed the cutoff frequency of the flow to be around 50 Hz which is directly related to two flow through times, i.e. the time it takes a particle to flow from the tip of the model to the base of the ogive section.

A closed-loop system was designed such that the unforced fluid dynamics and measurement noise were modeled as an output disturbance. The prediction error model was well suited for this system. A PID controller was implemented in the closed loop system and designed for adequate disturbance rejection and reference tracking performance. The closed loop transfer functions were analyzed. A time simulation was shown in which the controller was able to guide the asymmetric vortex state to an arbitrary asymmetric pressure distribution while adequately regulating the disturbances. To improve this control design approach a predictor model would be essential to reduce the convective time delay from the actuator to the sensor. Alternatively, the sensors would have to be placed closer to the nose of the ogive which would reduce the amplitude of the pressure measurements, reducing the signal to noise ratio.

5.5 Business Summary

The business plan was divided into both a salary portion and travel portion for the senior engineer. The projected salary portion is listed in table 9, itemized yearly for the duration of the contractual agreement. The projected salary portion is listed in 10 for travel to one conference per year.

Table 9: Total projected salary for contract duration

Period of Performance	Labor Category	Rate	Hours	Yearly Price
8 Jan 2010 to 7 Jan 2011	Senior Engineer	\$35.51	1880	\$66,750
8 Jan 2011 to 7 Jan 2012	Senior Engineer	\$39.89	1880	\$75,000
8 Jan 2012 to 7 Jan 2013	Senior Engineer	\$42.55	1880	\$80,000
Total				\$221,750

Table 10: Total projected travel for contract duration

Travel Expenses	Flights	Lodging/night	Per Diem (M&IE)	Registration	Total
2010 Conference	\$800.00	\$120.00	\$80.00	\$300.00	\$2,100.00
2011 Conference	\$800.00	\$120.00	\$80.00	\$300.00	\$2,100.00
2012 Conference	\$800.00	\$120.00	\$80.00	\$300.00	\$2,100.00
Total					\$6,300.00

The actual costs incurred are listed in Tables 11 and 12 for salary and travel, respectively. As shown, costs between projected and actual did differ slightly. This was mainly due to obligatory issues during Y3.Q1 and Y3.Q2. Also, more travel was required over the course of the contractual duration.

6 References

- F. Abergel and R. Temam. On some control problems in fluid mechanics. *Theoret. Comput. Fluid Dyn.*, 1:303–325, 1990.
- L. Angrisani, P. Daponte, and M. D’Apuzzo. A Method Based on Wavelet Networks for the Detection and Classification of Transients. *Proceedings of the IEEE Instrumentation and Measurement Technology Conference*, vol. 2,:903–908, 1998.
- M. Balajewicz, F. Nitzsche, and D. Feszty. Reduced Order Modeling of Nonlinear Transonic Aerodynamics Using a Pruned Volterra Series. In *AIAA 2009-2319*, 2009.
- M. J. Balas. Feedback Control of Flexible Systems. *IEEE Transactions on Automatic Control*, AC-23(3):673–679, 1978.
- R. Becker, R. King, R. Petz, and W. Nitsche. Adaptive Closed-Loop Separation Control on a High-Lift Configuration using Extremum Seeking. In *AIAA 2006-3493*, 2006.

Table 11: Total salary paid from January 2010 to January 2013

Period of Performance	Rate	Hours	Price
Y1.Q1	\$ 35.51	470	\$ 16,689.70
Y1.Q2	\$ 35.51	470	\$ 16,689.70
Y1.Q3	\$ 35.51	470	\$ 16,689.70
Y1.Q4	\$ 35.51	470	\$ 16,689.70
Y2.Q1	\$ 39.90	470	\$ 18,753.00
Y2.Q2	\$ 39.90	470	\$ 18,753.00
Y2.Q3	\$ 39.90	470	\$ 18,753.00
Y2.Q4	\$ 39.90	470	\$ 18,753.00
Y3.Q1	\$ 43.67	450	\$ 19,651.50
Y3.Q2	\$ 43.67	420	\$ 18,341.40
Y3.Q3	\$ 43.67	470	\$ 20,524.90
Y3.Q4	\$ 43.67	470	\$ 20,524.90
Total Salary Paid			\$ 220,813.50

Table 12: Total salary paid from January 2010 to January 2013

Dates	Type	Location	Total
May 26-28, 2010	AFC II	Germany	\$ 1,575.00
August 1-5, 2010	AIAA GNC	Toronto	\$ 2,053.76
Dec 7-10, 2011	ADD CoOp	South Korea	\$ 2,100.00
Dec 2-7, 2012	ADD CoOp	South Korea	\$ 2,100.00
Total Travel Funds			\$ 8,028.76

- G. Berkooz, P. Holmes, and J. L. Lumley. The Proper Orthogonal Decomposition in the Analysis of Turbulent Flows. *Ann. Rev. Fluid Mech.*, 25:539–575, 1993.
- D. H. Bridges. The asymmetric vortex wake problem - asking the right question. In *AIAA Paper 2006-3553*, 2006.
- J. Chen and D. Bruns. WaveARX Neural Network Development for System Identification Using a Systematic Design Synthesis. *Industrial and Engineering Chemistry Research*, vol. 34:4420–4435, 1995.
- K. Cohen, J. Z. Ben-Asher, and T. Weller. Vibration Control Using Fuzzy-Logic-Based Active Damping. *J. Aircraft*, 40(2):384–389, 2003a.
- K. Cohen, S. Siegel, and T. McLaughlin. Sensor Placement Based on Proper Orthogonal Decomposition Modeling of a Cylinder Wake. In *AIAA Paper 2003-4259*, 2003b.
- K. Cohen, S. Siegel, J. Seidel, S. Aradag, and T. McLaughlin. Sensor based estimation of POD Flow States using Artificial Neural Networks. *to be submitted to Computers and Fluids*, 2007.
- G. Constantinescu, R. Pacheco, and K. Squires. Detached-eddy simulation of flow over a sphere. In *AIAA Paper 2002-0425*, 2002.
- C. Fagley, M. Balas, S. Siegel, J. Seidel, and T. McLaughlin. Reduced Order Model of Cylinder Wake with Direct Adaptive Feedback Control. In *AIAA Paper 2009-5856*, 2009.
- C. Fagley, J. Seidel, S. Siegel, and T. McLaughlin. Reduced Order Modeling using Proper Orthogonal Decomposition (POD) and Wavenet System Identification of a Free Shear Layer. In *2nd Active Flow Control Conference, Berlin, Germany*, 2010.
- C. Fagley, J. Farnsworth, J. Seidel, and T. McLaughlin. Experimental Study of Open Loop Plasma Actuation on a von Karman Ogive. In *AIAA Paper 2012-0905*, 2012a.
- C. Fagley, C. Porter, J. Seidel, J. Farnsworth, and T. McLaughlin. Optimal sensor arrangement for asymmetric vortex state estimation on a slender body at high incidence. In *AIAA Aerospace Sciences Meeting, American Institute of Aeronautics and Astronautics, New Orleans, LA (submitted for publication)*, 2012b.
- C. Fagley, J. Farnsworth, C. Porter, J. Seidel, T. McLaughlin, J. Lee, and E. Lee. Open-loop dynamics of asymmetric vortex wake behind an ogive at high incidence. *Journal of Flow Control*, submitted 2012.
- J. Farnsworth, C. Fagley, C. Porter, J. Seidel, and T. McLaughlin. The transient response of a von karman ogive to open loop plasma actuation. In *AIAA Paper 2012-2955*, 2012.
- J. R. Forsythe and S. H. Woodson. Unsteady CFD Calculations of Abrupt Wing Stall Using Detached-Eddy Simulation. In *AIAA Paper 2003-0594*, 2003.
- J. R. Forsythe, K. A. Hoffmann, R. M. Cummings, and K. D. Squires. Detached-Eddy Simulation with Compressibility Corrections Applied to a Supersonic Axisymmetric Base. *J. Fluids Eng.*, 124(4):911–923, 2002.

- J. R. Forsythe, K. D. Squires, K. E. Wurtzler, and P. R. Spalart. Detached-Eddy Simulation of the F-15E at High Alpha. *J. Aircraft*, 41(2):193–200, 2004.
- R. Fuentes and M. Balas. Direct Adaptive Rejection of Persistent Disturbances. *J. Math. Anal. Appl.*, 251:11:28–39, 2000.
- J. Gerhard, M. Pastoor, R. King, B. Noack, A. Dillmann, M. Morzynski, and G. Tadmor. Model Based Control of Vortex Shedding using Low-Dimensional Galerkin Models. 2003.
- E. A. Gillies. Low-Dimensional Control of the Circular Cylinder Wake. *J. Fluid Mech.*, 371: 157–178, 1998.
- S. Gordeyev, E. Jumper, T. T. Ng, and A. B. Cain. The Optical Environment of a Cylindrical Turret with a Flat Window and the Impact of Passive Control Devices. In *AIAA Paper 2005-4657*, 2005.
- D. Griffith and A. G.R. A Partially Decoupled RLS Algorithm for Volterra Filters. *IEEE Transactions on Signal Processing*, 47, 1999.
- M. J. Grismer, W. Z. Strang, R. F. Tomaro, and F. C. Witzemman. Cobalt: A Parallel, Implicit, Unstructured Euler/Navier-Stokes Solver. *Advances in Engineering Software*, 29(3-6):365–373, 1998.
- R. Hansen and J. Forsythe. Large and Detached Eddy Simulations of a Circular Cylinder Using Unstructured Grids. In *AIAA Paper 2003-775*, 2003.
- M. A. Z. Hasan. The flow over a backward-facing step under controlled perturbation: laminar separation. *J. Fluid Mech.*, 238:73–96, 1992.
- C.-M. Ho and P. Huerre. Perturbed free shear layers. *Ann. Rev. Fluid Mech.*, 16:365–424, 1984.
- P. Holmes, J. L. Lumley, and G. Berkooz. *Turbulence, Coherent Structures, Dynamical Systems and Symmetry*. Cambridge Univ. Press, New York, 1996.
- J. Jeong and F. Hussain. On the identification of a vortex. *J. Fluid Mech.*, 285:69–94, 1995.
- E. J. Jumper and E. J. Fitzgerald. Recent advances in aero-optics. *Prog. Aero. Sci.*, 37:299–339, 2001.
- G. Karypis, K. Schloegel, and V. Kumar. *ParMETIS: Parallel Graph Partitioning and Sparse Matrix Ordering Library Version 1.0*, 1997.
- R. King, R. Becker, M. Garwon, and L. Henning. Robust and adaptive closed-loop control of separated shear flows. In *AIAA Paper 2004-2519*, 2004.
- W. R. Lanser and L. A. Meyn. Forebody Flow Control on a Full-Scale f/a-18 aircraft. *J. Aircraft*, 31(6):1365–1371, 1994.
- H. Larochelle, Y. Bengio, J. Louradour, and P. Lamblin. Exploring Strategies for Training Deep Neural Networks. *Journal of Machine Learning Research*, 1:1–40, 2009.

- E. Lee, J. Lee, K. Lee, J. Seidel, C. Fagley, C. Porter, and T. McLaughlin. Effects of the plasma actuation on the asymmetric vortex around an ogive body at high incidence. In *AIAA Aerospace Sciences Meeting, American Institute of Aeronautics and Astronautics, New Orleans, LA (submitted for publication)*, 2012.
- D. Lucia, P. Beran, and S. W.A. Aeroelastic System Development Using Proper Orthogonal Decomposition and Volterra Theory. In *AIAA 2003-1922*, 2003.
- A. Mani, M. Wang, and P. Moin. Resolution requirements for aero-optical simulations. *J. Comp. Phys.*, 227(21):9008–9020, 2008.
- D. Marcum and N. Weatherill. Unstructured Grid Generation using Iterative Point Insertion and Local Reconnection. *AIAA J.*, 33(9):1619–1625, 1995.
- T. Matsuno, H. Kawazoe, and R. C. Nelson. Aerodynamic Control of High Performance Aircraft Using Pulsed Plasma Actuators. In *AIAA Paper 2009-0697*, 2009.
- L. McMackin, R. J. Hugo, R. E. Pierson, and C. R. Truman. High speed optical tomography system for imaging dynamic transparent media. *Optics Express*, 1(11):302–311, 1997.
- C. Meneveau and J. Katz. Scale-Invariance and Turbulence Models for Large-Eddy Simulation. *Ann. Rev. Fluid Mech.*, 32:1–32, 2000.
- M. M. M.M. Polycarpou and S. Weaver. Adaptive Wavelet Control of Nonlinear Systems. *Proceedings of the 36th Conference on Decision & Control*, vol. 4:3890–3895, 1997.
- J. P. Moeck, M. R. Bothien, C. O. Paschereit, G. Gelbert, and R. King. Two-Parameter Extremum Seeking for Control of Thermoacoustic Instabilities and Characterization of Linear Growth. In *AIAA 2007-1416*, 2007.
- S. A. Morton, M. B. Steenman, R. M. Cummings, and J. R. Forsythe. DES grid resolution issues for vortical flows on a delta wing and an F-18C. In *AIAA Paper 2003-1103*, 2003.
- S. A. Morton, R. M. Cummings, and D. B. Kholodar. High Resolution Turbulence Treatment of F/A-18 Tail Buffet. In *AIAA Paper 2004-1676*, 2004.
- B. R. Noack, K. Afanasiev, M. Morzynski, G. Tadmor, and F. Thiele. A hierarchy of low-dimensional models for the transient and post-transient cylinder wake. *J. Fluid Mech.*, 497:335–363, 2003.
- B. R. Noack, G. Tadmor, and M. Morzynski. Low-dimensional models for feedback flow control. Part I: Empirical Galerkin models. In *AIAA Paper 2004-2408*, 2004.
- M. Norgaard, Ravn, O, Poulsen, N. K, Hansen, and L. K. *Neural Networks for Modelling and Control of Dynamic Systems*. Springer Advanced Textbooks in Control and Signal Processing, 2003.
- M. Oljaca and A. Glezer. Measurements of Aero-Optical Effects in a Plane Shear Layer. In *AIAA Paper 1997-2352*, 1997.

- D. Oster and I. Wygnanski. The forced mixing layer between parallel streams. *J. Fluid Mech.*, 123:91–130, 1982.
- Y. Oussar and G. Dreyfus. Initialization by Selection for Wavelet Network Training. *Neurocomputing*, vol. 34:131–143, 2000.
- S. B. Pope. *Turbulent Flows*. University Press, Cambridge, 2000.
- C. Porter, C. Fagley, J. Farnsworth, J. Seidel, and T. McLaughlin. Closed-Loop Flow Control of a Tangent Ogive at a High Angle of Attack. In *AIAA Paper 2013-0395*, 2013.
- D. Rempfer. On Low-Dimensional Galerkin Models for Fluid Flow. *Theoret. Comput. Fluid Dyn.*, 14:75–88, 2000.
- K. Roussopoulos. Feedback control of vortex shedding at low Reynolds numbers. *J. Fluid Mech.*, 248:267–296, 1993.
- C. W. Rowley, T. Colonius, and R. M. Murray. Model reduction for compressible flows using POD and Galerkin projection. *Physica D*, 189:115–129, 2004.
- J. Seidel, S. G. Siegel, K. Cohen, and T. McLaughlin. POD Based Separation Control on the NACA0015 Airfoil. In *AIAA Paper 2005-0297*, 2005.
- J. Seidel, S. Siegel, and T. McLaughlin. Computational Investigation of Aero-Optical Distortions in a Free Shear Layer. In *AIAA Paper 2009-0362*, 2009.
- S. Siegel, K. Cohen, and T. McLaughlin. Low-Dimensional Feedback Control of the von Karman Vortex Street at a Reynolds Number of 100. In *IUTAM Symposium on Integrated Modeling of Fully Coupled Fluid Structure Interactions using Analysis, Computations and Experiments*, 2003a.
- S. Siegel, K. Cohen, and T. McLaughlin. Feedback Control of a Circular Cylinder Wake In Experiment and Simulation (invited). In *AIAA Paper 2003-3569*, 2003b.
- S. Siegel, K. Cohen, J. Seidel, and T. McLaughlin. Two Dimensional Simulations of a Feedback Controlled D-Cylinder Wake. In *AIAA Paper 2005-5019*, 2005a.
- S. Siegel, J. Seidel, C. Fagley, D. Luchtenburg, K. Cohen, and T. McLaughlin. Low-dimensional modelling of a transient cylinder wake using double proper orthogonal decomposition. *J. Fluid Mech.*, 610:1–42, 2008.
- S. G. Siegel, K. Cohen, J. Seidel, and T. McLaughlin. Short Time Proper Orthogonal Decomposition for State Estimation of Transient Flow Fields. In *AIAA Paper 2005-0296*, 2005b.
- S. Sirisup, G. E. Karniadakis, D. Xiu, and I. G. Kevrekidis. Equation-free/Galerkin-free POD-assisted computation of incompressible flows. *J. Comp. Phys.*, 207:568–587, 2005.
- L. Sirovich. Turbulence and the Dynamics of Coherent Structures Part I: Coherent Structures. *Q Appl Math*, 45(3):561 – 571, 1987.

- P. R. Spalart. Strategies for Turbulence Modeling and Simulation. *Int. J. Heat Fluid Flow*, 21: 252–263, 2000.
- K. Squires, J. Forsythe, and P. Spalart. Detached-Eddy Simulation of the separated flow around a forebody crosssection. In B. Geurts, R. Friedrich, and O. Metais, editors, *Direct and Large-Eddy Simulation IV, ERCOFTAC Series Volume 8*, pages 481–500. Kluwer Academic Press, 2001.
- W. Strang, R. Tomaro, and M. Grismer. The Defining Methods of Cobalt60: A Parallel, Implicit, Unstructured Euler/Navier-Stokes Flow Solver. In *AIAA Paper 1999-0786*, 1999.
- A. Travin, M. Shur, M. Strelets, and P. Spalart. Detached-Eddy Simulations Past a Circular Cylinder. *Flow, Turbulence and Combustion*, 63:293–313, 1999.
- J. Trolinger, D. L’Experance, J.-H. Kim, J. Kastner, W. Lempert, and M. Samimy. Optical Diagnostics for Quantifying Flow Control Effects on Aero Optical Wavefront Degradation. In *AIAA Paper 2005-4658*, 2005.
- M. Van Dyke. *An Album of Fluid Motion*. Parabolic Press, 1982.
- B. Vukasinovic, D. G. Lucas, and A. Glezer. Direct Manipulation of Small-Scale Motions in a Plane Shear Layer. In *AIAA Paper 2004-2617*, 2004.
- J. Zhang, G. Walter, Y. Miao, and W. Lee. Wavelet Neural Networks for Function Learning. *IEEE Transactions on Signal Processing*, vol. 43, no. 6:1485–1497, 1995.
- Q. Zhang and A. Benveniste. Wavelet Networks. *IEEE Transactions on Neural Networks*, 3: 889–898, 1992.